ACOUSTO-OPTIC PROPERTIES OF TELLURIUM AND SELENIUM AND THEIR APPLICATIONS

BY
SUSUMU FUKUDA

JANUARY 1980

DEPARTMENT OF ELECTRONICS
KYOTO UNIVERSITY
KYOTO, JAPAN

ACOUSTO-OPTIC PROPERTIES OF TELLURIUM AND SELENIUM AND THEIR APPLICATIONS

BY
SUSUMU FUKUDA

JANUARY 1980

DEPARTMENT OF ELECTRONICS
KYOTO UNIVERSITY
KYOTO, JAPAN

ABSTRACT

Acousto-optic properties of single-crystal Te and amorphous Se at the 10.6-μm wavelength of a CO_2 laser are studied and discussed from an applicational point of view in this thesis. The thesis contains the following studies.

(1) Acousto-optic figures of merit in Te are determined by the Dixon-Cohen method making use of longitudinal acoustic waves propagating along the crystallographic x and z axes in Te. It is found that Te possesses exceptionally large figures of merit in the materials ever measured at 10.6 μm. The largest value obtained is 5850×10^{-18} sec^3/g for longitudinal waves propagating along the x axis and incident light polarized parallel to the z axis. Five of the eight non-vanishing independent Pockels photoelastic tensor components are deduced from the determined figures of merit.

(2) Optical activity in Te is precisely measured over the infrared wavelength range between 4.0 and 10.6 μm and influences of the optical activity on the acousto-optic properties of Te are discussed.

(3) Based on the knowledges obtained from the above results, potential applicabilities of Te crystal to an infrared acousto-optic deflector and modulator for the use especially at 10.6 μm are evaluated in terms of figures of merit, optical properties, acoustic properties (in particular, acoustic loss), resolution, and access time. As a result, it is found that Te is one

of the most promising acousto-optic materials for 10.6-μm wavelength.

(4) A prototype of Te acousto-optic deflector is fabricated based on the results obtained above and its operational characteristics are examined at 10.6 μm.

(5) Contributions from the indirect photoelastic effect and from the acousto-electrically induced free-carrier density waves to the photoelasticity in piezoelectric semiconductors are considered by taking the existence of both electrons and holes into account. This kind of free-carrier density waves are observed accompanying piezoelectrically active acoustic waves which propagate in piezoelectric semiconductors like Te. Explicit expressions for the effective photoelastic constants corresponding to these contributions are derived on the basis of small-signal acousto-electric theory by taking account of all of the material anisotropy. The results obtained are applicable either to extrinsic or to intrinsic semiconductors.

(4) Numerical evaluation of these contributions to the photoelasticity is carried out by taking Te as an example. In accordance with the theoretical prediction, an appreciable diffraction ascribable to the free-carrier density waves is observed in the acousto-optic diffraction experiments utilizing a Te crystal in an intrinsic conduction regime at room temperature. The observed diffraction intensity is in satisfactory agreement with the theoretically predicted value within a factor of 3.

(5) As an application of superior acousto-optic properties of Te to nonlinear optical effects, a novel phase-matching technique utilizing acousto-optic interactions is proposed.

Employing this phase-matching technique, relatively efficient optical second harmonic generation of a 10.6-μm light is experimentally demonstrated. It is revealed that by making use of this new phase-matching technique, restriction for the crystal orientation can be much relaxed as compared with the conventional collinear index-matching method.

(6) Acousto-optic figures of merit in amorphous Se are determined by the Dixon-Cohen method making use of longitudinal acoustic waves propagating in this material. It is found that amorphous Se possesses large figures of merit almost comparable to those of Te. Two non-vanishing independent Pockels photoelastic tensor components in amorphous Se are also determined. The wavelength dependence of these photoelastic constants suggests that the photoelasticity in amorphous Se can be attributed to the strain-induced change in the interband transition between the lone-pair p-band and the antibonding p-band. It is found that the addition of several percents of arsenic significantly improves the acousto-optic properties of amorphous Se.

(7) Feasibility of amorphous Se as an optical waveguide material at 10.6 μm is experimentally evaluated. Based on this result, a photoelastic optical modulator with a guide structure is constructed, and its modulation characteristics are measured.

ACKNOWLEDGMENTS

The author wishes to express his sincere gratitude and appreciation to Professor Akira Kawabata for his continuing guidance and encouragement throughout this work. The author deeply acknowledges the invaluable guidance and advice of Professor Tadashi Shiosaki. The author is grateful to Professors Akio Sasaki and Hiroyuki Matsunami for their encouragements and suggestions.

Appreciations are due to Mr. Masatoshi Adachi for his continuous stimulation, and to Dr. Shigeo Fujita, Dr. Junji Saraie, Dr. Akira Suzuki, and Mr. Shigehiro Nishino for their helpful advices and experimental facilities.

Appreciations are also due to the present and former members of Professor Kawabata's research group, Dr. Shinzo Ohnishi, Messrs. Takeshi Wada, Toshihiko Karasaki, Shinji Ikeda, and Hiroshi Kuroda, for their valuable participations in the work.

The author is very grateful to Dr. Yoshihiko Mizushima of Musashino Electrical Communication Laboratory, Nippon Telegraph and Telephone Public Corporation for the experimental facilities and encouragement.

One of the Te crystals used in this study was supplied by Professor J. C. Thuillier of CNRS, Faculté des Sciences Mirande, Dijon, France. The author is also indebted to Professor Yu. V. Gulyaev of Institute of Radioengineering and Electronics of Academy of Sciences, USSR for drawing his attention to the possibility of the peculiar acousto-optic phenomena described in Chap.3 in this thesis.

Part of this work was financially supported by the Grant-in-Aid for Scientific Research from the Ministry of Education, Science and Culture (No.075247, No.155116, No.375161, No.355147, and No.475222).

CONTENTS

CHAPTER 1

INTRODUCTION

1.1 Historical Background

The phenomenon of light diffraction by acoustic waves in liquids and solids has been extensively studied since the theoretical prediction by Brillouin in 1922 [1] and the first experimental verifications in 1932 by Debye and Sears [2] and by Lucas and Biquard [3]. This phenomenon is the one which is known as Brillouin scattering today, and such experiments were originally exploited to study thermal phonon distributions and elastic constants of various materials [4,5]. Brillouin's original theory predicted an optical diffraction analogous to x-ray diffraction in crystals: plane waves of light striking the acoustically induced periodic planes of density variations at a certain critical angle (Bragg angle) would be partially reflected. Furthermore, Brillouin's theory pointed out that the frequency of the reflected light will be Doppler-shifted by an amount equal to the acoustic frequency. Contrary to Brillouin's prediction, however, multiorder diffraction phenomenon was observed in the experiments utilizing low acoustic frequencies [3,6-8]. This multiorder diffraction phenomenon was well explained by the simple phase-grating theory developed by Raman and Nath (1935) [9], which is the most useful theoretical treatment made in the early stage of work. They established an infinite set of coupled-wave differential equations which are known as the Raman-Nath equations today. However, their original theory can be applied only to the case where the intensity of acoustic wave is not very strong and the interaction length is not very long.

Either when the acoustic frequency is sufficiently high or when the interaction length is sufficiently large, however, light intensity in the higher diffraction orders becomes negligibly small. In the extreme limit, only two modes, the zeroth and the positive (or negative) first order, need to be considered and the diffraction takes place only when the angle of incidence is very closely equal to the Bragg angle. This is the case which is known as Bragg diffraction and can be described by Brillouin's original theory. This type of diffraction was experimentally verified by Rytow (1935) [11] and Bhagavantam and Rao (1948) [10]. In 1956, Phariseau [12] modified the Raman-Nath theory in more intuitive way so as to treat the Bragg diffraction. A numerical treatment was made by Klein and Cook [13] to include more general cases where the Raman-Nath equations have no analytical solutions.

Since the advent of lasers for coherent light sources in the 1960's and the advances in piezoelectric transducer techniques for efficient excitation of ultrasonic waves, research in acousto-optic interactions received renewed attention from an applicational as well as physical point of view. Applications of acousto-optic phenomena to light modulation, deflection for optical communication, and signal processing have become practically important [14-20]. The several important works made since the advent of lasers are those by Gordon (1966) [21] on the efficiency and bandwidth of acousto-optic modulators and deflectors, by Korpel et al (1969) [14] on acoustic beem steering, by Dixon (1967) [22] on acousto-optic interactions in anisotropic media, and by Dixon and Cohen (1966) [23] on dynamic methods for the measurements of acousto-optic figure of merit.

For regards the selection of acousto-optic materials, Pinnow (1970) [24] and Uchida et al (1973) [25] have proposed systematic and practically useful guidelines. The acousto-optic materials which have been examined to date include liquid, amorphous, and

crystalline materials [25-27] for the use mainly in the visible or in the near-infrared region. The properties that are required of acousto-optic materials are good optical quality and high transmission, low acoustic losses at high rf frequencies, high acousto-optic figures of merit, good mechanical properties, high chemical stability, and availability in a large enough size.

Parallel with the above-mentioned works in the visible or in the near-infrared region, recent rapid progress made in high-efficiency CO_2 lasers at the infrared wavelength of 10.6μm has considerably enlarged the areas of practical application of this wavelength. Space communications, machining, laser radar, and nuclear fusion are some of the examples of current interest. As a result, the necessity of developing an efficient modulator and deflector for 10.6-μm radiation has become more and more imperative. However, the effort which has been made so far is a limited one compared with the large amount of work done in the visible and near-infrared regions. The most noteworthy candidates at present which satisfy the above requirements for acousto-optic materials at 10.6μm are (1) elemental semiconductors such as Ge, Si, and Te [26,28-31], (2) II-VI or III-V compounds such as CdS and GaAs [29], (3) amorphous chalcogenide crystals such as Tl_3AsS_4 and Tl_3PSe_4 [34,35]. However, the materials whose acousto-optic properties at 10.6μm have been investigated in detail to date are limited. Among them, only GaAs and Ge are practically used as acousto-optic media because of their well-established crystal-growth technology in addition to their relatively excellent acousto-optic properties. On the other hand, Dixon et al [36] pointed out the excellent properties of single-crystal Te as an acousto-optic medium. The figure of merit obtained by their measurements was as large as 4400×10^{-18} sec^3/g, and remains the largest value ever measured in these materials [26]. To our knowledge, however, a detailed study has not been made since that time. Amorphous Se is also of interest at 10.6μm because of the following

several characteristics which crystalline solids can hardly compete with [25]: (1) availability in large size and in arbitrary shape, (2) feasibility of annealing to attain optical homogeneity, (3) easiness in fabrication, and hence (4) low cost.

1.2 Organization of the Thesis

Taking the above-mentioned reasons into account, acousto-optic properties of single-crystal Te and amorphous Se at 10.6μm are investigated and discussed in detail from an applicational point of view in this thesis. The thesis is organized into the following chapters: In Chap.2, acousto-optic figures of merit and photoelastic constants of Te are determined by the Dixon-Cohen method, and its applicability as an acousto-optic medium is evaluated. Chapter 3 puts emphasis on peculiar acousto-optic phenomena resulting from the fact that Te simultaneously possesses both piezoelectricity and semiconductivity, that is, this chapter theoretically considers the possibility of optical diffraction arising from free-carrier density waves which accompany piezoelectrically active acoustic waves propagating in Te and the intensity of such diffraction is numerically evaluated. Finally, it is shown that an appreciable part of experimentally observed diffraction can be attributed to this mechanism. Chapter 4 describes an application of superior acousto-optic properties of Te to nonlinear optical effects and proposes a novel phase-matching technique utilizing acousto-optic interactions. Employing this phase-matching technique, relatively efficient optical second harmonic generation of a 10.6-μm light is experimentally demonstrated. Chapter 5 is devoted to the experimental determination of acousto-optic properties of amorphous Se, and practical applicability of this material to an acousto-optic medium for the use at 10.6μm is discussed. In Chap.6, feasibility

of amorphous Se as an optical-waveguide material at 10.6μm is experimentally shown. Based on this result, a photoelastic optical modulator with a guide structure is constructed, and its modulation characteristics are measured. The final chapter, Chap.7, summarizes the results and knowledge which are obtained from this work.

References

[1] L. Brillouin, Ann. Phys.(Paris), 9th ser. 17 (1922) 88.

[2] P. Debye and F. W. Sears, Proc. Nat. Acad. Sci. U.S. 18 (1932) 409.

[3] R. Lucas and P. Biquard, C. R. Acad. Sci. 194 (1932) 2132.

[4] M. Born and E. Wolf, *Principles of Optics* (Pergamon, New York, 1959).

[5] R. Pierls, *Quantum Theory of Solids* (Oxford, New York, 1955).

[6] O. Nomoto, Proc. Phys. Math. Soc. Jpn. 22 (1940) 314.

[7] F. H. Sanders, Can. J. Res. 14A (1936) 158.

[8] O. Nomoto, Proc. Phys. Math. Soc. Jpn. 24 (1942) 380.

[9] C. V. Raman and N. S. N. Nath, Proc. Indian Acad. Sci. 2A (1935) 406; 2A (1935) 413; 3A (1936) 75; 3A (1936) 119; and 4A (1937) 222.

[10] S. Bhagavantam and B. R. Rao, Proc. Indian Acad. Sci. 28A (1948) 54.

[11] S. M. Rytow, Phys. Z. Sowjetunion 8 (1935) 626.

[12] P. Phariseau, Proc. Indian Acad. Sci. 44A (1956) 165.

[13] W. R. Klein and B. D. Cook, IEEE Trans. Sonics Ultrason. SU-14 (1967) 123.

[14] A. Korpel, R. Adler, P. Desmares, and W. Watson, Proc. IEEE 54 (1966) 1429.

[15] A. Korpel, S. N. Lotsoff, and R. L. Whitman, Proc. IEEE 57 (1969) 160.

[16] L. K. Anderson, Bell Lab. Rec. 46 (1968) 318.

[17] J. T. LaMacchia, Laser Focus 6 (1970) 35.

[18] L. K. Anderson, Proc. 6th Int. Quantum Electronics Conf. (Kyoto, Sept. 1970).

[19] G. Hrbek and W. Watson, Proc. Electro-Optical Systems Design Conf. (New York, Sept. 1971) 271.

[20] A, W. Warner, D. L. White, and W. A. Bonner, J. Appl. Phys. 43 (1972) 4489.

[21] E. I. Gordon, Proc. IEEE 54 (1966) 1391.

[22] R. W. Dixon, IEEE J. Quantum Electron. QE-3 (1967) 85.

[23] R. W. Dixon and M. G. Cohen, Appl. Phys. Letters 8 (1966) 205.

[24] D. A. Pinnow, IEEE J. Quantum Electron. QE-6 (1970) 223.

[25] N. Uchida and N. Niizeki, Proc. IEEE 61 (1973) 1073.

[26] R. W. Dixon, J. Appl. Phys. 38 (1967) 5149.

[27] I. C. Chang, IEEE trans. Sonics Ultrason. SU-23 (1976) 2.

[28] R. L. Abrams and D. A. Pinnow, J. Appl. Phys. 41 (1970) 2765.

[29] H. R. Carleton and R. A. Soref, Appl. Phys. Letters 9 (1966) 110.

[30] S. Fukuda, T. Shiosaki, and A. Kawabata, Jpn. J. Appl. Phys. 15 (1976) 927.

[31] S. Fukuda, T. Shiosaki, and A. Kawabata, J. Appl. Phys. 50 (1979) 3899.

[32] S. Fukuda, T. Wada, T. Shiosaki, and A. Kawabata, Jpn. J. Appl. Phys. 16 (1977) 659.

[33] W. C. Schneider and K. Vedam, J. Opt. Soc. Am. 60 (1970) 800.

[34] M. Gottlieb, T. J. Isaacs, J. D. Feichtner, and G. W. Roland, J. Appl. Phys. 45 (1974) 5145.

[35] J. D. Feichtner, M. Gottlieb, and J. J. Conroy, Appl. Phys. Letters 34 (1979) 1.

[36] R. W. Dixon and A. N. Chester, Appl. Phys. Letters 9 (1966) 190.

CHAPTER 2

ACOUSTO-OPTIC PROPERTIES OF Te

2.1 Introduction

Recently the interest in elemental crystal Te has considerably increased as an active optical material for the use in the infrared. This is mainly because unlike most of other infrared materials, Te possesses the following peculiar properties: (1) transparency in the infrared, (2) exceptionally high refractive indices (the ordinary and extraordinary indices at 10.6 μm are respectively n_o = 4.7939 and n_e = 6.2433, and also see Fig.2.1-1) [18,53], (3) anomalously large optical nonlinearity [54],(4) strong piezoelectricity simultaneously along with semiconducting properties [55], (5) large optical as well as electrical anisotropy, and (6) availability in a large size of crystal. Te occupies the fifty-second place in the periodic table, and belongs to the VIb group. Crystallized Te has a peculiar hexagonal structure as illustrated in Fig.2.1-2. The Te atoms are arranged in spiral chains which are oriented along the z axis, each atom sharing covalent bonds with its two nearest neighbors in the chain. The chains are held together by a combination of Van der Waals and metallic bonds. The hexagonal lattice is constructed by locating each chain at the center and at each of the six corners of the hexagon. This hexagonal structure is readily revealed by cleaving a crystal because the relatively weak binding between chains easily generates planes of cleavage parallel to the z axis. The crystals have the D_3 (or 32) point group symmetry and belong to the trigonal system. The space group in the Schoenflies notation is denoted by either D_3^4 or D_3^6, corresponding to the right-handed and left-handed

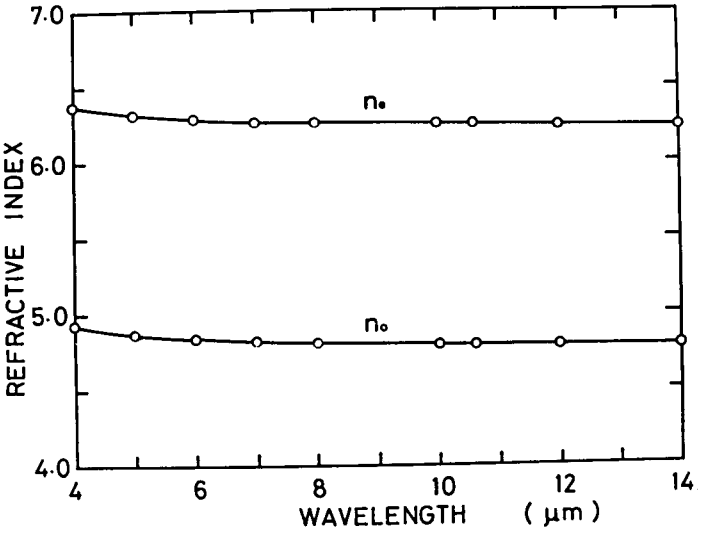

Fig.2.1-1 Wavelength dependence of refractive indices in Te [18].

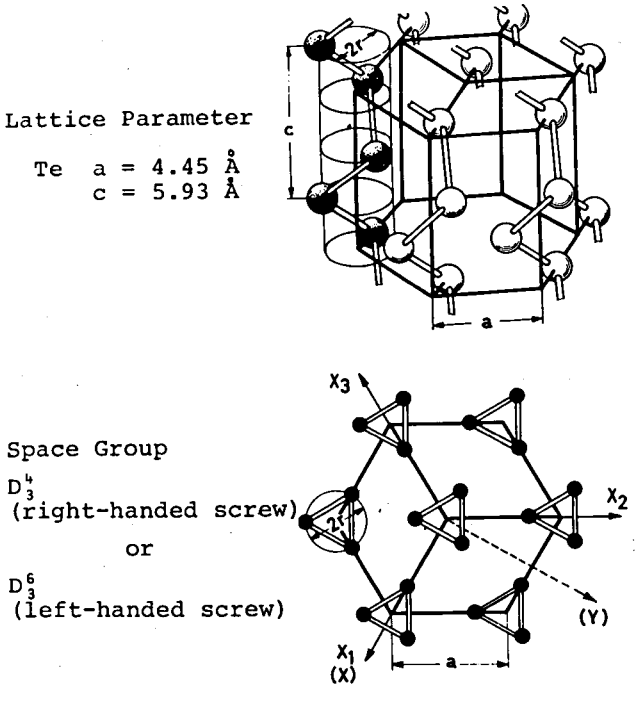

Fig.2.1-2 Structure of trigonal Te crystal.

spiral structures. The equivalent notation is $P3_121$ and $P3_221$ in the Hermann-Mauguin convention. The photoelastic and elastic tensors in Te are therefore expressed as [15]

$$\begin{vmatrix} p_{11} & p_{12} & p_{13} & p_{14} & 0 & 0 \\ p_{12} & p_{11} & p_{13} & -p_{14} & 0 & 0 \\ p_{31} & p_{31} & p_{33} & 0 & 0 & 0 \\ p_{41} & -p_{41} & 0 & p_{44} & 0 & 0 \\ 0 & 0 & 0 & 0 & p_{44} & p_{41} \\ 0 & 0 & 0 & 0 & p_{14} & \frac{1}{2}(p_{11}-p_{12}) \end{vmatrix} \qquad (2.1\text{-}1)$$

(8 independent components)

and

$$\begin{vmatrix} c_{11} & c_{12} & c_{13} & c_{14} & 0 & 0 \\ c_{12} & c_{11} & c_{13} & -c_{14} & 0 & 0 \\ c_{13} & c_{13} & c_{33} & 0 & 0 & 0 \\ c_{14} & -c_{14} & 0 & c_{44} & 0 & 0 \\ 0 & 0 & 0 & 0 & c_{44} & c_{14} \\ 0 & 0 & 0 & 0 & c_{14} & \frac{1}{2}(c_{11}-c_{12}) \end{vmatrix}, \qquad (2.1\text{-}2)$$

(6 independent components)

where the matrix notations are employed.

Since Dixon's measurements in 1966 [13], crystalline Te has been considered as one of the most promising acousto-optic materials at 10.6μm because the most of the physical properties required of efficient acousto-optic materials are expected to be satisfied in Te. Based on this expectation, acousto-optic properties of Te are studied in detail in this chapter and its feasibility of practical applications is evaluated.

2.2 Determination of Figures of Merit and Photoelastic Constants by the Dixon-Cohen Method

In general, two kinds of methods have been usually employed to determine photoelastic constants of materials [1]. One is a static method and was mainly used in the earlier stage of photoelastic studies [2-6], while the other is dynamic in nature and was widely used in more recent years [7-10]. In the dynamic methods, the intensity of acousto-optically diffracted light from an acoustic-wave pulse propagating in a standard reference material, usually water or fused quartz, is compared with the light diffracted from a similar acoustic pulse propagating in a sample bonded to the reference material. The ratio of these two light intensities determines the figure of merit M (a measure of the inherent diffraction efficiency of material as defined by Eq.(2.2-4) below, and also see Appendix) of the sample with respect to the standard material. Knowing the parameters appearing in M then enables one to derive a value for the photoelastic constant. The most simple and accurate such technique is the one proposed and discussed by Dixon and Cohen [10]. It should however be noted that with the dynamic method, it is generally not possible to determine the sign of the photoelastic constans. The acousto-optic measurements for Te which are described below were carried out by the Dixon-Cohen method.

The Te single crystals measured were grown by the Bridgman method [11] or by the gradual cooling method [12]. The samples were mechanically cut with a string saw and then polished into rectangular shape. After polishing, the samples were etched by concentrated sulphuric acid at 100°C and then annealed at 300 - 350°C for about 3 days in order to remove lattice defects induced during the crystal-growth and successive process. Finally, after the samples were subjected to the second surface-polishing with 0.3-μm aluminum oxide powder, slight chemical etching with concentrated sulphuric acid was again

carried out to eliminate a surface damage layer. This etching process is essentially important in Te because optical absorption within the surface damage layer often seriously reduces its infrared transparency. Since crystalline Te is relatively soft (about 2.5Mohs), great care was devoted to minimize a possible occurrence of damage during mechanical handling like cutting and abrasion. The parallelepiped size of the samples was about $x \times y \times z = 1 \times 1 \times 1.5$cm. The surface orientations were determined with respect to the cleavage plane (the $(10\bar{1}0)$, and hence, y plane) and believed to coincide properly with the corresponding crystallographic planes within an accuracy of much less than 1°. The electrical conductivity at room temperature was about 1.5 $(\Omega\,\mathrm{cm})^{-1}$ along the z axis and about 2.5 $(\Omega\,\mathrm{cm})^{-1}$ perpendicular to the z axis, repectively.

The experimental procedures were essentially the same as those used by Dixon et al [10, 13] for longitudinal acoustic waves propagating in the x direction in Te. Figure 2.2-1 shows a plot of the variation of acoustic phase velocities in Te as a function of propagation direction in the x - z and y - z planes. θ is the angle between the propagation direction and the z axis. These curves were numerically calculated using the Christoffel secular equation [14-16] and the values for the elastic constants of Te at 300°K. The elastic constants used in the calculation were determined, as listed in Table 2.1, from the following formulas due to Malgrange et al [17].

$$\begin{aligned} c_{11} &= 3.76 - 1.65 \times 10^{-3}\,T\,, & c_{12} &= 0.924 - 0.23 \times 10^{-3}\,T\,, \\ c_{13} &= 2.88 - 1.29 \times 10^{-3}\,T\,, & |c_{14}| &= 1.43 - 0.645 \times 10^{-3}\,T\,, \\ c_{33} &= 7.85 - 2.10 \times 10^{-3}\,T\,, & c_{44} &= 3.55 - 1.43 \times 10^{-3}\,T\,, \end{aligned} \qquad (2.2\text{-}1)$$

where T is the absolute temperature and c_{ij}'s are measured in the unit of $10^{10}\,\mathrm{N/m^2}$. The points indicated by the symbols L and S in Fig.2.2-1 denote the propagation directions of longitudinal waves and shear waves, respectively. The acoustic wave propagates as a

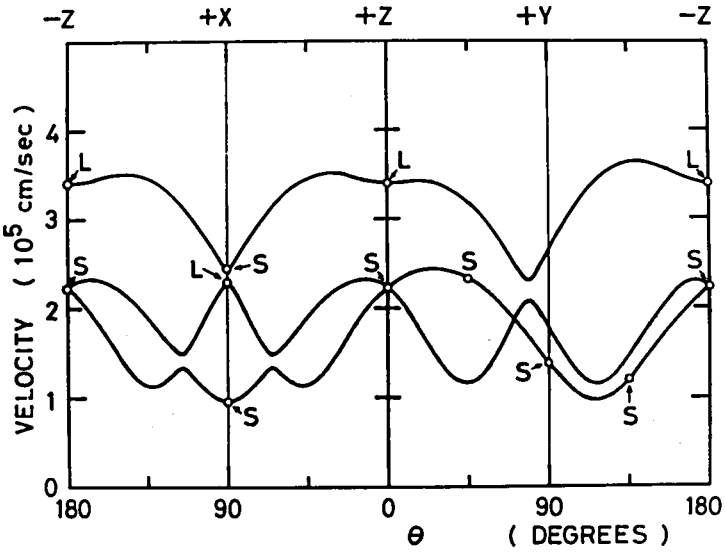

Fig.2.2-1 Variation of acoustic phase velocity in Te as a function of propagation direction in the x-z and y-z planes. θ is the angle between the propagation direction and the z axis. The symbols L and S denote the direction of a longitudinal mode and a shear mode, respectively.

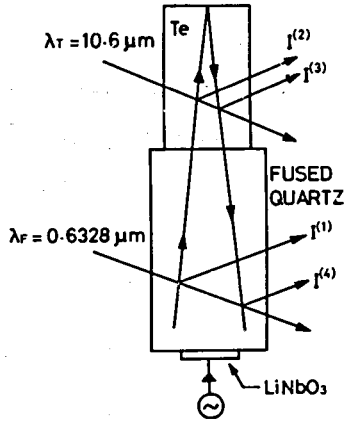

Fig.2.2-2 Dixon-Cohen method.

Table 2.1 Elastic constants of Te (300°K).

c_{11}	c_{12}	c_{13}	$\lvert c_{14} \rvert$	c_{33}	c_{44}
3.27	0.86	2.49	1.24	7.22	3.12

c_{ij} in the unit of 10^{10} N/m^2, ρ = 6.25 g/cm^3 .

quasimode in the other directions. In the present experiments, two pure longitudinal waves that have an energy flow in the same direction as the wave propagation were chosen because of the limitations of the sample size and to make the measurements and the following analysis less complicated: The first is a longitudinal wave propagating along the x axis with the velocity of 2.29×10^5 cm/sec and the second is a longitudinal wave propagating along the z axis with the velocity of 3.40×10^5 cm/sec.

Figure 2.2-2 shows the schematic illustration of the Dixon-Cohen method employed in the measurements. A fused quartz buffer rod was used as a standard reference material. Two 36°-rotated y-cut $LiNbO_3$ transducers with fundamental frequencies of 28 and 42 MHz were alternately bonded to the buffer rod to generate the above longitudinal waves. The experiments were carried out using these fundamental frequencies and their third overtones. The acoustic contact between the Te samples and the fused quartz was achieved by phenylsalicylate or epoxy resin bonds. Coherent light sources were a 0.6328-μm He-Ne laser for the fused quartz and a 10.6-μm *cw* CO_2 laser for the Te samples. The incident linearly polarized CO_2 laser beam had a well-collimated spot diameter of about 1 mm at the sample input face. The direction of the polarization was adjusted by rotating a NaCl Brewster plate inserted in the laser cavity. Since the optical losses for an extraordinarily polarized light (i.e., $\vec{E} \,//\, \vec{z}$-axis) in Te increase rapidly with increasing temperature due to the intervalence band transition located at 11 μm [18,19], the incident optical power was carefully maintained at less than a few hundred mW using an optical attenuator constructed with silicon plates to avoid an increase in the sample temperature due to optical absorption. The 10.6-μm light was detected by a HgCdTe photoconductive infrared detector FUJITSU HC050C4.

When the ratio of the first-order diffracted light intensity to that of the zeroth order without the acoustic field, I_1 / I_0, is much

less than unity, Eq.(A-34) in Appendix can be approximated as

$$I_1 = I_0 \, (\pi^2 / 2 \lambda_0^2) (L/H) \, M P_A \, . \qquad (2.2\text{-}2)$$

where λ_0 is the wavelength of the incident light in vacuum, L and H are the width and height of the acoustic beam, and M is the figure of merit of the material. Therefore, the first-order diffracted intensity I_1 is proportional to the acoustic power P_A, and hence, to the input electrical power applied to the transducer. For the geometry shown in Fig.2.2-2 under such conditions, we have Eq. (2.2-3) as below for the figures of merit M_T and M_F [13]:

$$M_T / M_F = (\lambda_T/\lambda_F)^2 \, [\, I^{(2)} . I^{(3)} / I^{(1)} . I^{(4)} \,]^{1/2} \qquad (2.2\text{-}3)$$

and

$$M = n^6 \, p^2 / \rho \, v^3 \qquad (2.2\text{-}4)$$

with $\lambda_T = 10.6 \, \mu m$ and $\lambda_F = 0.6328 \, \mu m$, where the subscripts T and F stand for Te and the fused quartz, λ's are the optical wavelengths in vacuum, n is the refractive index, p is the photoelastic constant, ρ is the density, and v is the acoustic velocity. As shown in Fig.2.2-2, $I^{(2)}$ and $I^{(3)}$ are the relative first-order diffracted light intensities for Te due to the acoustic pulse outgoing from the transducer and due to the pulse reflected from the free end of the Te, respectively. Similarly, $I^{(1)}$ and $I^{(4)}$ are the relative first-order diffracted intensities for the fused quartz due to the outgoing pulse and due to the reflected pulse, respectively. The value of $[\, I^{(2)} . I^{(3)} / I^{(1)} . I^{(4)} \,]^{1/2}$ does not depend on the quality of the bond at the interface between Te and the fused quartz, nor on the acoustic loss in the materials provided only that the acoustic transmission through the bond is reciprocal. Consequently, the figure of merit M_T for Te is determined from the measurements

of $I^{(1)}$, $I^{(2)}$, $I^{(3)}$, and $I^{(4)}$ with the standard value for M_F ($= 1.56 \times 10^{-18}\,\mathrm{sec}^3/\mathrm{g}$) .

2.3 Experimental Results

Figure 2.3-1 shows one of the results obtained by the Dixon-Cohen method for longitudinal acoustic waves propagating along the z axis, where the incident 10.6-μm light was transmitted in the y direction with the polarization parallel to the x axis. The linear dependence of $I^{(1)}$, $I^{(2)}$, $I^{(3)}$, and $I^{(4)}$ on the input electrical power applied to the piezoelectric transducer assures the validity of the application of Eq.(2.2-3). The calculation employing the method of least squares gives $M_T / M_F = 670$, and hence, $M_T = 1050 \times 10^{-18}\mathrm{sec}^3/\mathrm{g}$. The photoelastic tensor components relating to the diffraction geometry are p_{13} for Te and p_{12} for the fused-quartz.

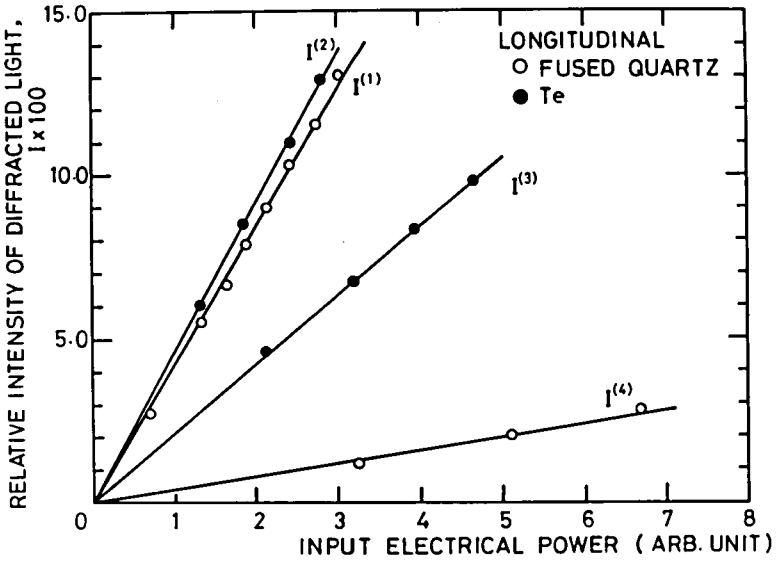

Fig.2.3-1 Relations between relative intensity of the first-order diffracted light and electrical input power applied to the transducer.

Table 2.2 Acousto-optic properties of Te.

Acoustic wave		Optical wave (10.6 μm)				Figures of merit		
Polarization and propagation direction	Velocity v (10^5 cm/sec)	Incident direction	Polarization direction	Refractive index n	p_{ij}	M (sec^3/g)	M' (cm^3 sec/g)	M'' (cm sec^2/g)
Long. in x	2.29	y	x	4.7939	p_{11}	4360×10^{-18} 4400 (Dixon)	11000×10^{-7} 10200 (Dixon)	4790×10^{-12} 4640 (Dixon)
		z	y	4.7939	p_{12}	3090	7770	3390
		y	z	6.2433	p_{31}	5850	19200	8360
Long. in z	3.40	y	x	4.7939	p_{13}	1050	5820	1710
		y	z	6.2433	p_{33}	368	2660	781

$\rho = 6.25\ g/cm^3$, $M = n^6\ p^2/\rho\ v^3$, $M' = n^7\ p^2/\rho\ v$, and $M'' = n^7\ p^2/\rho\ v^2$.

The other figures of merit determined by the similar procedures are tabulated in Table 2.2 together with the results obtained by Dixon [20]. The photoelastic components relating to the diffraction are also shown in Table 2.2. In what follows, we shall adopt the notation M_{ij} as the relevant figure of merit for the photoelastic component p_{ij}. In the results determined for longitudinal waves in the x dirction, the value of $4360 \times 10^{-18} sec^3/g$ obtained for M_{11} is in good agreement with the value reported by Dixon within the estimated experimental error of less than 15 %. In order to check the accuracy of the above-obtained M_{31}, the value for M_{31} relative to that for M_{11} was re-estimated by measuring the change in the relative diffracted light intensity occurring when the polarization direction of the incident light was rotated by 90° from the x to the z direction keeping other configurations and conditions the same. In this measurement, the transducer had been bonded directly onto the x face of the Te sample. The obtained I *vs* P_A relations are shown in Fig.2.3-2. The calculation using Eq.(2.2-2) reveals that the ratio of M_{31} to

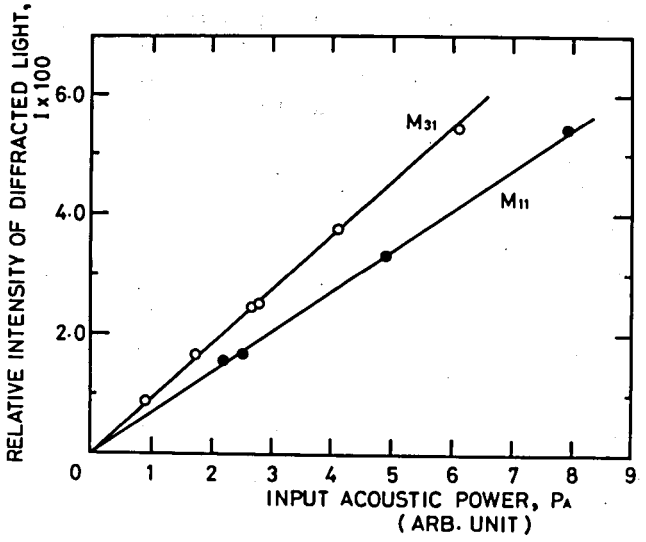

Fig.2.3-2 Relations between relative intensity of the first-order diffracted light and input acoustic power.

M_{11} coincides very closely with that obtained by the Dixon-Cohen method. In a similar way, the ratio of M_{33} to M_{13} was also re-estimated by rotating the polarization of the incident light by 90°, maintaining other conditions the same. The obtained I *vs* P_A characteristics are shown in Fig.2.3-3, from which we have $M_{13}/M_{33} = 2.86$, being in fair agreement with the values in Table 2.2.

The theory given in Appendix shows that the diffraction efficiency η (defined as I_1 / I_0 of Eq.(2.2-2)) of an acousto-optic device decreases with increasing optical wavelength since in the Bragg limit, η is a sine function of a quantity inversely proportional to λ_0^2 [21]. From a practical point of view, therefore, the existence of an acousto-optic material with a large figure of merit is much more imperative in the infrared region than in the visible. The present experimental results have revealed that Te possesses large enough figures of merit to compensate for the above reduction in the efficiency due to the longer operating wavelength. As understood from Eq.(2.2-4), this is mainly a result of its relatively

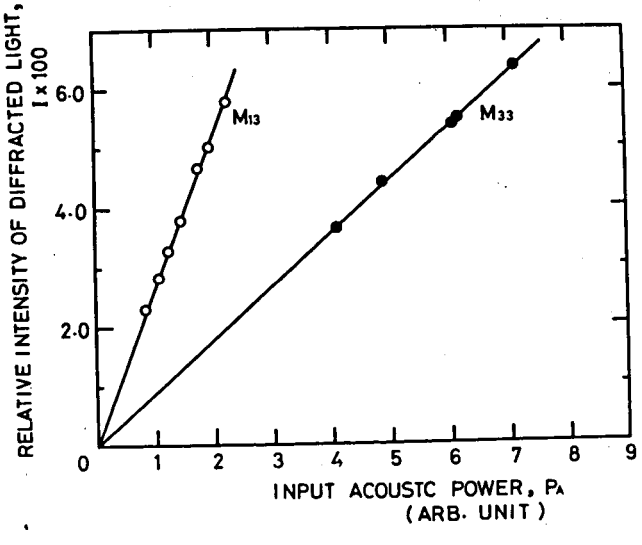

Fig.2.3-3 Relations between relative intensity of the first-order diffracted light and input acoustic power.

slow acoustic velocities and anomalously large refractive indices. For example, in the figures of merit obtained for a longitudinal acoustic wave propagating in the x direction, the value of $5850 \times 10^{-18} \text{sec}^3/\text{g}$ for M_{31} is the largest ever reported, where the relevant refractive index and acoustic velocity are $n_e = 6.2433$ and $v = 2.29 \times 10^5$ cm/sec, respectively. Under these geometrical conditions, a calculation employing Eq.(A-34) in Appendix shows that the acoustic power required to deflect all the incident 10.6-μm light is only 9.6 W when the cross section of the acoustic beam is assumed square. On the whole, the figures of merit relating to the acoustic wave propagating in the x direction are larger than those for the acoustic wave in the z direction. This is due mostly to the difference of the two acoustic velocities.

The figure of merit M defined by Eq.(2.2-4) which has been referred to above is only a measure of the inherent diffraction efficiency of the material, independent of geometry or other factors. Besides the values of M, Table 2.2 also tabulates the calculated values for two other commonly used figures of merit M' and M'' . The second figure of merit,

$$M' = n^7 p^2 / \rho v , \tag{2.3-1}$$

was introduced by Gordon for the specific device applications in which the diffraction bandwidth as well as the diffraction efficiency is important [22]. The third figure of merit,

$$M'' = n^7 p^2 / \rho v^2 , \tag{2.3-2}$$

was defined by Dixon [20] for the case where the acoustic beam height is as small as the optical beam diamerer. It is noted that all the figures of merit except those relating to p_{33} have exceptionally large values in Te. (See also Fig.2.6-2.)

On the other hand, Te has some drawbacks as an acousto-optic

Table 2.3 Photoelastic constants of Te.

p_{11}	p_{12}	p_{13}	p_{31}	p_{33}	p_{14}	p_{41}	p_{44}
0.164	0.138	0.146	0.086	0.038	-	-	-
0.155[a]	0.130[a]						

[a] The values determined by Dixon [20].

medium. One of them is its relatively high acoustic attenuation as will be discussed in Sec.2.6. The other is the fact that the optical absorption for extraordinarily polarized light at 10.6 μm is not very small except when the material is cooled, due to an absorption band centered at 11 μm [18,19]. In our crystal, the absorption coefficient for extraordinarily polarized light at 10.6 μm was about 4 cm^{-1} at room temperature, while it was about 0.5 cm^{-1} for ordinarily polarized light. In spite of these drawbacks, however, the large values of the figures of merit still make Te very attractive for device applications in the infrared region.

Utilizing Eq.(2.2-4), five of the eight independent Pockels photoelastic tensor components of Te were calculated from the above-obtained figures of merit and are listed in Table 2.3 togther with Dixon's values [20]. Since the measurements by the Dixon-Cohen method inherently yield only a numerical value for a photoelastic constant, the absolute signs are still indeterminate. The estimated experimental error is less than 15 % for all the constants except for p_{12}, which is influenced by optical activity as discussed in the next section. A large part of the experimental error is due to the imperfection of the experimental arrangement. Since the 10.6-μm laser beam was invisible, it was not easy to satisfy the phase-matching conditions (or equivalently, the Bragg conditions) required for the acousto-optic diffraction precisely.

For the determination of the rest of the independent photo-

elastic constants (i.e., p_{14} , p_{41} , and p_{44}), it would be necessary to work with anisotropic Bragg diffraction. However, since the birefringence of Te is exceptionally large (about 160 times that of α-quartz crystal), the acoustic frequencies required for these measurements become so high that the increase in the acoustic loss would preclude the precise determination of those constants.

2.4 Influence of Optical Activity

When linearly polarized monochromatic light is transmitted through certain isotropic materials it is sometimes found that the plane of polarization is rotated as the light is propagated through the materials [2]. This is the phenomenon known as optical activity or optical rotation. For the linearly polarized light incident upon anisotropic crystals like Te, which have both optical activity and birefringence, the emergent light is in general elliptically polarized by the birefringence and the major axis of the ellipse is rotated out of the incident plane of polarization by the optical activity. The existence of the birefringence has its effect only on the shape of the ellipse, and the direction of its major axis is determined only by the optical activity.

As mentioned in Sec.2.1, Te crystal has a peculiar spiral structure belonging to an enantiomorphous class and therefore shows strong optical activity [23-28]. However, since the birefringence in Te is anomalously large, the effect of the optical activity is considerably masked by the birefringence for a linearly polarized incident light transmitting at an angle to the optic axis (and hence, the z axis). Consequently, the optical activity can be observed only when the incident light is transmitted very closely to the optic axis where the ordinary birefrigence vanishes [2].

The specific rotatory power β (defined as the rotation angle

of the polarization plane per unit transmission length) due to the optical activity in Te was measured for the first time by Nomura [23] and the existence of both levo- and dextrorotatory crystals was experimentally demonstrated at the wavelengths between 4 and 7 μm. In his results, however, there exists a considerable discrepancy between the magnitude of the levorotatory power and that of the dextrorotatory power even at the same wavelength, i.e., the dextrorotatory power is always less than the levorotatory power. This is shown by the solid curves in Fig.2.4-1. As in the case of α-quartz, it is the above-mentioned enantiomorphous spiral structure that is responsible for the optical activity, the individual Te atoms themselves being of course optically inactive. Furthermore, both kinds of enantiomorphous crystals, i.e., D_3^4 and D_3^6 have exactly the same Bravais lattice, except for their handedness. Consequently, the above discrepancy in Nomura's results seems to be quite unreasonable.

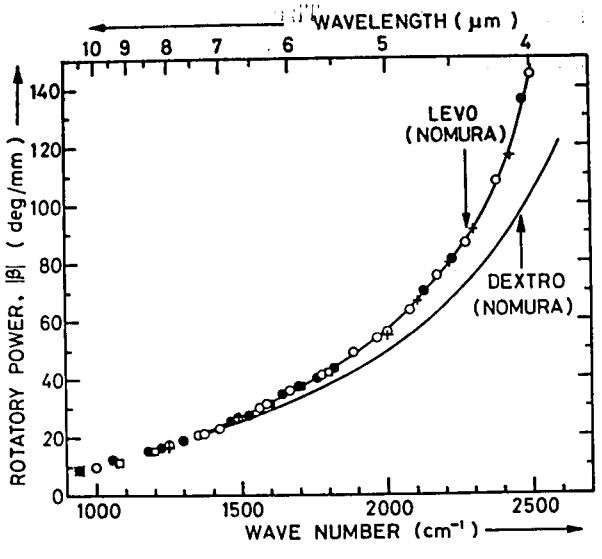

Fig.2.4-1 Dispersion of the optical rotatory power along the z axis in Te. The solid curves are the results obtained by Nomura [23]. The signs of the dextro- and the levorotatory powers are negative and positive, respectively; thickness (dextrorotatory) O 0.655 mm, ● 1.058 mm; thickness (levorotatory): + 0.630 mm, □ 0.650 mm, X 0.798 mm.

Natori [29,30] developed the general theory of the optical activity based on the electronic energy band theory. He applied this theory to Te and showed that most part of the optical rotatory dispersion of Te crystal could be explained by the k-linear term in the E versus k relation near the point H of the Brillouin zone, leading to the conclusion that the discrepancy in Nomura's results should be attributed to experimental error.

In the determinations of M_{12} and p_{12} as described in Sec.2.3, a question arose about the effects of the optical activity since the incident and the diffracted lights were transmitted nearly along the optic axis (or the z axis). To make this point clear, the specific rotatory power β was measured using two dextrorotatory and three levorotatory Te crystals [2,25]. The Te crystals measured were grown by the Bridgman method. The handedness of the crystals was determined from the etch pits produced on the cleavage plane by concentrated sulphuric acid at 100°C [32,33]. Because the shapes of the etch pits on levo- and dextrorotatory crystals are mirror images of each other as shown in Fig.2.4-2, the two types of crystals can be easily distinguished from each other [31]. The samples were mechanically cut and polished into thin plates with the plane-

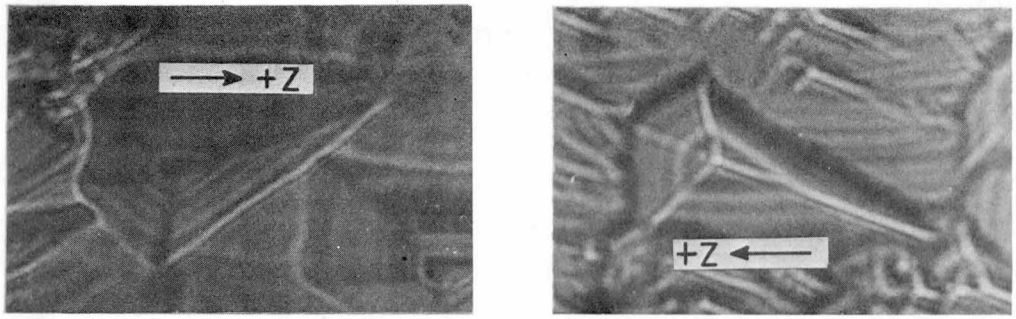

(a) (b)

Fig.2.4-2 Etch pits produced on the cleavage plane. (a) Dextrorotatory crystal; (b) Levorotatory crystal.

parallel faces oriented on the (0001) plane. The orientation of the sample faces was determined with an accuracy of better than 0.5° with repect to the (0001) plane. The measurements were performed using a Jasco, Model SS-50, single-beam infrared spectrometer at wavelengths between 4.0 and 9.0 μm, and a CO_2 laser at 10.6 μm. Linearly polarized radiation was produced using a AgCl polarizer. The angle of rotation of the polarization plane due to optical activity was measured with a Se thin-film polarizer [34-36] constructed by the present author.

Figure 2.4-1 shows the dispersion of the specific rotatory power β measured along the z axis. The signs of the dextro- and levorotatory powers are negative and positive, respectively, according to the conventional definition [2]. The values obtained are believed to be accurate within $\pm$ 1.5 deg/mm at wavelength between 4.0 and 9.0 μm, and within $\pm$ 0.2 deg/mm at 10.6 μm. The rotatory power at 10.6 μm was thus determined as $|\beta| = 9.0 \pm 0.2$ deg/mm. In contrast to Nomura [23], the results obtained here confirm that the levo- and the dextrorotatory powers coincide fairly well with each other in their magnitudes, which may obviously allow us to conclude that there exists no substantial difference between the two kinds of rotatory powers, except for their signs. The dispersion data obtained here show an excellent agreement with the levorotatory curve given by Nomura.

It is known that the rotatory power of nonmetallic materials along the optic axis in the low-absorption region is represented by the following phenomenological Chandrasekhar dispersion formula based on the classical coupled-oscillator model [37, 38]:

$$\beta = \sum_r \frac{k_r \lambda^2}{(\lambda^2 - \lambda_r^2)^2} \qquad \text{(rad/mm)},$$

where k_r is a constant corresponding to the characteristic absorp-

tion wavelength λ_r in μm, the summation being performed over all the r absorption wavelengths. It is found from the present results that the rotatory dispersion of Te is also well represented by the Chandrasekhar formula with two oscillators. The constants that fit the experimental data (except for wavelengths shorter than 4.3 μm) are

$$\lambda_1 = 2.563\ \mu m, \qquad \lambda_2 = 1.141\ \mu m,$$

$$k_1 = 9.66, \text{ and } k_2 = 9.42.$$

In an optically uniaxial crystal such as Te, the light transmitted in a general direction is, in general, broken up into two elliptically polarized waves that travel with different velocities. The simple way to estimate the effects of the optical activity on the acousto-optic diffraction is to investigate the ellipticity γ (the ratio of the minor to the major axis) of these two wave components. In Te, γ depends only on the angle, θ, between the wave normal and the optic axis as

$$\gamma = \tan\left[\frac{1}{2}\tan^{-1}\left(\left(g_{11}\sin^2\theta + g_{33}\cos^2\theta\right)\frac{x^{3/4}}{n_o^3(1-x^{1/2})}\right)\right] \qquad (2.4\text{-}1)$$

and

$$x = \cos^2\theta + (n_o/n_e)^2\sin^2\theta\,, \qquad (2.4\text{-}2)$$

where g_{11} and g_{33} are the components of a gyration tensor, and n_o and n_e are the ordinary and extraordinary refractive indices, respectively. The following relation holds between the gyration g_{33} and the rotatory power β [2]:

$$g_{33} = \lambda_0\, n_o\, \beta/\pi\,. \qquad (2.4\text{-}3)$$

Figure 2.4-3 shows the dispersion of the gyration tensor component $|g_{33}|$ which is calculated according to Eq.(2.4-3) using the specific rotatory power data given in Fig.2.4-1 and the refractive indices determined by Caldwell et al [18]. In this way, we have $|g_{33}| = (2.54 \pm 0.06) \times 10^{-3}$ at 10.6 μm. Though the actual magnitude of g_{11} is still unknown, the first term $g_{11} \sin^2\theta$ in the small parentheses on the right-hand side of Eq.(2.4-1) can be dropped because we are interested in the behavior only in the vicinity of the optic axis ($\sin^2\theta \ll 1$). Calculation of Eq.(2.4-1) with this approximation yeilds the dependence of the ellipticity γ on θ as in Fig. 2.4-4. The light transmitted exactly along the optic axis splits into two circularly polarized components with $\gamma = 1$. For θ larger than several degrees, γ rapidly approaches zero, and the two wave components are very closely linearly polarized.

Exactly speaking, in the measurements of M_{12}, the propagation direction of the incident and the diffracted light actually differs from the optic axis by the magnitude of the Bragg angle θ_B as

$$\theta_B = \sin^{-1}(\lambda_0 f/2nv) , \qquad (2.4-4)$$

Because a photoelastic constant p_{ij} is a quantity defined with respect to a linearly polarized wave, there arises some deterioration in the accuracy of the deduced value for p_{12} due to the existence of the optical activity. For obtaining an accurate result, the propagation directions of both the incident and diffracted lights must be inclined from the optic axis as far as possible by utilizing a large Bragg angle. For an 84 MHz longitudinal wave in the x direction which was used in the measurements for M_{12}, Eq.(2.4-4) yields $\theta_B = 2.3°$ and M_{12} was determined to be 3090×10^{-18} sec^3/g . Though the ellipticity corresponding to this θ_B is small, $\gamma \simeq 0.14$, the light is not strictly linearly polarized. Therefore, the corresponding p_{12} contains a small additional error in the determined value due to

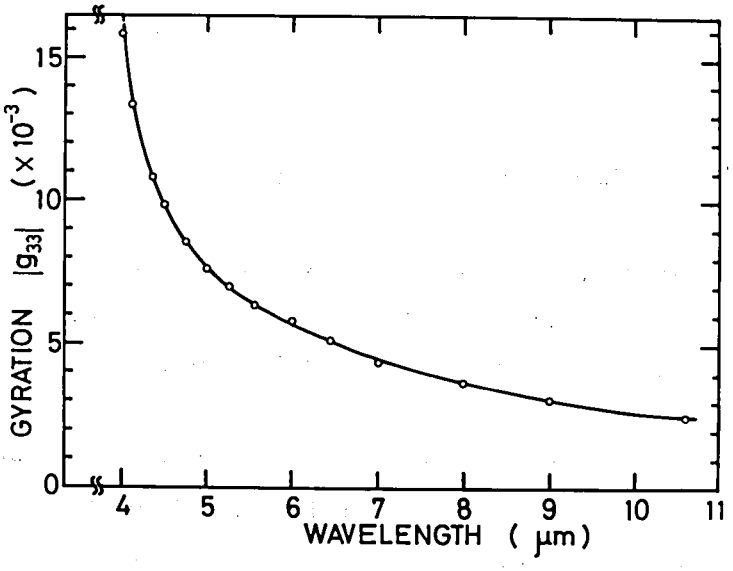

Fig.2.4-3 Dispersion of the gyration tensor component $|g_{33}|$ in Te.

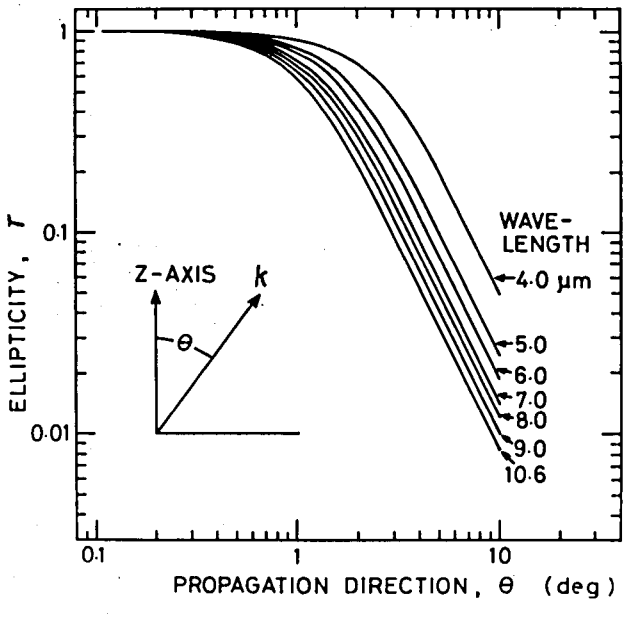

Fig.2.4-4 Dependence of ellipticity on propagation direction.

the optical activity. Thus, the total error for p_{12} is estimated as less than 25 %.

2.5 Application to Acousto-Optic Deflector

One of the most important device applications of acousto-optic effect in a medium is a light deflector. There have been several methods of deflecting a light beam to a given position in a space. The techniques may be divided into three groups [21]: mechanical electro-optic, and acousto-optic ones. Among them, the acousto-optic deflector has the following several advantages [21]: (1)capability of rather high capacity of signal processing, (2) ease in control of deflection modes and position, (3) simple structure of deflector element, and (4) wide variety of usage.

Figures 2.5-1 (a) and (b) show a schematic illustration and photograph of the Te acousto-optic light deflector fabricated for

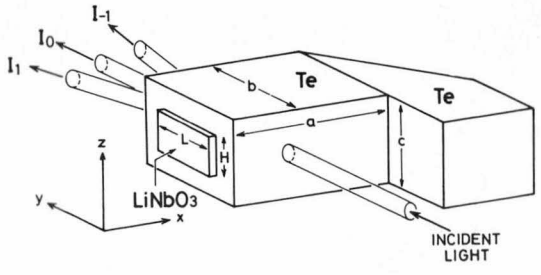

(a)

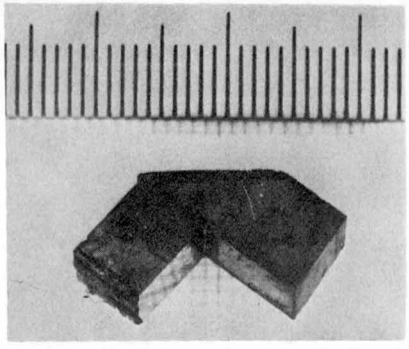

(b)

Fig.2.5-1 A schematic illustration (a) and photograph (b) of a Te acousto-optic light deflector fabricated for the use at 10.6 μm. The coordinate axes denote the crystallographic orientation for the Te crystal. The element sizes are $a \times b \times c = 5.89 \times 6.61 \times 5.49$ mm for the Te crystal and $L \times H = 5.06 \times 4.12$ mm for the $LiNbO_3$ transducer (36°-rotated y cut. The fundamental frequency is 13 MHz). A piece of a Te crystal is cemented as an acoustic absorber.

10.6-μm radiation, based on the experimental results described in Sec.2.3. The coordinate axes denote the crystallographic orientation of the Te crystal. The element size is $a = 5.89$ mm along the x axis, $b = 6.61$ mm along the y axis, and $c = 5.49$ mm along the z axis. The longitudinal wave in the x direction was produced by bonding a 36°-rotated y-cut $LiNbO_3$ transducer on the x face with epoxy resin. The fundamental frequency and the size of the transducer are 13 MHz and $L \times H = 5.06 \times 4.12$ mm, respectively. A piece of a Te crystal obliquely cut and polished was cemented onto the opposite face as an acoustic absorber. Figure 2.5-2 shows the 13-MHz rf-electrical input pulse applied to the transducer and the first-order diffracted light pulse. The suppression of the reflected acoustic wave by the use of the absorber was about 10 dB.

As described in Appendix, a useful criterion to determine in which regime (Bragg or Raman-Nath) an acousto-optic deflector operates was given by Klein and Cook [39] as the value of $Q = K^2 L/k$, where K and k are the wave number of the acoustic wave and the light in the medium, respectively. For a center frequency of 13 MHz and ordinarily polarized incident light, $Q = 2.26$. Therefore, the diffraction occurs in the transition region near the Raman-Nath region.

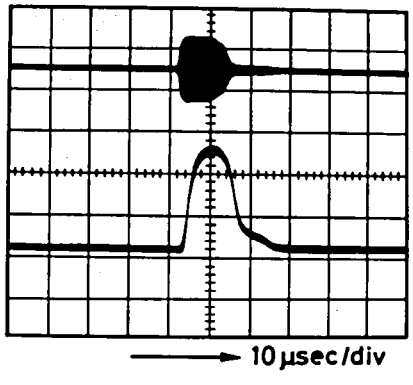

Fig.2.5-2 The wave forms obtained with the Te acousto-optic deflector. The upper trace is the electrical rf pulse applied to the transducer. The lower is the first-order diffracted optical signal.

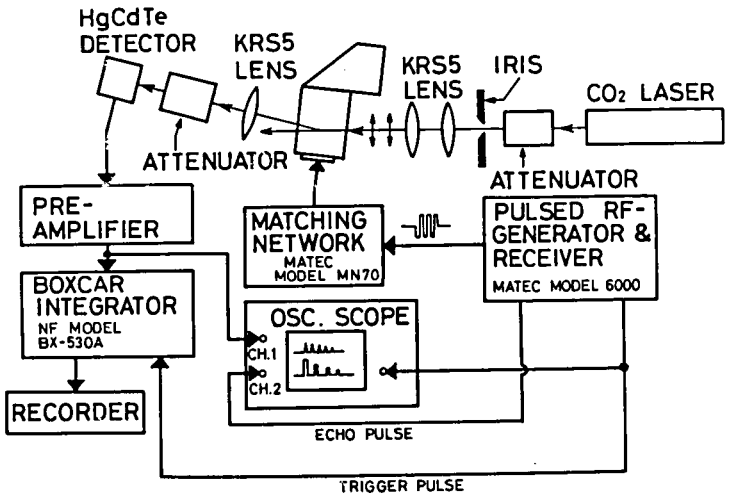

Fig.2.5-3 Arrangement for the diffraction experiments.

Figure 2.5-3 illustrates the arrangement for the diffraction experiments. Figure 2.5-4 shows the angular distribution of the diffracted light which was obtained when the input light was incident normal to the x-z plane with the polarization parallel to the x axis. Figure 2.5-5 plots the measured diffraction angles, where the theoretical curves are obtained from Eq.(A-13) in Appendix with $\theta_0 = 0$. The existence of diffracted light from the negative third to the positive third order confirms that the operation was actually performed in the transition region. The diffracted light intensity of the first order is shown in Fig.2.5-6 as a function of the input acoustic power. The solid curve indicates the theoretical result obtained from the numerical calculation employing the Klein-Cook analysis under $Q = 2.26$, as given in Appendix [39]. The electrical impedance of the transducer was matched to the 50 Ω electrical source through the MATEC matching network MODEL MN70. The figure of merit corresponding to this diffraction geometry is $M_{11} = 4360 \times 10^{-18}$ sec^3/g.

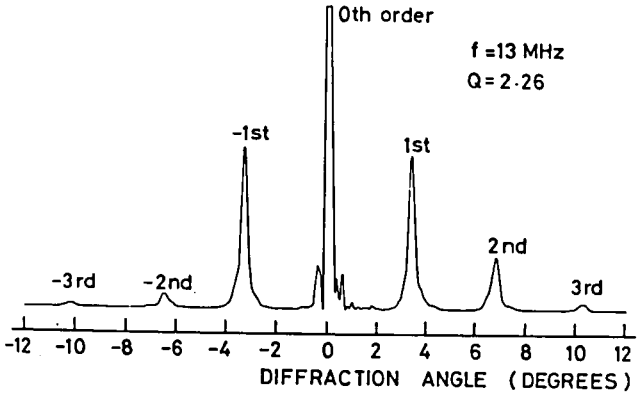

Fig.2.5-4 Angular distribution of the diffracted light intensities.
The angles were measured outside the medium.

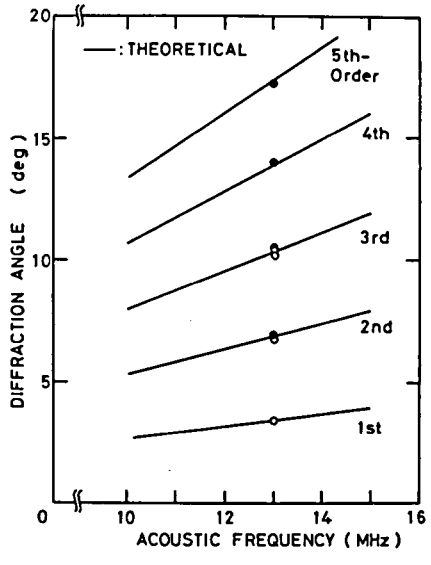

Fig.2.5-5 Relation between the measured diffraction angles and the calculation.

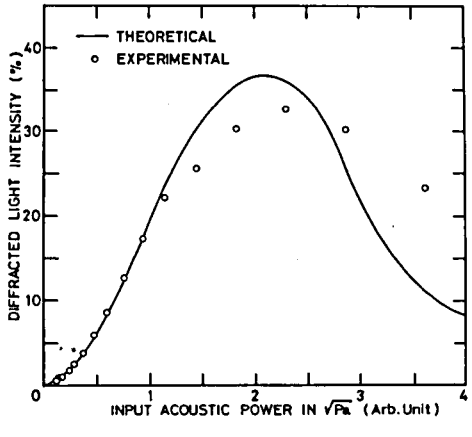

Fig.2.5-6 Relation between the first-order diffracted light intensity and the acoustic power.

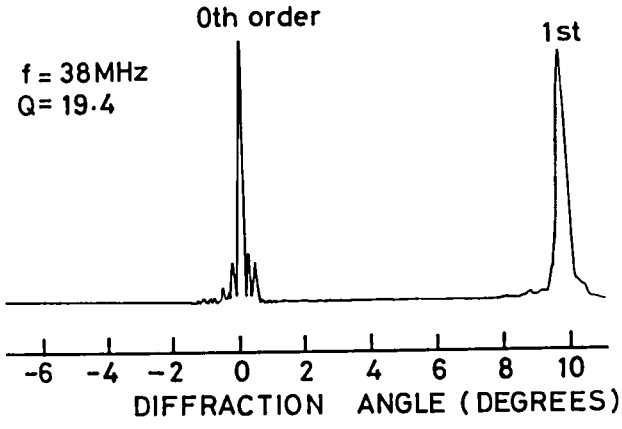

Fig.2.5-7 Angular distribution of the diffracted light intensities. The angles were measured outside the medium.

For operation using the third overtone at 38 MHz, $Q = 19.4 > 4\pi$, and therefore, diffraction occurs in the Bragg region as shown in Fig.2.5-7, where the incident light was transmitted at the Bragg angle (= 5.0° outside the crystal) to the acoustic wave. The experimental determination of the diffraction bandwidth Δf was not attempted since it was not obtainable with our present experimental apparatus. However, assuming that the acoustic power is constant throughout the whole frequency region, or in other words, when the transducer possesses a sufficiently wide bandwidth, the 3-dB-frequency bandwidth Δf due to the Bragg-angle limitation can be calculated from the relation [22]:

$$\Delta f \simeq 1.8\, n\, v^2 \cos\theta_0 / \lambda\, f_0\, L. \qquad (2.5\text{-}1)$$

For a center frequency $f_0 = 38$ MHz, an acoustic velocity $v = 2.29 \times 10^5$ cm/sec, the refractive index $n = 4.7939$, the interaction length $L = 5.06$ mm, and $\cos\theta_0 \simeq \cos\theta_B \simeq 1$, we obtain the value $\Delta f = 22$ MHz. Since the deflection angle θ_d, which is defined as the angle between the undiffracted beam and the first-order diffracted beam, is equal

to twice the Bragg angle θ_B, i.e., $\theta_d = 2\,\theta_B = 2\sin^{-1}(\lambda_0\, f/2\,v)$ (outside the medium), the maximum controllable range of the deflection angle without depletion of the diffraction intensity is obtained as

$$\Delta\theta_d \simeq \lambda_0\, \Delta f/v. \qquad (2.5\text{-}2)$$

For the present deflector with $\Delta f \simeq 22$ MHz, Eq.(2.5-2) gives $\Delta\theta_d \simeq 5.8°$. This means that for the incident angle fixed at $\theta_B = 5.0°$, the deflection angle in the range between 7.2° and 13.0° can be arbitrarily accessed with constant diffraction intensity only by changing the driving acoustic frequency from 27 to 49 MHz. Outside this frequency region, the diffraction intensity rapidly decreases because of the deviation from the Bragg condition.

In an acousto-optic deflection system, there are two most important performance parameters [21,40]: resolution and access time. Resolution, or the maximum number of resolvable angular positions, can be found from the relation [21]:

$$N \simeq D\,\Delta f/v, \qquad (2.5\text{-}3)$$

where D is the width of the incident light beam in the plane of deflection. The access time of the deflector is a measure of the speed of the deflector and is equal to the transit time of the acoustic wave across the optical beam, i.e.,

$$\tau \simeq D/v \qquad (2.5\text{-}4)$$

Equations (2.5-3) and (2.5-4) manifest that there is a conflicting relation between large resolution and short access time. Since we have $\Delta f \simeq N/\tau$ from Eqs.(2.5-3) and (2.5-4), the deflector with large Δf in general possesses a large resolution and short access

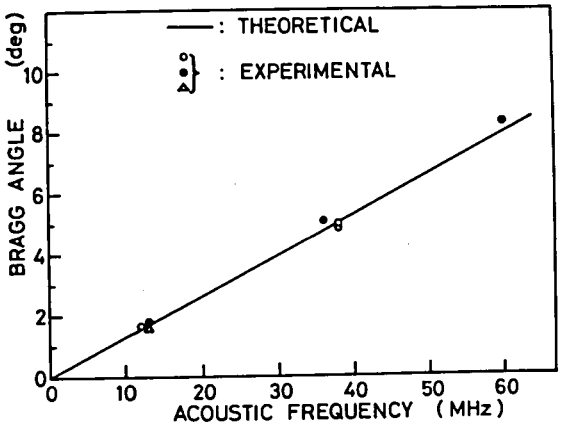

Fig.2.5-8 Relation between the observed Bragg angle and the calculation as a function of acoustic frequency.

time. Besides, as discussed in Sec.2.3, since Δf is approximately proportional to the second figure of merit M', it is necessary to obtain a material with large M' in order to realize an acousto-optic deflector with large Δf. The results given in Table 2.2 show that Te is one of the materials which fulfill this requirement.

When a rectangular incident beam with a width D of 5 mm is used, Eqs.(2.5-3) and (2.5-4) reveal that the deflector shown in Fig.2.5-1 can resolve about 50 spots with an access time of about 2 μsec. The calculation also shows that an acoustic power of 10.5 W is needed to deflect 100 % of the incident 10.6-μm beam.

Figure 2.5-8 shows the relation between the observed and calculated Bragg angles as a function of acoustic frequency.

2.6 Discussion

Besides figures of merit which have been discussed in Sec.2.3, another important property that an acousto-optic material must possess is a low acoustic loss at high frequencies. Figure 2.6-1

shows the frequency dependence of acoustic attenuation for longitudinal waves propagating in the x and in the z direction and a shear wave propagating in the y direction. The latter shear wave is the one shown in Fig.2.2-1 and is simple to experiment with because the displacement direction is parallel to the x axis. The attenuation constants in Fig.2.6-1 are obtained by the pulse-echo method and increase approximately as the square of the frequency [41,42]. Table 2.4 lists the attenuation constants at 100 MHz and Γ. Γ is the

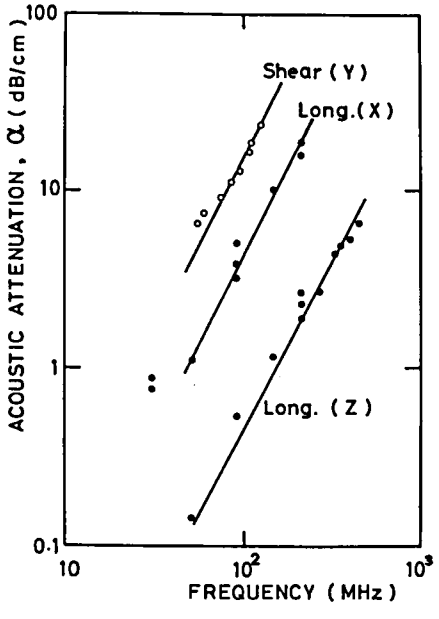

Fig.2.6-1 Acoustic attenuation in Te as a function of acoustic frequency; ○ this work, ● after Reiber [42].

Table 2.4 Acoustic waves in Te.

Polarization and propagation direction	Velocity (10^5 cm/sec)	Mechanical impedance (10^6 kg/sec m^2)	Attenuation at 100 MHz (dB/cm)	Γ (dB/cm GHz^2)
long. in x	2.29	14.3	4.2	420
long. in z	3.40	21.3	0.46	46
shear in y	1.39	8.7	13.0	1300

acoustic attenuation constant at 1 GHz obtained on the assumption that the attenuation is proportional to the square of the frequency. Contrary to previous expectations [13,20,43], these relatively high attenuation constants in Te may restrict the usable frequency to a somewhat lower range except for the case of a longitudinal wave propagating in the z direction. In Fig.2.6-2, the relation between M and Γ is plotted for the five figures of merit in Te and for several other infrared materials of interest which possess relatively well-established acousto-optic data at 10.6 μm [20,21,41,44-46]. It is empirically known that the requirement of low acoustic attenuation and large figure of merit, as a rule, conflict with each other [20,21]. Figure 2.6-2 shows that this tendency holds true also in Te.

There are two contributions that are considered as being most responsible for the acoustic loss mechanism in Te. According to Reiber [42], the major part of the loss at room temperature can be attributed to the phonon-phonon interaction similar to that theoretically treated by Woodruff and Ehrenreich [47], which is often referred to as the Akhieser loss and expressed by

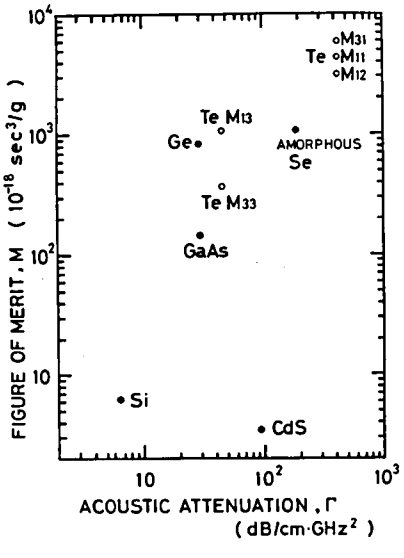

Fig.2.6-2 Relation between figure of merit and acoustic attenuation for various acousto-optic materials measured at 10.6 μm. The open circles denote the values for Te.

$$\alpha = \gamma^2 \omega_A^2 \kappa T / \rho v^5 \qquad (\omega_A \tau \ll 1), \tag{2.6-1}$$

where ω_A is the acoustic frequency, γ is Grüneisen's constant, T is the absolute temperature, κ is the thermal conductivity, and τ is the phonon relaxation time. For the longitudinal wave propagating in the x direction and for the shear wave propagating in the y direction, however, additional loss arises due to the piezoelectric coupling between the acoustic waves and the mobile charge carriers because these two waves are piezoelectrically active [48]. The attenuation for this case was theoretically derived by Fink and Quentin [49] for Te at room temperature, it can be approximated as

$$\alpha = e^3 \omega_A^2 / 2 \rho v^3 \sigma, \tag{2.6-2}$$

where e is the piezoelectric constant, and σ is the electrical conductivity. Equation (2.6-2) shows that the only possible way to lessen the acoustic attenuation is to realize as high a conductivity as possible, for example, by doping with Sb as an impurity since the conductivity is the only controllable physical parameter. This technique will be especially important when using Te at lower temperature since the acoustic loss given by Eq.(2.6-2) increases with decreasing temperature due to the temperature dependence of the conductivity.

In Sec.2.5, we have seen that the maximum number of resolvable spots is determined by Eq.(2.5-3). In some device applications where the speed of deflector is not a major importance, the resolution is also limited by the acoustic attenuation at high frequency. As a tentative limit for the attenuation, $\alpha D = 3.3$ dB is often used as a practically torelable value, where α is the acoustic attenuation in dB per unit length, D is the width of the incident light beam in the plane of deflection, and therefore, αD is the attenuation

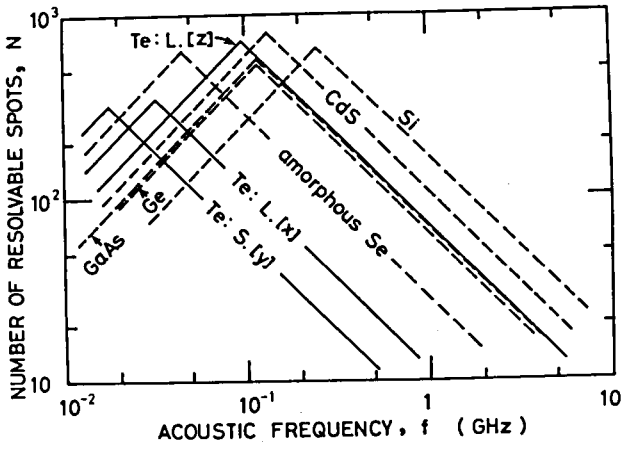

Fig.2.6-3 Relation between number of resolvable spots, N, and acoustic frequency.

that the acoustic wave suffers while it traverses the incident beam [21,40]. Besides, as discussed by Uchida et al [21], if we assume Δf is limited only by the bandwidth of the transducer response, and typically $\Delta f = f_0/2$ (a fractional bandwidth of 50 %), we can modify Eq.(2.5-3) to become

$$N = (1.06 / v \Gamma f_0) \times 10^9 , \qquad (2.6\text{-}3)$$

where f_0 is the center frequency in GHz. Thus, Eq.(2.6-3) determines the resolution in high frequency range, For the resolution at low frequency, if we choose D as 5 cm according to the convention [21]*, We have

$$N = (2.50 f_0 / v) \times 10^9 . \qquad (2.6\text{-}4)$$

* To estimate a potential spatial-resolution of a deflector, D = 5 cm is conventionally used as a standard value for an incident beam-width [21].

The obtainable resolutions determined from Eqs.(2.6-3) and (2.6-4) are plotted in Fig.2.6-3 as a function of acoustic frequency for Te and the other materials which are shown in Fig.2.6-2. The maximum attainable value of N is realized at $f_0 = 0.65/(\Gamma)^{1/2}$ as

$$N_{max} = (1.63 / v \Gamma^{1/2}) \times 10^9 . \qquad (2.6\text{-}5)$$

Though CdS and Si are the materials which possess the largest resolutions, they may be of no practical importance because, as can be understood from Fig.2.6-2, the figures of merit M of these materials are considerably small compared with Te and the rest of the materials. For a longitudinal wave in the z direction in Te, N_{max} is about 700 at $f_0 = 96$ MHz and larger than the values in Ge (N_{max} = 540) and GaAs ($N_{max} = 560$). On the other hand, N_{max} is about 350 at 32 MHz for a longitudinal wave in the x direction in Te.

2.7 Concluding Remarks

In conclusion, in order to avoid the harmuful influence of an optical attenuation due to the absorption band centered at 11 μm, the use of an ordinarily polarized beam is preferred to the use of an extraordinarily polarized one as an incident light. Furthermore, for device applications where only the driving-power consideration is important, appropriate deflector configurations may be those utilizing a longitudinal wave in the x direction and the corresponding large value of M_{12}. On the other hand, the deflector utilizing a longitudinal wave in the z direction and M_{13} has an advantage for the applications which require operations with large resolution, large bandwidth, and short access time.

In addition to its possible use as an infrared acousto-optic medium utilizing normal Bragg diffraction as described thus far

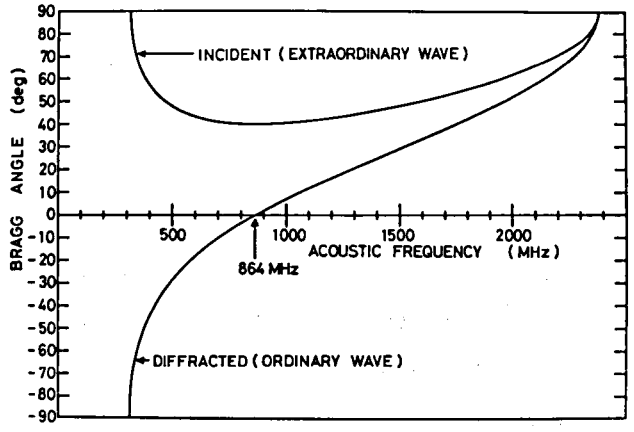

Fig.2.6-4 Calculated anisotropic Bragg angles for longitudinal acoustic waves in the x direction.

in this chapter, the single-ctystal Te also possesses one of the symmetries that allow the use of anisotropic Bragg diffraction. In many anisotropic acousto-optic materials, the use of anisotropic Bragg diffraction has been of interest since it enables one to design wide-bandwidth deflectors. In such deflectors, the center frequency is given by $f_0 = v\,(\,|\,n_o^2 - n_e^2\,|\,)^{1/2} / \lambda_0$ [43]. However, since the birefringence of Te is very large, the required f_0 in general becomes so high that the increase of the acoustic attenuation makes the practical application questionable. The longitudinal wave propagating along the x axis, for instance, can produce the anisotropic Bragg diffraction for the light beam traveling in the z plane due to the photoelastic component p_{41}. Figure 2.6-4 shows the angles of incidence and diffraction for this anisotropic Bragg diffraction which are calculated using Eqs.(3.2-42) and (3.2-43) in Chap.3, from which the center frequency f_0 can be obtained as the frequency at which the angle of diffraction equals zero. The corresponding f_0 is therefore 864 MHz, for which the acoustic attenuation is calculated as high as about 310 dB/cm. On the other hand, anisotropic Bragg diffraction utilizing the strong optical activity

in Te is worth considering since f_0 can be significantly reduced as has been suggested by Warner et al [50] and by Yano et al [51,52] for the case of TeO_2.

References

[1] A. Korpel, *Acousto-Optics*, in *Applied Solid State Science* (Academic, New York, 1972) Vol.3, pp.71-180.

[2] J. F. Nye, *Physical Properties of Crystals* (Clarendon, Oxford, 1957).

[3] A. Feldman, Phys. Rev. 150 (1966) 748.

[4] K. Vedam and E. D. D. Schmidt, Phys. Rev. 146 (1966) 548.

[5] C. W. Higginbotham, M. Cardona, and F. H. Pollak, Phys. Rev. 184 (1969) 821.

[6] W. C. Schneider and K. Vedam, J. Opt. Soc. Am. 60 (1970) 800.

[7] L. Bergman and E. Fues, Nature (London) 24 (1936) 492.

[8] H. Mueller, Z. Kristallogr. 99 (1938) 122.

[9] T. M. Smith and A. Korpel, IEEE J. Quantum Electron. QE-1 (1965) 283.

[10] R. W. Dixon and M. G. Cohen, Appl. Phys. Letters 8 (1966) 205.

[11] J. J. Loforski, Phys. Rev. 93 (1954) 707.

[12] J. C. Thuillier, private communication.

[13] R. W. Dixon and A. N. Chester, Appl. Phys. Letters 9 (1966) 190.

[14] G. W. Farnell, Can. J. Phys. 39 (1961) 65.

[15] J. W. Tucker and V. W. Rampton, *Microwave Ultrasonics in Solid State Physics* (North-Holland, Amsterdam, 1972) p.12.

[16] D. F. Nelson, *Electric, Optic, and Acoustic Interactions in Dielectrics* (Wiley, New York, 1979) p.206.

[17] J. L. Malgrange, G. Quentin, and J. M. Thuillier, Phys. Status Solidi 4 (1964) 139.

[18] R. S. Caldwell and H. Y. Fan, Phys. Rev. 114 (1956) 664.

[19] P. Grosse, *Springer Tracts in Modern Physics* (Springer, Verlag, 1969) Vol.48.

[20] R. W. Dixon, J. Appl. Phys. 38 (1967) 5149.

[21] N. Uchida and N. Niizeki, Proc. IEEE 61 (1973) 1073.

[22] E. I. Gordon, Appl. Opt. 5 (1966) 1629.

[23] K. C. Nomura, Phys. Rev. Letters 5 (1960) 500.

[24] S. Ades and C. H. Champness, J. Opt. Soc. Am. 65 (1975) 217.

[25] S. Fukuda, T. Shiosaki, and A. Kawabata, Phys. Status Solidi (b) 68 (1975) K107.

[26] R. Reijnhart, Ph.D. Thesis, TH Delft (1970).

[27] V. Vysin, Proc. Phys. Soc. 87 (1966) 55.

[28] H. Stolze, M. Lutz, and P. Grosse, Phys. Status Solidi (b) 82 (1977) 457.

[29] K. Natori, Ph.D. Thesis, Tokyo University (1973).

[30] K. Natori, J. Phys. Soc. Jpn. 39 (1975) 1013.

[31] A. Koma, E. Takimoto, and S. Tanaka, Phys. Status Solidi 40 (1970) 239.

[32] J. S. Blakemore, J. W. Schultz, and K. C. Nomura, J. Appl. Phys. 31 (1960) 2226.

[33] J. S. Blakemore and K. C. Nomura, J. Appl. Phys. 32 (1961) 745.

[34] A. Elliott, E. J. Ambrose, and R. Temple, J. Opt. Soc. Am. 38 (1948) 212.

[35] G. K. T. Conn and G. K. Eaton, J. Opt Soc. Am. 44 (1954) 553.

[36] E. M. Bradbury and A. Elliott, J. Sci. Instrum. 39 (1962) 390.

[37] S. Chandrasekhar, Proc. Indian Acad. Sci. A37 (1953) 468.

[38] S. Chandrasekhar, Proc. Roy. Soc. 259 (1961) 531.

[39] W. R. Klein and B. D. Cook, IEEE Trans. Sonics Ultrason. SU-14 (1967) 123.

[40] I. C. Chang, IEEE Trans. Sonics Ultrason. SU-23 (1976) 2.

[41] S. Fukuda, T. Shiosaki, and A. Kawabata, J. Appl. Phys. 50 (1979) 3899.

[42] K. Reiber, Solid State Commun. 6 (1968) 779.

[43] R. W. Dixon, IEEE J. Quantum Electron. QE-3 (1967) 85.

[44] R. L. Abrams and D. A. Pinnow, J. Appl. Phys. 41 (1970) 2765.

[45] H. R. Carleton and R. A. Soref, Appl. Phys. Letters 9 (1966) 110.

[46] S. Fukuda, T. Wada, T. Shiosaki, and A. Kawabata, Jpn. J. Appl. Phys. 16 (1977)659.

[47] T. O. Woodruff and H. Ehrenreich, Phys. Rev. 123 (1967) 1553.

[48] T. Ishiguro and T. Tanaka, Jpn. J. Appl. Phys. 6 (1967) 684.

[49] M. Fink and G. Quentin, Phys. Status Solidi A 4 (1971) 397.

[50] A. W. Warner, D. L. White, and W. A. Bonner, J. Appl. Phys. 43 (1972) 4489.

[51] T. Yano and A. Watanabe, J. Appl. Phys. 45 (1974) 1243.

[52] T. Yano and A. Watanabe, Appl. Opt. 15 (1976) 2250.

[53] N. van Tran, Onde Electr. 47 (1967) 965.

[54] J. H. McFee, G. D. Boyd, and P. H. Schmidt, Appl. Phys. Letters 17 (1970) 57.

[55] G. Arlt and P. Quadflieg, Phys. Status Solidi 32 (1969) 687.

CHAPTER 3

PHOTOELASTICITY AND ACOUSTO-OPTIC DIFFRACTION INFLUENCED BY SIMULTANEOUS PRESENCE OF PIEZOELECTRICITY AND CONDUCTIVITY IN PIEZOELECTRIC SEMICONDUCTOR Te

3.1 Introduction

As has been seen in Chap.2, an elastic deformation accompanying an acoustic mode traveling in a medium gives rise to optical scattering phenomena, known as Brillouin scattering or acousto-optic diffraction. The physical mechanism of these scattering phenomena in an anisotropic crystal can best be described in terms of the time-space fluctuations in the inverse dielectric constant of the crystal. Especially, as discussed by Keller [1-3], in strong piezoelectric semiconductors three effects can contribute significantly to these fluctuations:

$$\Delta(1/\kappa)^{t}_{ij} = \Delta(1/\kappa)^{d}_{ij} + \Delta(1/\kappa)^{in}_{ij} + \Delta(1/\kappa)^{fc}_{ij} \ , \qquad (3.1\text{-}1)$$

where $\Delta(1/\kappa)_{ij}$ is the change in the inverse dielectric constant at an optical frequency caused by the elastic deformation. (Hereinafter, a dielectric constant at an optic1 frequency will be designated by κ_{ij} and we shall retain ε_{ij} to mean that at an acoustic frequency.) The first term, $\Delta(1/\kappa)^{d}_{ij}$, represents the direct photoelastic effect arising from the fluctuations in the strain (or, equivalently, the Pockels photoelasticity) and the mean rotation of the volume element. The formulation of the direct effect was derived by Nelson and Lax [4-6] on the phenomenological basis as

$$\Delta(1/\kappa)^{d}_{ij} = p_{(ij)(kl)}\, S_{(kl)} + p_{(ij)[kl]}\, R_{[kl]}$$

$$= p_{(ij)kl}\, u_{k,l} \,, \qquad (3.1\text{-}2)$$

where the summation convention has been used. $p_{(ij)(kl)}$ in the first term is the Pockels photoelastic tensor component and $p_{(ij)[kl]}$ in the second term represents the photoelastic tensor due to the rotational contribution. The infinitesimal strain and mean rotation are defined, respectively, by

$$S_{(kl)} \equiv \frac{1}{2}\left(u_{k,l} + u_{l,k} \right) \qquad (3.1\text{-}3)$$

and

$$R_{[kl]} \equiv \frac{1}{2}\left(u_{k,l} - u_{l,k} \right) . \qquad (3.1\text{-}4)$$

Parentheses enclosing subscripts indicate symmetry upon interchange of the subscripts, while bracketed subscripts indicate antisymmetry upon interchange. The gradient of the displacement vector u_k of the acoustic wave is denoted by $u_{k,l} \equiv \partial u_k / \partial x_l$. The antisymmetric part $p_{(ij)[kl]}$ of the total photoelastic tensor can be calculated simply from the optical dielectric tensor [4-6]:

$$p_{(ij)[kl]} = \frac{1}{2}\left[(1/\kappa)_{il}\, \delta_{kj} + (1/\kappa)_{lj}\, \delta_{ik} \right.$$

$$\left. -(1/\kappa)_{ik}\, \delta_{lj} - (1/\kappa)_{kj}\, \delta_{il} \right] . \qquad (3.1\text{-}5)$$

The second term on the right-hand side of Eq.(3.1-1), $\Delta(1/\kappa)^{in}_{ij}$, represents the indirect photoelastic effect, i.e., the succession of the piezoelectric and electro-optic effects. This effect includes the screening caused by the free carriers and can be calculated from the

acousto-electrically induced self-consistent electric field due to the piezoelectric coupling. The third term, $\Delta(1/\kappa)_{ij}^{fc}$, gives the change of the inverse dielectric constant caused by the fluctuation in the free-carrier densities, i.e., an acoustic wave may be accompanied by free-carrier density waves arising also from the piezoelectric coupling. Accordingly, the second and third terms are significant only when the acoustic wave is piezoelectrically active, or equivalently when the acoustic wave induces a longitudinal self-consistent electric field. Contributions from the deformation-potential coupling may be ignored, since in strong piezoelectric semiconductors contributions from the piezoelectric coupling dominate these by many orders of magnitude. Appearance of the third term was first theoretically predicted by Proklov, Shkerdin, and Gulyaev [7] and experimentally verified by Proklov, Mirgorodsky, Shkerdin, and Gulyaev[8] in an n-type CdS crystal.

Because both the second and third terms in Eq.(3.1-1) are tensor function of the elastic deformation (the appropriate independent elastic variable in this case is the strain), it is possible to define effective photoelastic constants for these two terms. An explicit expression for the photoelastic constant for the indirect effect was derived by Nelson and Lax [5,6] for the case without free-carrier screening and by Sasaki, Tsubouchi, Chubachi, and Mikoshiba [9] for the case with screening. The latter authors started from the Hutson and White formulation [10,11] for the acousto-electric interaction assuming the existence of only one kind of free carrier and therefore it applies only to extrinsic semiconductors. On the other hand, Keller [2] gave rather general expressions for the dielectric fluctuations of the second and third terms in Eq. (3.1-1), but assumed also only one kind of free carrier.

In contrast to the previous works above, the theory which will be developed here takes account of the existence of both electrons and holes and derives the expressions for effective photoelasticity

that are applicable to piezoelectric semiconductors in either intrinsic or extrinsic conduction regime. The theoretical treatment presented in Sec.3.2.A is based upon the linear acousto-electric theory originally developed by Fink and Quentin [12] taking two kinds of free carriers into account. The treatment is therefore valid for the cases where the small-signal theory applies. The derived results predict that in intrinsic semiconductors considerable cancellation may occur between photoelasticity due to electron-density fluctuation and that due to hole-density fluctuation. In Sec.3.2.B, we shall apply the results to Te which is known as one of the most highly piezoelectric semiconductors. Finally, in Sec.3.3, acousto-optic diffraction experiments of 10.6-μm infrared light from a CO_2 laser are carried out using a Te crystal in intrinsic conduction regime at room temperature. In accordance with the theoretical prediction, an appreciable diffraction ascribable to the free-carrier density fluctuations is observed [15].

In this chapter, the notation for refractive index has been changed from " n " to " N " and an electron density will be designated by " n ".

3.2 Theoretical

3.2.A *Photoelasticity in piezoelectric semiconductors*

In this section, we derive the expressions for the effective photoelastic constants corresponding to the second and third terms in Eq.(3.1-1). In the following treatment, the recombination between electrons and holes will be neglected. This assumption is legitimate in Te, where $\tau_{rec} \sim 10^{-6}$ sec [12], which is much longer than the period of the acoustic wave we shall be concerned with. In order to derive the effective photoelastic tensors with full symmetry, the tensor notations will be retained throughout.

The basic equations to describe the acousto-electric interaction are the mechanical wave equations, the Maxwell equations, and the piezoelectric equations of state [12]:

$$T_{pq} = c_{pqkl}\, S_{kl} - e_{spq}\, E_s \tag{3.2-1}$$

$$D_i = e_{imn}\, S_{mn} + \varepsilon_0\, \varepsilon_{ki}\, E_k \tag{3.2-2}$$

where T_{pq} is the stress, S_{kl} is the strain, c_{pqkl} is the elastic stiffness constant, e_{imn} is the piezoelectric constant, and ε_{ki} is the dielectric constant at an acoustic frequency. The subscripts are referred to the usual rectangular crystallographic coordinates. An acoustic wave propagating in the medium creates an instantaneous local modulation of the free-carrier densities: neglecting trapping effect,

$$n' = n_0 + n, \tag{3.2-3}$$

$$p' = p_0 + p, \tag{3.2-4}$$

where n_0 and p_0 are the equilibrium density of electrons and holes in the absence of an acoustic wave, and n and p represent their instantaneous local changes. Poisson's equation is satisfied separately for the two kinds of free carriers:

$$\frac{\partial D_i^n}{\partial x_i} = -q\,n\,, \qquad \frac{\partial D_i^p}{\partial x_i} = q\,p\,, \tag{3.2-5}$$

and

$$D_i = D_i^n + D_i^p\,, \tag{3.2-6}$$

where the superscripts n and p denote the component due to elec-

trons and due to holes, respectively, and q is the electronic charge. The equations of charge continuity are

$$\frac{\partial J_j^n}{\partial x_j} = q \frac{\partial n}{\partial t}, \qquad \frac{\partial J_j^p}{\partial x_j} = - q \frac{\partial p}{\partial t}. \tag{3.2-7}$$

The total current density is

$$J_j = J_j^n + J_j^p \tag{3.2-8}$$

with

$$J_j^n = \sigma_{kj}^n E_k + q D_{ij}^n \frac{\partial n}{\partial x_i} \tag{3.2-9}$$

and

$$J_j^p = \sigma_{kj}^p E_k - q D_{ij}^p \frac{\partial p}{\partial x_i}, \tag{3.2-10}$$

where D_{ij}^n and D_{ij}^p are the diffusion constants, the equilibrium electrical conductivities are

$$\sigma_{kj}^n = q n_0 \mu_{kj}^n, \qquad \sigma_{kj}^p = q p_0 \mu_{kj}^p, \tag{3.2-11}$$

and the nonlinear terms containing $n E_k$ and $p E_k$ have been dropped as compared with the other terms. Equations (3.2-1) through (3.2-10) can be solved by introducing plane-wave time and space dependences such as

$$E_k = E_k^0 \exp[j(k_i^a x_i - \omega t)] \tag{3.2-12}$$

and

$$n = n^0 \exp[j(k_i^a x_i - \omega t)], \tag{3.2-13}$$

where k_i^a and ω are the wave vector and the angular frequency of the acoustic wave. The piezoelectrically induced self-consistent longitudinal electric field is then obtained as

$$E_r = -\frac{a_r\, a_l\, e_{lmn}\, S_{mn}}{\varepsilon_0\, a_k\, \varepsilon_{kp}\, a_p} \frac{1}{1+\dfrac{j(\omega_C^n/\omega)}{1+j(\omega/\omega_D^n)}+\dfrac{j(\omega_C^p/\omega)}{1+j(\omega/\omega_D^p)}}, \qquad (3.2\text{-}14)$$

where the dielectric relaxation frequencies are

$$\omega_C^n = \frac{a_i\, \sigma_{ij}^n\, a_j}{\varepsilon_0\, a_k\, \varepsilon_{kl}\, a_l}, \qquad \omega_C^p = \frac{a_i\, \sigma_{ij}^p\, a_j}{\varepsilon_0\, a_k\, \varepsilon_{kl}\, a_l}, \qquad (3.2\text{-}15)$$

and diffusion frequencies are

$$\omega_D^n = v^2 / a_i\, D_{ij}^n\, a_j = q\, v^2 / a_i\, \mu_{ij}^n\, a_j\, k_B\, T, \qquad (3.2\text{-}16)$$

$$\omega_D^p = v^2 / a_i\, D_{ij}^p\, a_j = q\, v^2 / a_j\, \mu_{ij}^p\, a_i\, k_B\, T. \qquad (3.2\text{-}17)$$

v is the acoustic velocity, a_i is the component of the directional cosine of the acoustic wave vector, and k_B is the Boltzmann constant. The local fluctuations in the free-carrier densities due to acousto-electric bunching are then

$$n = \frac{a_l\, e_{lmn}\, S_{mn}}{q\, v} \frac{\omega_C^n}{[1+j(\omega/\omega_D^n)]\left[1+\dfrac{j(\omega_C^n/\omega)}{1+j(\omega/\omega_D^n)}+\dfrac{j(\omega_C^p/\omega)}{1+j(\omega/\omega_D^p)}\right]}, \qquad (3.2\text{-}18)$$

and

$$p = -\frac{a_1\, e_{1mn}\, S_{mn}}{q\, v} \frac{\omega_C^p}{[1+j(\omega/\omega_D^p)]\left[1+\dfrac{j(\omega_C^n/\omega)}{1+j(\omega/\omega_D^n)}+\dfrac{j(\omega_C^p/\omega)}{1+j(\omega/\omega_D^p)}\right]} . \tag{3.2-19}$$

From Eq.(3.2-14), the change of the inverse dielectric constant arising from the indirect effect, i.e., the second term on the right-hand side of Eq.(3.1-1) can be written

$$\begin{aligned}\Delta(1/\kappa)_{ij}^{in} &= \gamma_{ijr}\, E_r \\ &= -\frac{\gamma_{ijr}\, a_r\, a_1\, e_{1mn}\, S_{mn}\, A}{\varepsilon_0\, a_k\, \varepsilon_{kp}\, a_p} \\ &\equiv p_{ijmn}^{in}\, S_{mn} ,\end{aligned} \tag{3.2-20}$$

with

$$A = \frac{1}{1+\dfrac{j(\omega_C^n/\omega)}{1+j(\omega/\omega_D^n)}+\dfrac{j(\omega_C^p/\omega)}{1+j(\omega/\omega_D^p)}} , \tag{3.2-21}$$

where γ_{ijr} is the electro-optic constant measured at constant strain. The effective photoelastic constant defined in Eq.(3.2-20) is then given by

$$p_{ijmn}^{in} = -\frac{\gamma_{ijr}\, a_r\, a_1\, e_{1mn}\, A}{\varepsilon_0\, a_k\, \varepsilon_{kp}\, a_p} . \tag{3.2-22}$$

The third term on the right-hand side of Eq.(3.1-1) can be obtained through the relation for infrared radiation [13,14]:

$$\kappa_{ij} = \kappa_{ij}^0 - \frac{q^2 n'}{\varepsilon_0\, \omega_o^2}\left(\frac{1}{m_n}\right)_{ij} - \frac{q^2 p'}{\varepsilon_0\, \omega_o^2}\left(\frac{1}{m_p}\right)_{ij} , \tag{3.2-23}$$

where n' and p' have been defined in Eqs.(3.2-3) and (3.2-4), κ_{ij}^0 is

the dielectric constant in the absence of free carriers, ω_o is the optical frequency, and m_n and m_p are the electron and the hole effective mass, respectively. Differentiating Eq.(3.2-23) with respect to n' and p', we obtain

$$\Delta\kappa_{ij}^{fc} \equiv \Delta\kappa_{ij}^{n} + \Delta\kappa_{ij}^{p}$$

$$= - \kappa_{ij}^{n} \, (n/n_0) - \kappa_{ij}^{p} \, (p/p_0) \, , \qquad (3.2\text{-}24)$$

where

$$\kappa_{ij}^{n} = \frac{q^2 n_0}{\varepsilon_0 \, \omega_o^{\,2}} \left(\frac{1}{m_n} \right)_{ij} , \quad \kappa_{ij}^{p} = \frac{q^2 p_0}{\varepsilon_0 \, \omega_o^{\,2}} \left(\frac{1}{m_p} \right)_{ij} , \qquad (3.2\text{-}25)$$

and n and p have been derived in Eqs.(3.2-18) and (3.2-19). To obtain the change in the inverse dielectric constant, we shall employ the following identity equation.

$$\Delta(1/\kappa)_{ij} = - \, (1/\kappa)_{im} \, \Delta\kappa_{mn} \, (1/\kappa)_{nj} \, . \qquad (3.2\text{-}26)$$

In the crystal symmetries except for triclinic and monoclinic systems, the coordinate system we have referred to above agrees with the dielectric principal axes, so that Eq.(3.2-26) is reduced to the simple form,

$$\Delta(1/\kappa)_{ij} = - \frac{\Delta\kappa_{ij}}{\kappa_{ii} \, \kappa_{jj}} \, , \qquad (3.2\text{-}27)$$

where no summation over repeated subscripts is implied. Substitution of Eq.(3.2-24) into Eq.(3.2-27) yields

$$\Delta(1/\kappa)_{ij}^{fc} = \frac{\kappa_{ij}^{n}}{\kappa_{ii} \, \kappa_{jj}} \left(\frac{n}{n_0} \right) \delta_{ij} + \frac{\kappa_{ij}^{p}}{\kappa_{ii} \, \kappa_{jj}} \left(\frac{p}{p_0} \right) \delta_{ij}$$

$$\equiv p_{ijmn}^{fc} \, S_{mn} \, . \qquad (3.2\text{-}28)$$

The effective photoelastic constant is then written

$$p_{ijmn}^{fc} \equiv p_{ijmn}^{n} + p_{ijmn}^{p}$$
$$= \frac{a_1 \, e_{lmn} \, A}{\kappa_{ii} \, \kappa_{jj} \, q \, v} \left(\frac{\kappa_{ij}^{n}}{n_0} \frac{\omega_C^{n}}{1 + j(\omega/\omega_D^{n})} - \frac{\kappa_{ij}^{p}}{p_0} \frac{\omega_C^{p}}{1 + j(\omega/\omega_D^{p})} \right) \delta_{ij} \, , \tag{3.2-29}$$

Because the right-hand side of Eq.(3.2-29) contains κ_{ij}^{n} and κ_{ij}^{p} which are inversely proportional to the square of the optical frequency ω_o^2 , the photoelasticity arising from the free-carrier density fluctuations in some favorable cases may become comparable to or even larger than the two other contributions for the measurements using long enough optical wavelength (10.6-μm light of a CO_2 laser, for example).

For piezoelectric semiconductors in extrinsic conduction regime, p-type for example, putting the equilibrium electron density n_0 equal to zero as compared with p_0, Eqs.(3.2-22) and (3.2-29) become

$$p_{ijmn}^{in} = - \frac{\gamma_{ijr} \, a_r \, a_1 \, e_{lmn}}{\varepsilon_0 \, a_k \, \varepsilon_{kp} \, a_p} \frac{1 + j(\omega/\omega_D^{p})}{1 + j(\omega_C^{p}/\omega + \omega/\omega_D^{p})} \tag{3.2-30}$$

and

$$p_{ijmn}^{fc} = - \frac{a_1 \, e_{lmn} \, \kappa_{ij}^{p} \, \delta_{ij}}{\kappa_{ii} \, \kappa_{jj} \, q \, v \, p_0} \frac{\omega_C^{p}}{1 + j(\omega_C^{p}/\omega + \omega/\omega_D^{p})} \, . \tag{3.2-31}$$

Equation (3.2-30) reduces to the expression derived by Sasaki et al [9]. Equations (3.2-29) and (3.2-31) indicate that the conductivity dependence of p_{ijmn}^{fc} is considerably different between intrinsic and extrinsic semiconductors. In particular, for intrinsic case where the relation $n_0 = p_0$ holds between the two equilibrium carrier densities, p_{ijmn}^{n} and p_{ijmn}^{p} defined in Eq.(3.2-29) have the absolute values which are in general not very much different from each other, while

the phase angle between them is always greater than $\pi/2$ and less than π. Especially, when $\omega_D^n \sim \omega_D^p$, the phase angle cannot deviate much from π regardless of ω. The maximum deviation of the phase angle from π occurs at the acoustic frequency of $\omega = (\omega_D^n\ \omega_D^p)^{1/2}$. As a striking result, considerable cancellarion is expected between the photoelasticity due to the electron-density fluctuation and that due to the hole-density fluctuation. This behavior, as suggested by Eqs Eqs.(3.2-18) and (3.2-19), reflects that the electron and hole bunchings always occur nearly π out of phase provided that $\omega_D^n \sim \omega_D^p$. If $\omega_D^n = \omega_D^p$, the phase angle between p_{ijmn}^n and p_{ijmn}^p is exactly π so that the most effective cancellation takes place.

It is understood from Eqs.(3.1-2), (3.1-5), (3.2-22), and (3.2-29) that the photoelastic tensors corresponding to the different physical origins possess different summetries and show different dependences on the acoustic and optical frequencies. This permits a powerful experimental technique to measure each contribution separately. For acoustic frequencies $\omega \ll \omega_C^{n,p}$, $\omega_D^{n,p}$, Eqs.(3.2-22) and (3.2-29) can be approximated as

$$p_{ijmn}^{in} = j \frac{\gamma_{ijr}\ a_r\ a_l\ e_{lmn}}{\varepsilon_0\ a_k\ \varepsilon_{kp}\ a_p} \frac{\omega}{\omega_C^n + \omega_C^p} \tag{3.2-32}$$

and

$$p_{ijmn}^{fc} = -j \frac{a_l\ e_{lmn}}{\kappa_{ii}\ \kappa_{jj}\ q\ v} \frac{\omega}{\omega_C^n + \omega_C^p} \left(\frac{\kappa_{ij}^n\ \omega_C^n}{n_0} - \frac{\kappa_{ij}^p\ \omega_C^p}{p_0} \right) \delta_{ij}, \tag{3.2-33}$$

indicating that the absolute values of both the photoelastic constants increase in proportion to ω. For sufficiently high frequencies $\omega \gg \omega_C^{n,p}$, $\omega_D^{n,p}$, on the other hand, the free-carrier screening rapidly diminishes and p_{ijmn}^{in} approaches its high-frequency limit,

$$p^{in}_{ijmn} = - \frac{\gamma_{ijr}\, a_r\, a_l\, e_{lmn}}{\varepsilon_0\, a_k\, \varepsilon_{kp}\, a_p}\,, \tag{3.2-34}$$

which is in agreement with the expression obtained by Nelson and Lax [5,6] in the limit of zero conductivity. On the other hand, $|p^{fc}_{ijmn}|$ decreases in inverse proportion to ω as

$$p^{fc}_{ijmn} = - j \frac{a_l\, e_{lmn}}{\kappa_{ii}\, \kappa_{jj}\, q\, v} \frac{1}{\omega} \left(\frac{\kappa^n_{ij}\, \omega^n_C\, \omega^n_D}{n_0} - \frac{\kappa^p_{ij}\, \omega^p_C\, \omega^p_D}{p_0} \right) \delta_{ij}\,. \tag{3.2-35}$$

These frequency dependences will be considered in more detail in Sec. 3.2.B by taking Te as an example.

3.2.B *Photoelasticity and acousto-optic Bragg diffraction in Te*

As described in Sec.2.1, Te is a semiconducting material with a trigonal crystal structure belonging to class-32 symmetry and shows p-type extrinsic conduction below its Hall-reversal temperature of about 200°K. Since Te is one of the most highly piezoelectric materials, it shows remarkable nonlinear conduction due to the acousto-electric effect at low temperature [16-20]. Ultrasonic amplification in this material was achieved for the first time by Ishiguro et al [16,21] using a shear ultrasonic wave of 45 MHz propagating along the y axis at 77°K. These previous experimental results suggest that appreciable dielectric modulation due to the piezoelectric coupling should be observed when peizoelectrically active ultrasonic waves traverse the material.

The contracted matrix notation for the symmetric part $p_{(ij)(kl)}$ of the photoelastic tensor for the direct effect in crystals with the class 32 symmetry has been already given by Eq.(2.1-1) in Sec. 2.1. However, we shall give it here again for convenience sake [22]:

$$\begin{vmatrix} p_{11}^{s} & p_{12} & p_{13} & p_{14} & 0 & 0 \\ p_{12} & p_{11} & p_{13} & -p_{14} & 0 & 0 \\ p_{31} & p_{31} & p_{33} & 0 & 0 & 0 \\ p_{41} & -p_{41} & 0 & p_{44} & 0 & 0 \\ 0 & 0 & 0 & 0 & p_{44} & p_{41} \\ 0 & 0 & 0 & 0 & p_{14} & \frac{1}{2}(p_{11}-p_{12}) \end{vmatrix}, \qquad (3.2\text{-}36)$$

(8 independent components)

where the superscript "s" is attatched to clarify its symmetric property. Equation (3.1-5) gives the antisymmetric part $p_{(ij)[kl]}$ as

$$p_{(13)[13]} = p_{(23)[23]} = \frac{1}{2}\left(\frac{1}{N_e^2} - \frac{1}{N_o^2}\right), \qquad (3.2\text{-}37)$$

where N_o and N_e are the ordinary and the extraordinary index, respectively. The other antisymmetric components are identically zero in this crystal class. For Te, $N_o = 4.7939$ and $N_e = 6.2433$ at 10.6 μm [23]. Then the value of Eq.(3.2-37) reduces to - 0.0089.

The photoelastic tensor p_{ijmn}^{in} for the indirect effect is determined from Eq.(3.2-22) using the dielectric-constant and piezoelectric-constant tensors of the class 32 as

$$\begin{vmatrix} p_{11}^{in} & -p_{11} & 0 & p_{14} & p_{15} & p_{16} \\ -p_{11} & p_{11} & 0 & -p_{14} & -p_{15} & -p_{16} \\ 0 & 0 & 0 & 0 & 0 & 0 \\ p_{41} & -p_{41} & 0 & p_{44} & p_{45} & p_{46} \\ p_{46} & -p_{46} & 0 & p_{45} & p_{55} & p_{56} \\ p_{16} & -p_{16} & 0 & p_{15} & p_{65} & p_{66} \end{vmatrix}. \qquad (3.2\text{-}38)$$

(12 independent components)

In a similar way, Eq.(3.2-29) determines p^{fc}_{ijmn} as

$$\begin{vmatrix} p^{fc}_{11} & -p_{11} & 0 & p_{14} & p_{15} & p_{16} \\ p_{11} & -p_{11} & 0 & p_{14} & p_{15} & p_{16} \\ p_{31} & -p_{31} & 0 & p_{34} & p_{35} & p_{36} \\ 0 & 0 & 0 & 0 & 0 & 0 \\ 0 & 0 & 0 & 0 & 0 & 0 \\ 0 & 0 & 0 & 0 & 0 & 0 \end{vmatrix} . \qquad (3.2\text{-}39)$$

(8 independent components)

Because of the presence of the acoustic wave-vector direction a_1 in p^{in}_{ijmn} as shown by Eq.(3.2-22), it does not transform as a simple fourth-rank tensor. It is instead a tensor function of the acoustic wave-vector direction. The same situation holds also in p^{fc}_{ijmn} which has been derived thus far in this study.

Since p^{fc}_{ijmn} is equal to zero if $i \neq j$, it is understood that the acousto-optic diffraction of an incident light caused by the free-carrier density fluctuations does not accompany a right-angle rotation of the polarization plane. In the Bragg-diffraction limit [24], therefore, when the polarization vector of the incident light lies in the plane perpendicular to the optic axis in an optically uniaxial crystal, like Te, the diffraction will take the form of isotropic Bragg diffraction [26] (see Appendix). On the other hand, anisotropic Bragg diffraction takes place when the polarization plane rotates at a right angle to that of the incident light (i.e., $i \neq j$) and also refractive indices for both lights differ from each other [26].

Starting from Eq.(13.5.52) in Ref.(6), an expression for the diffracted optical intensity from the Bragg diffraction can be de-

rived under the phase matching condition for plane waves. Ignoring the incident optical wave depletion due to the diffraction, we obtain

$$I_D = I_I \frac{\pi^2}{2\lambda_0^2} \left(\frac{N_I^3(\theta_I)\, N_D^3(\theta_D)\, p_{eff}^2}{\rho\, v^3} \right) \frac{P_A}{L\, H} \frac{L^2}{\cos^2\theta_D} , \quad (3.2\text{-}40)$$

where the subscripts I and D indicate the quantities relating to the incident and the diffracted light, respectively, N is the refractive index, P_A is the acoustic power, L and H are respectively the width and the height of the cross section of the acoustic column where the direction of L lies in the scattering plane and is normal to the acoustic wave vector, ρ is the density, v is the acoustic velocity, λ_0 is the wavelength of the diffracted light in vacuum, θ is the angle between the optical wave vector and the normal to the acoustic wave vector, and p_{eff} is the effective photoelastic constant [27] given by

$$p_{eff} = \left| d_m^D\, p_{mnkl}\, d_n^I\, a_l\, b_k \right| , \quad (3.2\text{-}41)$$

where d_m^D and d_n^I are unit vectors in the directions of the electric displacements of the diffracted and incident waves. a_l and b_k are unit vectors in the direction of the acoustic wave vector and of the material displacement, respectively. p_{mnkl} is a relevant photoelastic tensor component given by Eqs.(3.2-22), (3.2-29), and (3.2-36) -(3.2-39). In the derivation of Eq.(3.2-40), we have made the approximation that $\cos\delta_D \simeq 1$ and $\cos\delta_I \simeq 1$, where $\delta_{D,I}$ are the angles between the optical Poynting vector and the wave vector. Equation (3.2-40) is essentially the same as those usually referred to in experimental determinations of acousto-optic figures of merit (Eq. (A-34) of Appendix, for example) except that the latter expressions often contain some ambiguous notations for refractive indices and phototelastic constant.

In order to utilize Eqs.(3.2-40) and (3.2-41), it is necessary to determine the frequency dependence of the angle of incidence θ_I and the corresponding angle of the diffraction θ_D under the phase matching condition (or equivalently, the Bragg condition), which can be derived simply from consideration of energy and pseudomomentum conservation as the following well-known equations [25].

$$\sin\theta_I = \frac{\lambda_0}{2\, N_I(\theta_I)\, v}\left(f + \frac{v^2}{f\,\lambda_0{}^2}\left[\, N_I{}^2(\theta_I) - N_D{}^2(\theta_D)\,\right]\right) \qquad (3.2\text{-}42)$$

and

$$\sin\theta_D = \frac{\lambda_0}{2\, N_D(\theta_D)\, v}\left(f - \frac{v^2}{f\,\lambda_0{}^2}\left[\, N_I{}^2(\theta_I) - N_D{}^2(\theta_D)\,\right]\right), \qquad (3.2\text{-}43)$$

where $f\ (=\omega/2\pi)$ is the acoustic frequency.

In the acousto-optic diffraction experiments we shall describe below, a shear ultrasonic wave propagating along the crystallographic y axis with the velocity of 1390 m/sec at room temperature was used as one of the highly piezoelectrically active acoustic waves in Te. This wave has its displacement vector parallel to the x axis, so that the mean rotation of the volume element defined by Eq.(3.1-4) above is reduced to $R_{[12]}$. Because Eq.(3.2-37) reveals that there are no non-zero antisymmetric photoelastic components corresponding to $R_{[12]}$, we can neglect the rotational contribution and consequently the only relevant variable we must retain to describe the elastic deformation is the strain S_{12}. The experimental geometry is shown in Fig.3.2-1, in which the angles measured outside the medium are determined by Snell's law as

$$\theta_I' = \sin^{-1}\left[\, N_I(\theta_I)\sin\theta_I\,\right] \qquad (3.2\text{-}44)$$

and

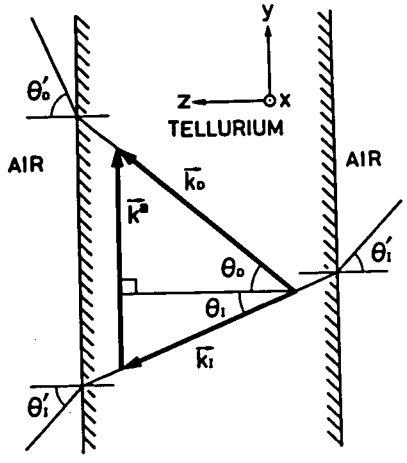

Fig.3.2-1 Schematic illustration of the wave vector diagram employed in the acousto-optic diffraction experiments. $\vec{k}_I$ and $\vec{k}_D$ are the wave vectors of the incident and diffracted lights, respectively. θ_I and θ_D are the angles of incidence and diffraction measured inside the crystal, while θ_I' and θ_D' are those measured outside the crystal. $\vec{k}^a$ is the wave vector of the shear acoustic wave propagating along the y axis. The coordinate axes denote the crystallographic orientation for the Te sample. The diffraction plane is parallel to the y-z plane.

$$\theta_D' = \sin^{-1}[\, N_D(\theta_D) \sin\theta_D \,] . \qquad (3.2\text{-}45)$$

The incident optical beam was transmitted in the y-z plane and ordinarily polarized parallel to the x axis. Therefore, in an isotropic Bragg case the polarization of the diffracted light is also parallel to the x axis and both $N_I(\theta_I)$ and $N_D(\theta_D)$ coincide with the ordinary index given by N_o, being independent of θ_I and θ_D. Equations (3.2-42) and (3.2-43) are then reduced to

$$\sin\theta_I = \sin\theta_D = \lambda_0 \, f \,/\, 2\, N_o \, v . \qquad (3.2\text{-}46)$$

For anisotropic Bragg diffraction, on the other hand, the polarization vector of the diffracted light lies in the y-z plane and Eqs. (3.2-42) and (3.2-43) are simply modified by putting $N_I(\theta_I) = N_o$ and

$N_D(\theta_D) = 1/[(\cos\theta_D/N_o)^2 + (\sin\theta_D/N_e)^2]^{1/2}$. Figure 3.2-2 shows the thus calculated external angles θ_I' and θ_D' for both isotropic and anisotropic Bragg diffractions as a function of acoustic frequency. Here two kinds of solutions designated in the diagram respectively by "case 1" and "case 2" have been obtained for the anisotropic diffraction, for which the experiments were carried out with respect to the case 1.

Inspection of Eqs.(3.2-36) and (3.2-41) reveals that in this geometry the direct photoelastic effect gives rise to anisotropic Bragg diffraction through the effective photoelastic constant

$$p_{eff}^s = |p_{41}^s \sin\theta_D - p_{66}^s \cos\theta_D|. \qquad (3.2\text{-}47)$$

Numerical values for five of the eight independent photoelastic tensor components in Te have been already experimentaly determined in

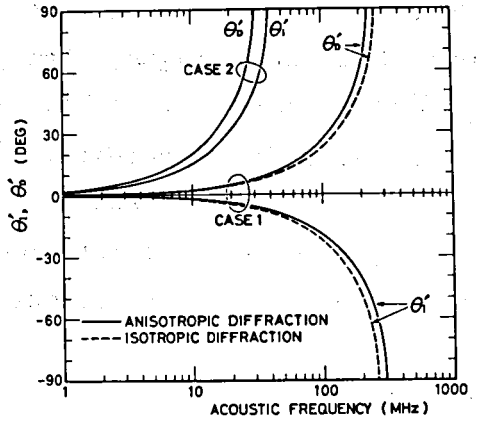

Fig.3.2-2 Calculated angles of incidence and diffraction outside the Te crystal at 10.6 μm as a function of frequency of a shear acoustic wave propagating in the y direction with displacement parallel to the x axis. The incident light is an ordinary wave polarized along the x axis and the diffraction plane lies in the y-z plane. The solid curves are obtained for anisotropic Bragg diffraction, while the broken curves are for isotropic Bragg diffraction. There are two kinds of solutions denoted respectively by "case 1" and "case 2" for the anisotropic diffraction.

Table 3.1 Pockels photoelastic constants in Te.

$\lvert p_{11}^s \rvert$	$\lvert p_{12}^s \rvert$	$\lvert p_{13}^s \rvert$	$\lvert p_{31}^s \rvert$	$\lvert p_{33}^s \rvert$	$\lvert p_{14}^s \rvert$	$\lvert p_{41}^s \rvert$	$\lvert p_{44}^s \rvert$
0.164	0.138	0.146	0.086	0.038	-	-	-

Sec.2.3 as shown in Table 2.3 [28,29]. These values are here again listed in Table 3.1 for convenience sake, where values for p_{14}^s, p_{41}^s, and p_{44}^s have not been determined yet. Though the actual value for p_{41}^s is still unknown, the first term in Eq.(3.2-47) may be dropped compared to the second term which is a good approximation as long as we are concerned with a small Bragg angle so as to satisfy the relation $\sin\theta_D \ll 1$. Then we have $p_{eff}^s \simeq |p_{66}^s|$. The absolute value for p_{66}^s can be determined from the relation [22] $|p_{66}^s| = |p_{11}^s - p_{12}^s|/2$, with $|p_{11}^s| = 0.164$ and $|p_{12}^s| = 0.138$. Because the relative sign of p_{11}^s and p_{12}^s is unknown, we shall tentatively assume the following two cases: (1) If p_{11}^s and p_{12}^s possess the same signs, then $|p_{66}^s| = 0.013$; (2) if they possess different signs, then $|p_{66}^s| = 0.151$. The actual relative sign will be determined in Sec.3.3 by comparing the experimentally observed diffraction intensity with those theoretically predicted from the two assumed kinds of values above.

Similarly the indirect photoelastic effect causes anisotropic Bragg diffraction through the effective photoelastic constant

$$p_{eff}^{in} = |p_{56}^{in} \sin\theta_D - p_{66}^{in} \cos\theta_D|$$

$$\simeq |p_{66}^{in}|, \qquad (3.2\text{-}48)$$

where Eq.(3.2-22) gives

$$p_{66}^{in} \simeq -\gamma_{62}\, e_{26}\, A/\varepsilon_0\, \varepsilon_{22}. \qquad (3.2\text{-}49)$$

On the other hand, it can be easily derived that the photoelasticity arising from the free-carrier density fluctuations may give rise to isotropic Bragg diffraction via

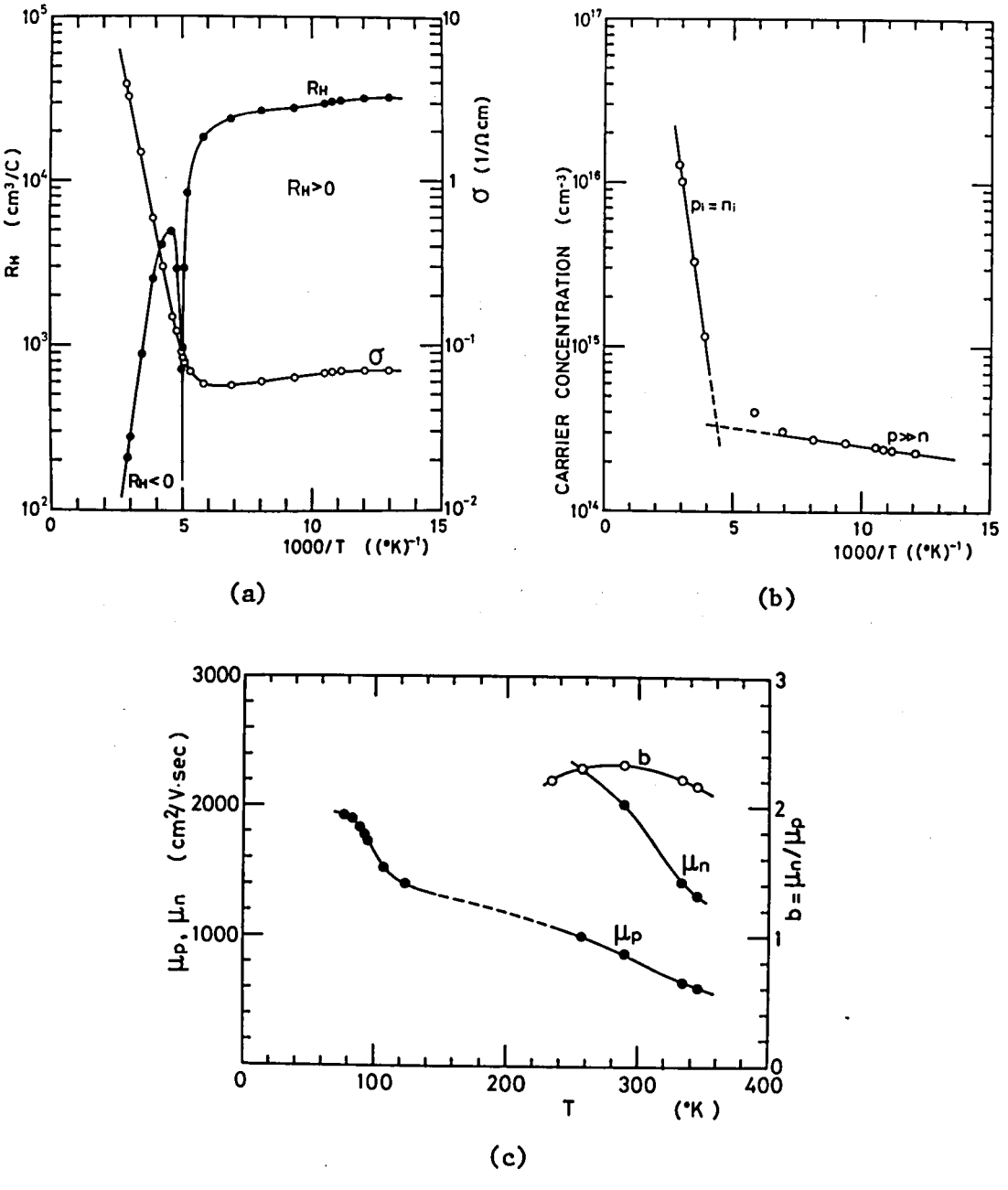

Fig.3.2-3 Results of Hall measurements.

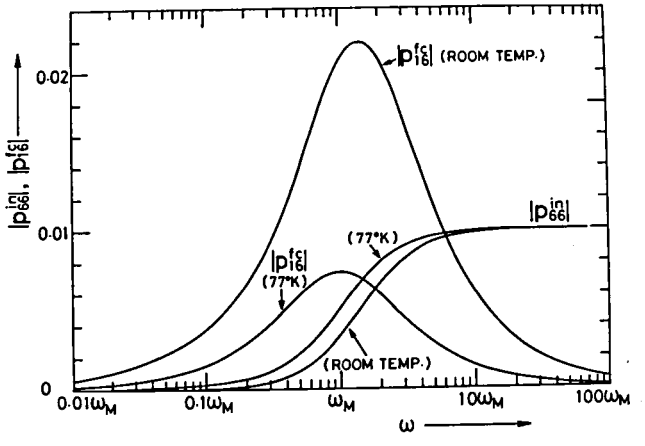

Fig.3.2-4 Theoretical plot of $|p_{66}^{in}|$ and $|p_{16}^{fc}|$ in Te as a fuction of acoustic frequency. The calculations have been carried out for Te in an intrinsic region at room temperature ($\omega_M = 2.15 \times 10^9$ Hz) and in a p-type extrinsic region at 77°K ($\omega_M = 1.0 \times 10^9$ Hz), respectively.

$$p_{eff}^{fc} = |p_{16}^{fc}| = \left| -\frac{e_{26}\, A}{(\kappa_{11})^2\, q\, v} \left(\frac{\kappa_{11}^n}{n_0} \frac{\omega_C^n}{1+j(\omega/\omega_D^n)} - \frac{\kappa_{11}^p}{p_0} \frac{\omega_C^p}{1+j(\omega/\omega_D^p)} \right) \right| . \tag{3.2-50}$$

In order to estimate the frequency characteristics of the two photoelastic constants predicted by Eqs.(3.2-48) and (3.2-50) above, the dielectric relaxation frequencies and the diffusion frequencies were determined from the Hall measurements. The sample was cut from the same crystal as used in the acousto-optic diffraction experiments in Sec.3.3. The results of the Hall measurements are shown in Figs. 3.2-3 (a), (b), and (c). The Hall reversal was observed at 200°K. The estimation of the electron and hole mobilities, i.e., μ_n and μ_p in the intrinsic region above the Hall reversal temperature was performed according to the method and formulas proposed by Grosse [30], from which we have $n_0 \simeq p_0 = 4.4 \times 10^{15} cm^{-3}$, $\mu_n = 1840$ cm^2/V sec, $\mu_p = 800$ cm^2/V sec, and $b = \mu_n/\mu_p = 2.3$ at room temperature. Using the

low frequency dielectric constant $\varepsilon_{22} = 33$ [31], we obtain $\omega_C^n = 7.11 \times 10^{10}$ Hz, $\omega_C^p = 3.09 \times 10^{10}$ Hz, $\omega_D^n = 6.46 \times 10^7$ Hz, and $\omega_D^p = 1.49 \times 10^8$ Hz. The expected variations of $|p_{66}^{in}|$ and $|p_{16}^{fc}|$ at 10.6 μm are plotted in Fig.3.2-4 as a function of acoustic frequency, where $\omega_M \equiv (\omega_C^n \omega_D^n)^{1/2} = (\omega_C^p \omega_D^p)^{1/2} = 2.15 \times 10^9$ Hz. The material constants used in the calculations are $e_{26} = -0.42$ C/m^2 [32], $m_n = 0.051\, m_0$, $m_p = 0.146\, m_0$ [33], $\kappa_{11} = N_o^2 = 22.98$ [23], and $\gamma_{62} = 6.97 \times 10^{-12}$ m/V. γ_{62} has been estimated from the nonlinear optical coefficient [34] $d_{11} = 920 \times 10^{-12}$ m/V employing Miller's rule [35]. At 77°K, this sample shows p-type extrinsic conduction with $p_0 = 2.3 \times 10^{14}$ cm^{-3}, $\mu_p = 1920$ cm^2/V sec, $\omega_C^p = 3.8 \times 10^9$Hz, $\omega_D^p = 2.7 \times 10^8$ Hz, and $\omega_M = (\omega_C^p \omega_D^p)^{1/2} = 1.0 \times 10^9$ Hz, from which $|p_{66}^{in}|$ and $|p_{16}^{fc}|$ at 77°K are calculated using Eqs.(3.2-30) and (3.2-31) as also illustrated in Fig.3.2-4. The frequency which gives the maximum value for $|p_{16}^{fc}|$ coincides with ω_M at 77°K, while at room temperature it is shifted toward higher frequencies but still located in the range $(\omega_D^n, \omega_D^p < \omega < \omega_C^n, \omega_C^p)$. For sufficiently high frequencies $(\omega \gg \omega_D^n, \omega_D^p)$, the free-carrier bunchings attain a scale much smaller than the Debye length [11] and are effectively smeared out by the thermal motion of the free carriers. The magnitude of $|p_{16}^{fc}|$ arising from the free-carrier density fluctuations is therefore considerably reduced. Figure 3.2-4 shows that the maximum attainable value for $|p_{16}^{fc}|$ is about 0.022 at the acoustic frequency of 3.03 GHz for room temperature and about 0.0074 at 1.00 GHz for 77°K. These values can be compared with the photoelastic constants listed in Table 3.1. In the intrinsic region at room temperature as discussed in Sec.3.2.A, considerable cancellation may take place between p_{16}^n and p_{16}^p. To make this point clear, p_{16}^n and p_{16}^p are evaluated by resolving them into their absolute values $|p_{16}^n|$ and $|p_{16}^p|$, and the phase angle ϕ between them. The results are illustrated in Fig.3.2-5. As expected, ϕ does not deviate very much from π and shows small but maximum deviation at $\omega = 0.0457\, \omega_M$. In the vicinity of the maximum of $|p_{16}^{fc}|$, about 35 % of $|p_{16}^n|$ is effectively cancelled by $|p_{16}^p|$

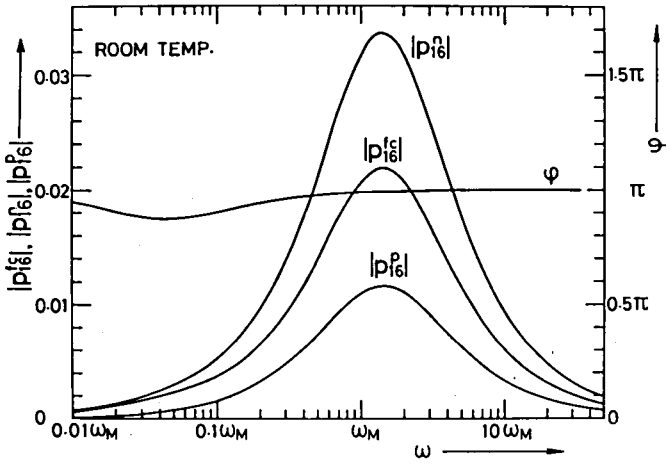

Fig.3.2-5 Dependences of $|p_{16}^{fc}|$, $|p_{16}^{n}|$, $|p_{16}^{p}|$, and ϕ on acoustic frequency at room temperature. $|p_{16}^{n}|$ and $|p_{16}^{p}|$ are the absolute values of the photoelastic constants respectively arising from the electron- and the hole-dencity fluctuation. ϕ is the phase angle between p_{16}^{n} and p_{16}^{p}. $|p_{16}^{fc}|$ is equal to $|p_{16}^{n} + p_{16}^{p}|$ and therefore is obtained as their overall effect. $\omega_M = 2.15 \times 10^9$ Hz.

so that the overall photoelastic constant $|p_{16}^{fc}|$ is reduced to about 65 % of $|p_{16}^{n}|$.

On the other hand, Fig.3.2-4 shows that $|p_{66}^{in}|$ increases monotonically with ω and, above ω_M, rapidly approaches its high-frequency limit value of 0.01.

For a given acoustic frequency, the expected diffraction intensities expressed by Eq.(3.2-40) can be determined by knowing the Bragg angles and the relevant effective photoelastic constants. In the acousto-optic diffraction experiments carried out at room temperature as described in Sec.3.3, a shear ultrasonic wave of 120 MHz was transmitted in the y direction. At this frequency, the angles of incidence and diffraction for the anisotropic Bragg diffractions are $\theta_I = 4.76°$ and $\theta_D = 6.18°$ (or, correspondingly, $\theta_I' = 23.42°$ and $\theta_D' = 31.18°$), while they are $\theta_I = \theta_D = 5.48°$ (or $\theta_I' = \theta_D' = 27.23°$) for the isotropic Bragg case. Besides, we have $p_{eff}^{in} \simeq |p_{66}^{in}| = 2.1 \times 10^{-5}$ and $p_{eff}^{fc} = |p_{16}^{fc}| = 2.5 \times 10^{-3}$ at 120 MHz. Therefore, (1) if the signs

of p_{11}^s and p_{12}^s are the same, the expected diffraction intensities are

$$I_D^d : I_D^{in} : I_D^{fc} = 1 : 2.6 \times 10^{-6} : 3.7 \times 10^{-2}; \qquad (3.2\text{-}51)$$

(2) if different,

$$I_D^d : I_D^{in} : I_D^{fc} = 1 : 1.9 \times 10^{-8} : 2.7 \times 10^{-4}, \qquad (3.2\text{-}52)$$

where I_D^d is the intensity of the diffracted light due to the direct effect, I_D^{in} is that due to the free-carrier screened indirect effect, and I_D^{fc} is that due to the free-carrier density fluctuations. The extremely small intensities of I_D^{in} may be neglected compared to I_D^d and I_D^{fc} at this acoustic frequency.

3.3 Experimental Results and Discussion

The experiments were performed at room temperature, where Te shows intrinsic conduction. A schematic illustration of the experimental arrangement is given in Fig.3.3-1. The Te sample was cut from a boule grown by the gradual cooling method. The preparation of the

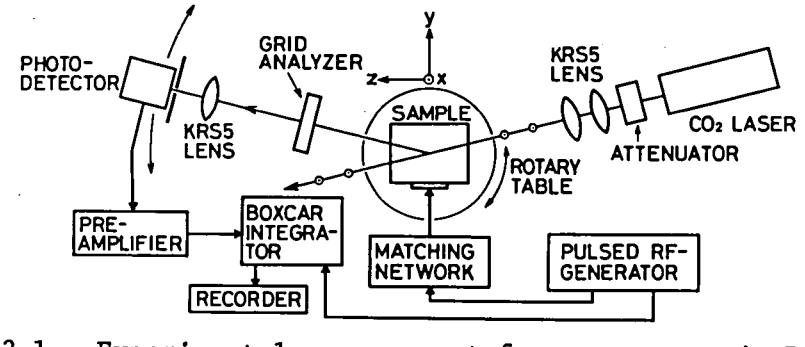

Fig.3.3-1 Experimental arrangement for acousto-optic Bragg diffraction in Te. The coordinate axes denote the crystallographic orientation for the Te sample.

sample was carried out in the same way as described in Sec.2.2. The parallelepiped size of the polished sample is $x \times y \times z = 13.5 \times 7.7 \times 12.5$ mm. The surface orientations were determined with respect to the cleavage plane (the $(10\bar{1}0)$, hence, the y plane) and believed to properly coincide with the corresponding crystallographic planes within an accuracy of much less than 1°.

For an ultrasonic transducers, a Se film epitaxially grown on the Te y-face was used, as described by Shiosaki, Kawabata, and Tanaka [36], by utilizing the fact that crystalline Se possesses an isomorphic structure to Te. The film grown on the y face serves as a transducer which generates only shear waves propagating along the y direction. As long as the deviation of the actual sample face from the ideal crystallographic y plane is negligibly small, unexpected excitations of other unwanted acoustic modes (which often lead to serious inconvenience when using bonded shear-mode transducers, owing mainly to misoriented bonding) can be easily avoided. In the present experiments, the transducer with a fundamental center frequency of about 51 MHz and fractional 3-dB bandwidth of about 90 % was fabricated. The usual pulse-echo measurements carried out prior to the acousto-optic diffraction experiments proved that the time intervals of any two adjacent echoes appearing in the acoustic echo train, as shown in Fig.3.3-2, precisely agreed with the value calcu-

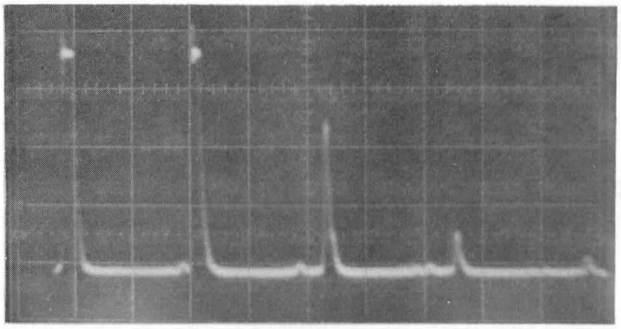

Fig.3.3-2 Acoustic echo train. Horizontal sweep: 5 μsec/div.

lated from the shear wave velocity, 1390 m/sec, and any noticeable spurious echo-pulses ascribable to other acoustic modes were not detected. In the acousto-optic diffraction experiments, the acoustic pulses with the carrier frequency of 120 MHz were excited by a pulsed rf generator utilizing the third-overtone frequency band of the transducer. The pulse width was chosen as 1 μsec.

A 10.6-μm *cw* CO_2 laser operating in the lowest transverse mode was used as a coherent infrared light source. The high-power output from the laser was reduced to about 20 mW with an optical attenuator in order to minimize the effects arising from light absorption. The well-collimated beam had a spot diameter of about 1 mm at the sample position. Any noticeable change was not observed in the electrical conductivity of the sample when the sample was irradiated by light with this level of intensity. The conductivity data of the sample at room temperature have already been given in Sec.3.2.B.

A KRS5 lens focused the diffracted beam through a narrow slit mounted in front of a HgCdTe photoconductive infrared detector. The polarization direction of the laser beam was carefully adjusted by rotating the Brewster plate inserted in the laser resonator so as to align parallel to the x axis within the sample. A grid analyzer placed in front of the KRS5 lens was used to determine the polarization direction of the diffracted beam. The motor-driven rotary table on which the sample was mounted was used to obtain the angle of incidence required from the Bragg conditions as precisely as possible. The photodetector was also mechanically rotated in the y-z plane about the sample to determine the diffraction angles precisely. The signal from the photodetector was recorded after integration by a Boxcar integtrator.

For the present transducer, L and H in Eq.(3.2-40) are respectively equal to 3.5 and 11.0 mm. Under these experimental conditions we have pure Bragg diffraction because $Q \gg 4\pi$. (For the meaning of Q, see Appendix.) At the acoustic frequency of 120 MHz, diffrac-

tion was observed for two different angles of incidence, $\theta_I' \simeq 23.9°$ and 27.1°. The lower trace in Fig.3.3-3 shows the acoustic echo train which was detected by the transducer and the upper trace is the wave form of the diffracted light pulse. Figure 3.3-4 shows the angular distribution of the diffracted light intensities recorded by rotating the photodetector about the sample for these two angles of incidence, the upper half of the figure for $\theta_I' \simeq 27.1°$ and the lower half for $\theta_I' \simeq 23.9°$. The lower half has been drawn on a vertical scale 100:1 to the upper half for the same acoustic power. The linear dependence of the diffracted light intensities on the acoustic power was carefully checked by varying the electric power applied to the transducer as shown in Fig.3.3-5, so that the small-signal approximation of Eq.(3.2-40) was well satisfied under the present experimental conditions. In the upper half of Fig.3.3-4, the polarization plane of the analyzer was set parallel to the polarization direction of the incident light and the diffraction angle corresponding to the peak position was obtained $\theta_D' \simeq 27.1°$ ($\simeq \theta_I'$). In the lower half, on the other hand, the polarization plane of the analyzer was set normal to that of the incident light and we have θ_D' $\simeq 31.6°$. Figure 3.3-6 shows the polarization states of the incident and diffracted lights measured as fuctions of rotation angles of the

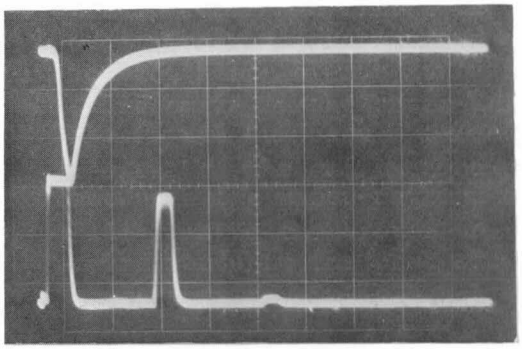

Fig.3.3-3 Upper: diffracted light pulse. Lower: acoustic pulse. Horizontal sweep: 5 μsec/div.

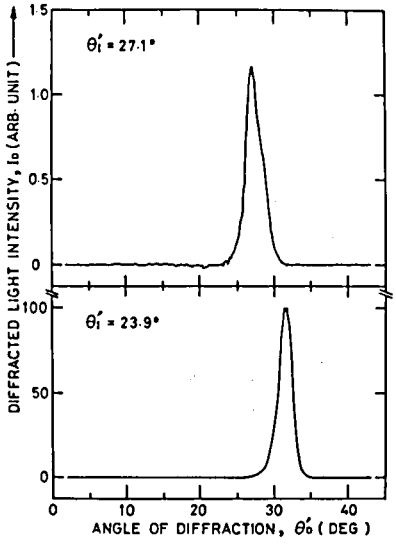

Fig.3.3-4 Angular distribution of the diffracted light intensities measured at the same acoustic power. In the upper-half of the figure, the angle of incidence $\theta_I' \simeq 27.1°$ and the polarization plane of the analyzer is parallel to the polarization direction of the incident light. In the lower-half, $\theta_I' \simeq 23.9°$ and the polarization plane of the analyzer is normal to the polarization direction of the incident light.

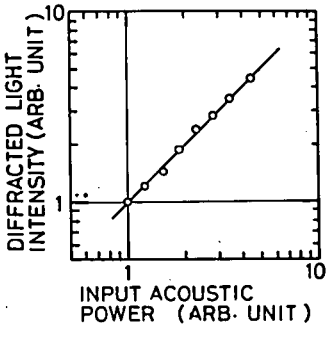

Fig.3.3-5 Dependence of diffracted light intensity on acoustic power.

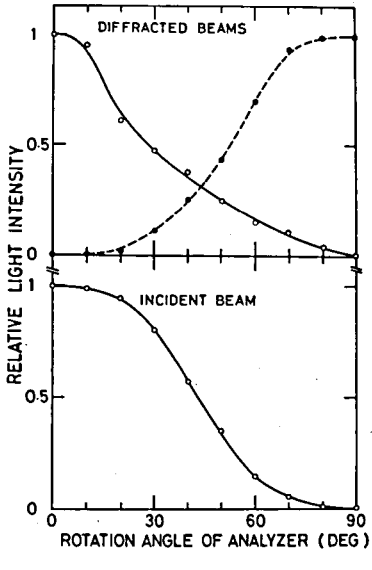

Fig.3.3-6 Polarization states of the incident and diffracted beams determined by rotating the polarization plane of the analyzer. The solid curve in the upper-half of the figure has been obtained with respect to the diffraction peak shown in the upper-portion of Fig. 3.3-4, while the broken curve corresponds to the peak shown in the lower-portion of Fig.3.3-4.

analyzer. The polarization state of the incident light is plotted in the lower half of the diagrm. The solid curve in the upper half of Fig.3.3-6 was obtained with respect to the diffraction peak given in the upper half of Fig.3.3-4, indicating that the polarization of the diffracted light is parallel to that of the incident light and hence was created by the isotropic Bragg diffraction. Quantitative agreements of the measured θ_I' and θ_D' with the calculation, i.e., $\theta_I' = \theta_D' = 27.23°$ also confirm that the diffraction arose according to the isotropic Bragg law. On the other hand, the broken curve which was obtained with respect to the diffraction peak in the lower half of Fig.3.3-4 suggests that the polarization of the diffracted light in this case is perpendicular to that of the incident light and hence the diffraction is anisotropic, for which the calculated Bragg angles are $\theta_I' = 23.42°$ and $\theta_D' = 31.18°$ and agree well with the observed angles of 23.9° and 31.6°. In addition, Fig.3.3-4 shows that the intensity of the observed isotropic diffraction relative to the intensity of the anisotropic diffraction is about 1.2×10^{-2}.

As we have seen in Sec.3.2.B, the isotropic diffraction observed in the experiments can not be explained only by taking account of the direct photoelastic effect. By the use of the Se transducer epitaxially grown on the moderately oriented Te sample, the possibility of excitation of unexpected spurious acoustic modes which might give rise to the isotropic diffraction was negligibly small. Besides, the plane of incidence and the polarization derection of the incident light had been closely adjusted. Even if we allow misalignment to a certain extent in the experimental conditions, the observed intensity of the isotropic diffraction is very much larger than that predicted solely from the direct photoelastic effect. Consequently, the possibility of an accidental contribution from the isotropic photoelastic tensor components of the direct effect, which might arise from possible experimental misorientations, can be ruled out. On the contrary, the observed relative intensity

(1.2×10^{-2}) is in satisfactory agreement with the theoretically predicted one ($I_D^{fc}/I_D^d = 3.7 \times 10^{-2}$ as given in Eq.(3.2-51)) within a factor of 3, leading to the conclusion that the observed isotropic diffraction should be attributed to the free-carrier density fluctuations.

This is the first time that an acousto-optic diffraction due to free-carrier density fluctuations accompanying an acoustic wave has been observed in an intrinsic semiconductor. It has been revealed that this effect gives rise to an appreciable contribution to diffraction intensity in Te for the optical wavelength of 10.6 μm. The essential agreement of the observed diffraction intensity with the theoretical prediction given by Eq.(3.2-51) suggests that the signs of p_{11}^s and p_{12}^s should be the same in Te.

3.4 Concluding Remarks

In this chapter, contributions from the free-carrier screened indirect photoelastic effect and from the free-carrier density fluctuations to the photoelasticity in piezoelectric semiconductors have been considered by taking the existence of both electrons ans holes into account. Explicit expressions for the effective photoelastic constants corresponding to these contributions have been derived on the basis of the small-signal acousto-electric theory. The results obtained are applicable either to extrinsic or to intrinsic semiconductors. The numerical evaluation of these contributions has been carried out by taking Te as an example. In accordance with the theoretical prediction, an appreciable diffraction ascribable to the free-carrier density fluctuations has been observed in the acousto-optic diffraction experiments

References

[1] O. Keller, Phys. Rev. B 11 (1975) 5059.

[2] O. Keller, Phys. Rev. B 13 (1976) 4612.

[3] O. Keller, J. Opt. Soc. Am. 68 (1978) 42.

[4] D. F. Nelson and M. Lax, Phys. Rev. Letters 24 (1970) 379.

[5] D. F. Nelson and M. Lax, Phys. Rev. B 3 (1971) 2778.

[6] D. F. Nelson, *Electronic, Optic, and Acoustic Interactions in Dielectrics* (Wiley, New York, 1979).

[7] V. V. Proklov, G. N. Shkerdin, and Yu. V. Gulyaev, Solid State Commun. 10 (1972) 1145.

[8] V. V. Proklov, V. I. Mirgorodsky, G. N. Shkerdin, and Yu. V. Gulyaev, Solid State Commun. 15 (1974) 1735.

[9] H. Sasaki, K. Tsubouchi, N. Chubachi, and N. Mikoshiba, J. Appl. Phys. 47 (1976) 2046.

[10] A. R. Hutson and D. L. White, J. Appl. Phys. 33 (1962) 40.

[11] J. H. McFee, *Physical Acoustics*, edited by W. P. Mason (Academic, New York, 1966) Vol.4, Pt.A, p.1.

[12] M. Fink and G. Quentin, Phys. Status Solidi A 4 (1971) 397.

[13] A. F. Gibson, Proc. Phys. Soc. B 69 (1956) 488.

[14] P. M. Platzman and P. A. Wolf, *Waves and Interactions in Solid State Plasmas* (Academic, New York, 1973).

[15] S. Fukuda, T. Karasaki, T. Shiosaki, and A. Kawabata, Phys. Rev. B 20 (1979) 4109.

[16] T. Ishiguro and T. Tanaka, J. Phys. Soc. Jpn. 21-suppl. (1966) 489.

[17] G. Quentin and J. M. Thuilier, Phys. Letters 19 (1966) 3.

[18] G. Quentin and J. M. Thuillier, J. Phys. Soc. Jpn. 21-suppl. (1966) 493.

[19] G. Quentin and J. M. Thuillier, Solid State Commun. 4 (1966) 3.

[20] T. Ishiguro and T. Tanaka, Jpn. J. Appl. Phys. 6 (1967) 864.

[21] T. Ishiguro, A. Hotta, T. Tanaka, Jpn. J. Appl. Phys. 5 (1966)

335.

[22] J. F. Nye, *Physical Properties of Crystals* (Clarendon, Oxford, 1957) p.943.

[23] N. van Tran, Onde Electr. 47 (1967) 965.

[24] W. R. Klein and B. D. Cook, IEEE Trans. Sonics Ultrason. SU-14 (1967) 123.

[25] R. W. Dixon, IEEE J. Quantum Electron. QE-3 (1967) 85.

[26] N. Uchida and N. Niizeki, Proc. IEEE 61 (1973) 1073.

[27] D. F. Nelson and P. D. Lazay, Phys. Rev. B 6 (1972) 3109.

[28] S. Fukuda, T. Shiosaki, and A. Kawabata, Jpn. J. Appl. Phys. 15 (1976) 927.

[29] S. Fukuda, T. Shiosaki, and A. Kawabata, J. Appl. Phys. 50 (1979) 3899.

[30] P. Grosse, *Springer Tracts in Modern Physics* (Springer, Verlag, 1969) Vol.48, p.144.

[31] H. Wagner, Z. Phys. 193 (1966) 218.

[32] G. Arlt and P. Quadflieg, Phys. Status Solidi 32 (1969) 687.

[33] Y. Miura and C. Hirose, J. Phys. Soc. Jpn. 33 (1972) 1522.

[34] J. H. McFee, G. D. Boyd, and P. H. Schmidt, Appl. Phys. Letters 17 (1970) 57.

[35] R. C. Miller, Appl. Phys. Letters 5 (1964) 17; and Eq.(7.15) in S. H. Wemple and M. DiDomenico Jr., in *Applied Solid State Science*, edited by R. Wolf (Academic, New York, 1972) Vol.3, p.293.

[36] T. Shiosaki, A. Kawabata, and T. Tanaka, Jpn. J. Appl. Phys. 9 (1970) 631.

CHAPTER 4

APPLICATION OF ACOUSTO-OPTIC EFFECTS IN Te TO OPTICAL SECOND HARMONIC GENERATION (ACOUSTO-OPTICALLY PHASE-MATCHED NONCOLLINEAR OPTICAL SECOND HARMONIC GENERATION IN Te)

4.1 Introduction

In nonlinear optical interactions such as optical harmonic generation, possibility of phase-matching is one of the most essential conditions to be satisfied in order to produce large enough converted signals. The most frequently performed technique for the phase-matching is the one utilizing the birefringence of nonlinear optical materials. In these materials, there are special directions known as the index-matching directions, and their angles measured from the optic axis are usually referred to as the matching angle θ_m. The phase-matching condition can be satisfied only when the incident optical wave with specific polarization is transmitted in these directions.

On the other hand, this chapter describes two kinds of acousto-optically phase-matched noncolliear optical second harmonic generations (SHG) that have been experimentally observed for the first time in Te as novel phase-matching techniques. The phenomena are interpreted as being due to mixing of an incident light and acousto-optically scattered light (four-wave interaction) and due to mixing of two acousto-optically scattered lights (five-wave interaction), respectively. The phase-matching techniques that are

described here are especially suitable for Te since as we have seen, its acousto-optic effects are exceptionally large in addition to the large nonlinear optical coefficient ($d_{11} = 920 \times 10^{-12}$ m/V) [1-4].

4.2 Theoretical

4.2.A *SHG due to four-wave interaction*

The possibility of this technique has been theoretically predicted by Harris et al and Nelson et al [5-7]. The basic principle of this technique is to compensate the phase-mismatch $\Delta\vec{k}$ in the conventional SHG by interacting an acoustic wave that has the wave vector $\vec{K}$ ($= \Delta\vec{k}$). The output second harmonic (SH) wave (ω_C, $\vec{k}_C$) is then produced due to mixing of two input waves (ω_A, $\vec{k}_A$) and one input acoustic wave (Ω, $\vec{K}$). Therefore, the phenomenon consists of a four-wave interaction process. Exactly speaking, the output frequecy ω_C ($= 2\omega_A + \Omega$) differs from the exact SH frequency $2\omega_A$ by the negligible amount of Ω.

For a given input optical frequency ω_A and material, the acoustic mode which should be used is determined from the considerations that the phase-matching can be attained at a moderate acoustic frequency and that the acoustic wave can actually produce the nonlinear polarization that governs the nonlinear process. In the present experiments, a longitudinal wave propagating in the crystallographic x direction with the velocity of 2290 m/sec was chosen as such an acoustic wave. In this case, there are two kinds of interactions [6,7]: One is the direct mixing of the three input waves through the fifth-rank mixing tensor $\chi_{ifg\ kl}$ as shown in Fig.4.2-1 (a), where $u_{k,1} = \partial u_k / \partial x_1$ is the acoustic displacement gradient corresponding to the acoustic field [8]. The other is a two-step indirect mixing process as illustrated in Fig.4.2-1 (b). The latter indirect process arises from the acousto-optic scattering (the fre-

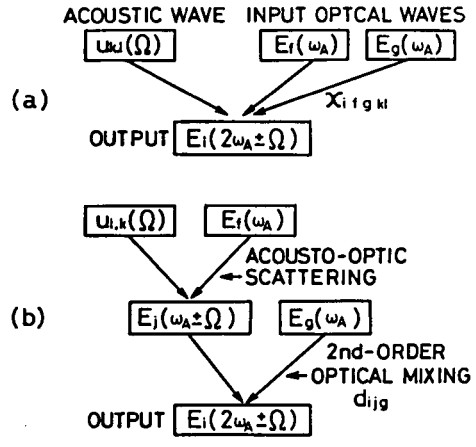

Fig.4.2-1 Nonlinear four-wave interaction processes in Te. (a) direct mixing and (b) two-step indirect mixing of two optical and one acoustic waves.

quency of the scattered optical wave: $\omega_B = \omega_A + \Omega$) followed by the optical mixing ($\omega_C = \omega_A + \omega_B$). Accordingly, the phase-matching condition for the direct process is

$$\vec{k}_C = 2\vec{k}_A + \vec{K} \ . \qquad (4.2\text{-}1)$$

On the other hand, to realize the indirect process effectively, it is essential to satisfy the following two conditions simultaneously:

$\vec{k}_B = \vec{k}_A + \vec{K}$ (the Bragg condition required for the acousto-optic scattering) (4.2-2-a)

and

$\vec{k}_C = \vec{k}_A + \vec{k}_B$ (the phase-matching condition required for the optical mixing). (4.2-2-b)

When both Eqs.(4.2-2-a) and (4.2-2-b) are satisfied, the efficiency of the indirect process can be larger than that of the direct process by several orders of magnitude. To our knowledge, however, this indirect process has never been experimentally exploited up to date [9]. In what follows, we ignore the contribution from the

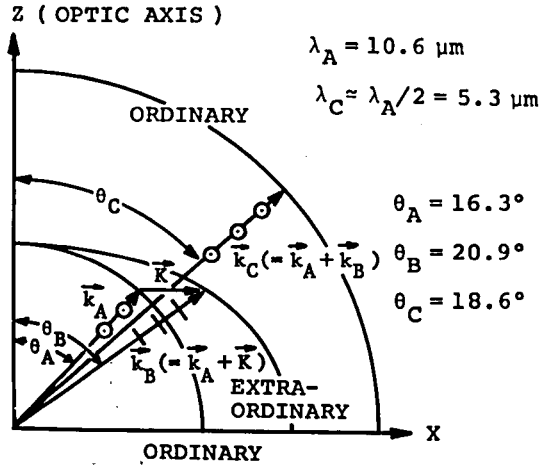

Fig.4.2-2 Wave vector diagram for the four-wave interaction in Te.

direct mixing process since we shall treat only the case in which Eqs.(4.2-2-a) and (4.2-2-b) are nearly satisfied.

Now, we shall derive an expression for the induced nonlinear polarization which governs the nonlinear optical process. The crystal axes and the wave vector diagram corresponding to the interaction geometry are shown in Fig.4.2-2. Since we concern ourselves only with a longitudinal acoustic wave in the x direction, we can use the strain S_1 ($= S_{11}$) instead of the displacement gradient $u_{1,1}$ as the relevant variable to express the acoustic field, and hence the contribution from the rotation of the volume element can be omitted [8]. The electric fields of the incident and the acousto-optically scattered wave and the strain, denoted respectively by E_A, E_B, and S_1, can be expressed as

$$E_A(x, z, t) = \frac{1}{2} E_A(z) \exp[\, j(\omega_A t - \vec{k}_A \cdot \vec{r})\,] + c.c., \qquad (4.2\text{-}3\text{-}a)$$

$$E_B(x, z, t) = \frac{1}{2} E_B(z) \exp[\, j(\omega_B t - \vec{k}_B \cdot \vec{r})\,] + c.c., \qquad (4.2\text{-}3\text{-}b)$$

and

$$S_1(x,\ t) = \frac{1}{2} S_1 \exp[\, j(\Omega t - Kx)\,] + c.c., \qquad (4.2\text{-}3\text{-}c)$$

where $\vec{k}_A \cdot \vec{r} = k_A (x \sin\theta_A + z \cos\theta_A)$, $\vec{k}_B \cdot \vec{r} = k_B (x \sin\theta_B + z \cos\theta_B)$, and $\omega_B = \omega_A + \Omega$. In a similar way the output optical wave can be expressed by

$$E_C(x,\ z,\ t) = \frac{1}{2} E_C(z) \exp[\, j(\omega_C t - \vec{k}_C \cdot \vec{r})\,] + c.c., \qquad (4.2\text{-}4)$$

where $\omega_C = 2\omega_A + \Omega$ and $\vec{k}_C \cdot \vec{r} = k_C (x \sin\theta_C + z \cos\theta_C)$. In the above expressions, we assumed the fields in the form of plane wave. These waves are governed by the following nonlinear wave equation:

$$\left(\nabla^2 - \mu_0 \varepsilon \frac{\partial^2}{\partial t^2} \right) \vec{E} = \mu_0 \frac{\partial^2 \vec{P}_{NL}}{\partial t^2} , \qquad (4.2\text{-}5)$$

where ε is the dielectric permittivity and $\vec{P}_{NL}$ is the induced nonlinear polarization. In the geometry shown in Fig.4.2-2, the incident optical wave E_A is transmitted as an ordinary wave in the direction making an angle θ_A from the optic axis, and hence its polarization is parallel to the y axis. The intermediate optical wave E_B is then generated as an extraordinary wave in the direction θ_B by the anisotropic Bragg scattering due to the photoelastic tensor component p_{41}. In this step, the acousto-optically induced nonlinear polarization which radiates E_B is given by

$$P_{NL}^{AO}(x,\ z,\ t) = \varepsilon_0 n_o^2\ n_e^2(\theta_D)\, p_{41} \sin\theta_B \cos\rho\ S_1\, E_A(x,\ z,\ t) \qquad (4.2\text{-}6)$$

with

$$n_e(\theta_B) = 1/[(\cos\theta_B/n_o)^2 + (\sin\theta_B/n_e)^2]^{1/2} \qquad (4.2\text{-}7)$$

and

$$\cos\delta = (n_e^2 \cos^2\theta_B + n_o^2 \sin^2\theta_B)/(n_e^4 \cos^2\theta_B + n_e^4 \sin^2\theta_B)^{1/2} , \tag{4.2-8}$$

where n_o and n_e are the ordinary and the extraordinary refractive index at ω_A ($\simeq \omega_B$), respectively, and δ is the angle between the Poynting vector and the propagation direction of E_B. Substituting Eqs.(4.2-3-b) and (4.2-6) into Eq.(4.2-5) and neglecting the second-order derivative, we obtain the following differential equation with respect to the field amplitude $E_B(z)$:

$$\frac{dE_B(z)}{dz} = -j A S_1 E_A(z) \exp(-j \Delta k z) \tag{4.2-9}$$

and

$$A = \omega_B n_o^2 n_e(\theta_B) p_{41} \sin\theta_B \cos\delta/4 c \cos\theta_B , \tag{4.2-10}$$

where $\Delta k = k_A \cos\theta_A - k_B \cos\theta_B$, $k_A = \omega_A n_o/c$, $k_B = \omega_B n_e(\theta_B)/c$, c is the optical velocity in vacuum, and we assume that there is no phase-mismatch for the x components. For simplicity, we shall solve Eq. (4.2-9) in the usual small signal approximation, that is, we consider the case where the depletion of the input optical wave is negligible so that $dE_A(z)/dz \simeq 0$ and $E_A(z) \simeq E_A(0)$. Then Eq.(4.2-9) yields

$$E_B(z) = -j A S_1 E_A(0) z \left(\frac{\sin(\Delta k z/2)}{\Delta k z/2}\right) \exp(- j \Delta k z/2). \tag{4.2-11}$$

When the Bragg condition (Eq.(4.2-2-a)) is satisfied so that $\Delta k = 0$, the electric field amplitude of the acousto-optically scattered wave is obtained as

$$E_B(z) = -j A S_1 E_A(0) z . \tag{4.2-12}$$

In the next step, the output SH wave E_C is generated as an ordinary wave in the direction of θ_C by mixing of the above acousto-optically scattered wave E_B with the input optical wave E_A via the second-order optical mixing effect. Thus the polarization direction of E_C is again parallel to the y axis. The induced nonlinear polarization which radiates E_C has, therefore, only one component along the y axis. The simple argument similar to that in the conventional optical-mixing effect gives the expression for this polarization as [10,11]

$$P_{NL}(x,\ z,\ t) = \frac{1}{2} P_{NL}(z) \exp\{ j[\omega_C t - (\vec{k}_A + \vec{k}_B)\cdot\vec{r}]\} + c.c., \tag{4.2-13-a}$$

and

$$P_{NL}(z) = -2\,\varepsilon_0\, d_{11}\, E_A(0)\, E_B(z) \cos(\theta_B - \delta)\ . \tag{4.2-13-b}$$

where d_{11} is the nonlinear optical coefficient. When the Bragg condition is satisfied, Eq.(4.2-13-b) can be replaced by

$$P_{NL}(z) = 2\,j\,\varepsilon_0\, d_{11}\, A \cos(\theta_B - \delta)\, S_1\, [E_A(0)]^2\, z\ . \tag{4.2-13-c}$$

In this way, we have derived the expression for the induced nonlinear polarizations which govern the entire nonlinear process.

The solution for E_C can be obtained by substituting Eqs.(4.2-4) and (4.2-13-a) into Eq.(4.2-5). When the second phase-matching condition expressed by Eq.(4.2-2-b) is simultaneously satisfied, the output SH power P_C obeys the following relation:

$$P_C \propto L^4\, P_{ac}\, P_A{}^2\ , \tag{4.2-14}$$

where P_A is the input optical power, P_{ac} is the acoustic power, and L is the effective interation length ($\simeq$ the width of the acoustic

column).

4.2.B *SHG due to five-wave interaction*

The wave vector diagram for another phase-matching method is schematically illustrated in Fig.4.2-3, where a shear acoustic wave propagating in the y direction with the displacement parallel to the x axis has been chosen. As illustrated in Fig.4.2-4, this nonlinear effect consists of two-step indirect mixing process, which arises from the acousto-optic scattering of the input optical wave from the acoustic wave, followed by the second harmonic generation of the scattered wave. The frequencies of the acousto-optically scattered wave and output wave are therefore $\omega_B = \omega_A + \Omega$ and $\omega_C = 2\,\omega_B$, respec-

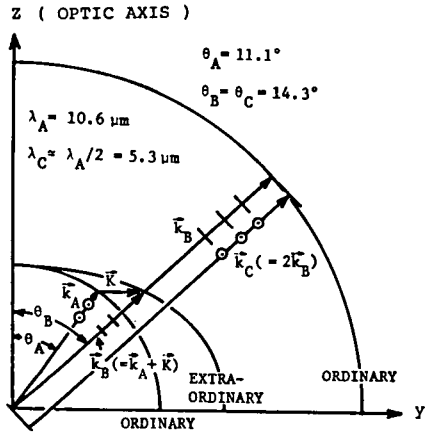

Fig.4.2-3 Wave vector diagram for the five-wave interaction in Te.

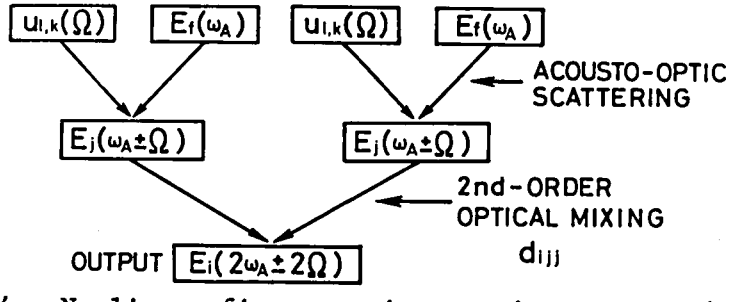

Fig.4.2-4 Nonlinear five-wave interaction process in Te.

tively. The output optical frequency ω_C ($= 2\omega_A + 2\Omega$) again differs from the exact SH frequency ($2\omega_A$) by the negligible amount of 2Ω. The phase-matching conditions required for this process are

$$\vec{k}_B = \vec{k}_A + \vec{K} \quad \text{(the Bragg condition)} \tag{4.2-15-a}$$

and

$$\vec{k}_C = 2\vec{k}_B \quad \text{(for the optical mixing)} \tag{4.2-15-b}$$

When Eqs.(4.2-15-a) and (4.2-15-b) are simultaneously satisfied, the output SH power P_C obeys the following relation:

$$P_C \propto L^6 P_{ac}^2 P_A^2 \ , \tag{4.2-16}$$

where the depletion of P_A is again ignored.

4.3 Experimental Results

4.3.A *SHG due to four-wave interaction*

The experiments were carried out in the setup as shown in Fig. 4.3-1. The relating refractive indices are $n_o = 4.7939$ and $n_e = 6.2433$ at 10.6 μm, and $n_o = 4.855$ at 5.3 μm [12,13]. The crystal size was $x \times y \times L = 6.3 \times 7.4 \times 8.4$ mm, where the direction of L is as defined in Fig.4.3-1. Pulsed longitudinal acoustic waves (pulse width: about 2 μsec) propagating in the x direction ($v = 2290$ m/sec) were generated by a 36°-rotated y-cut $LiNbO_3$ transducer cemented on the x plane of the crystal. The thickness of the transducer was adjusted by polishing so that its fundamental frequency was about 88 MHz. The cross section of the transducer was $y \times z = 3.0 \times 6.0$ mm. The peak acoustic powers up to about 50 W were used. The impedance

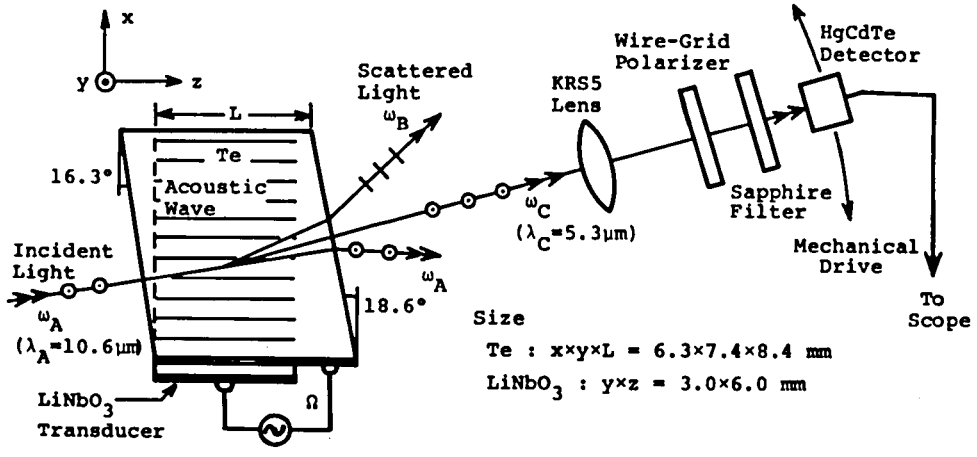

Fig.4.3-1 Experimental arrangement.

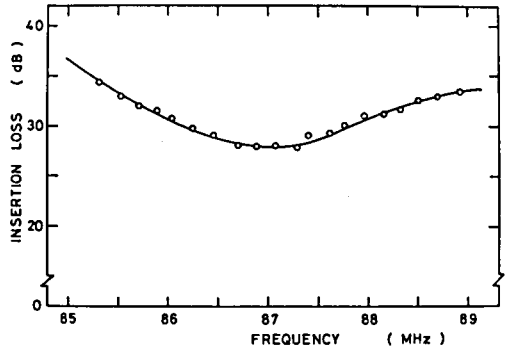

Fig.4.3-2 Insertion loss.

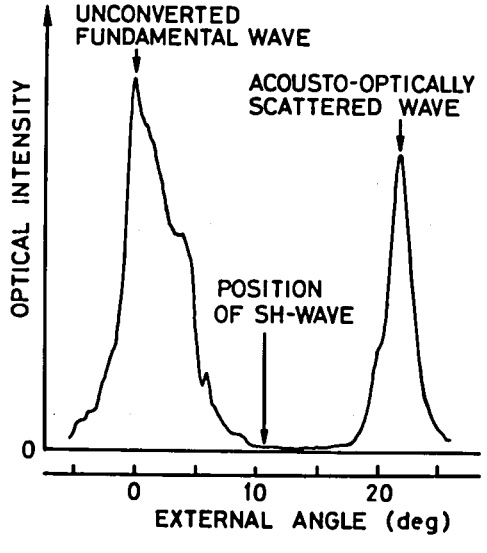

Fig.4.3-3 Intensity distributions of the emergent optical signals. The angles were measured outside the crystal.

of the transducer was matched to the 50-Ω electrical source through the MATEC matching network MODEL MN70. A 10.6-μm beam from a CO_2 laser was focused with a KRS5 lens into the Te crystal so as to propagate at an angle $\theta_A = 16.3°$ as an ordinary wave polarized along the y axis. The peak power of the laser beam was about 50 W at a repetition rate of 100 sec^{-1}. The width of the laser pulse was estimated to be 0.3 to 0.4 μsec. The confocal parameter and the waist radius of the beam within the crystal were 80 mm and 170 μm, respectively. The acoustic pulse was triggered by an electrical pulse from the CO_2 laser. The timing of the acoustic pulse with respect to the laser pulse was adjusted by feeding the trigger pulse through a delay circuit. Figure 4.3-2 shows the tuned electrical insertion loss of the sample.

In order to realize the first step of the interactions, the acoustic frequency was tuned to 88.8 MHz so as to satisfy the first phase-matching condition that is given by Eq.(4.2-2-a). In this geometry, the intermediate extraordinary wave (ω_B) polarized in the x-z plane was generated in the direction of $\theta_B = 20.9°C$ by the anisotropic Bragg scattering. The second condition (4.2-2-b) was then automatically satisfied at the frequency of 88.8 MHz and the output SH wave ($\lambda_C = 5.3$ μm) appeared as an ordinary wave in the direction of $\theta_C = 18.6°$.

The emergent optical waves were detected by a HgCdTe photoconductive infrared detector. The SH power was separated from the unconverted fundamental by a sapphire-plate filter. The polarization directions of the waves were determined by the wire-grid polarizer inserted in front of the sapphire filter. Figure 4.3-3 shows the intensity distributions of the emergent optical signals measured by rotating the detector about the Te crystal, in which the incident directions of the laser beam was kept at $\theta_A = 16.3°$. The distributions of the unconverted fundamental wave ($\lambda_A = 10.6$ μm) and the acousto-optically scattered wave were obtained without the sapphire

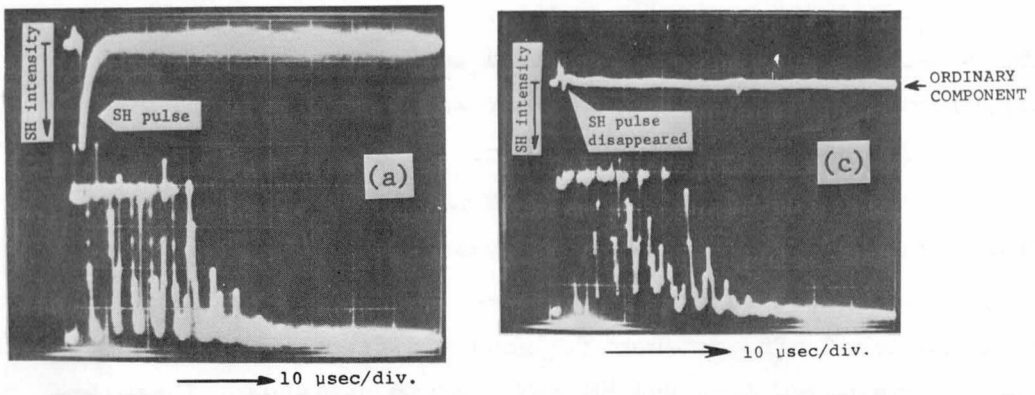

Fig.4.3-4 The wave form of the observed SH signal (upper trace) and the acoustic echo train (lower trace). The polarizer was set so as to pass only the ordinary wave (a), and was rotated by 90° so as to pass the extra-ordinary wave (b). The acoustic frequency was detuned to 86 MHz in (c).

filter, where the CO_2 laser was operated in the *cw* condition with the output power of about 0.5 W since the distribution recording of the pulsed signal was not obtainable with our present experimental aparatus. On the other hand, the position of the SH signal was determined using the sapphire filter and the laser in the pulsed operation. The intensity peaks of the acousto-optically scattered wave and the SH wave were observed at the positions 21.8° and 10.7° away from the emergent direction of the fundamental wave outside the cryatal respectively and agreed well with their calculated positions of 22.5° and 11.1°.

Figure 4.3-4 (a) shows the wave form of the observed SH signal and the acoustic echo train detected by the $LiNbO_3$ transducer, where the polarizer was set so as to pass only the ordinary-wave component. In the experiment shown in Fig.4.3-4 (a), about 18 % of the fundamen-

tal power was acousto-optically scattered into the intermediate wave and the obtained SH power was estimated to be the order of 10^{-3} W. The corresponding conversion efficiency was the order of 10^{-5} with the fundamental power of 50 W. However, the strong fluctuation of the laser power prohibited the accurate measurements. When the polarizer was rotated by 90° so as to pass the extraordinary wave, no SH power was detected as in Fig.4.3-4 (b). When the acoustic power was switched off, or when the acoustic frequency was changed, as shown in Fig.4.3-4 (c), the SH power again vanished. These experimental evidences prove that the detected output was due to the nonlinear process described above.

4.3.B *SHG due to five-wave interaction*

Figure 4.3-5 shows the Te crystal which was used in this experiment. The crystal size was $x \times y \times L = 8.0 \times 6.7 \times 10.3$ mm, where L is as defined in Fig.4.3-5. Pulsed shear acoustic waves (pulse width: about 2 μsec) propagating in the y direction (v = 1390 m/sec) were generated by a 163°-rotated y-cut $LiNbO_3$ transducer, The Poynting vector of this acoustic wave tilts by about 44° from the propagation direction as schematically shown in Fig.4.3-5. The transducer size was $x \times z = 3.5 \times 4.0$ mm. The experimental conditions were essentially the same as in the previously described experiments using a longitu-

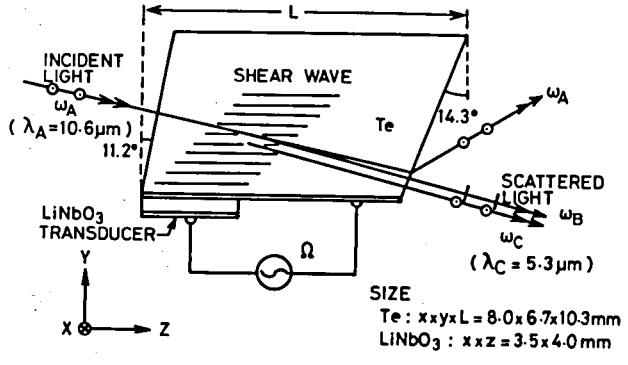

Fig.4.3-5 Te crystal used in the five-wave interaction.

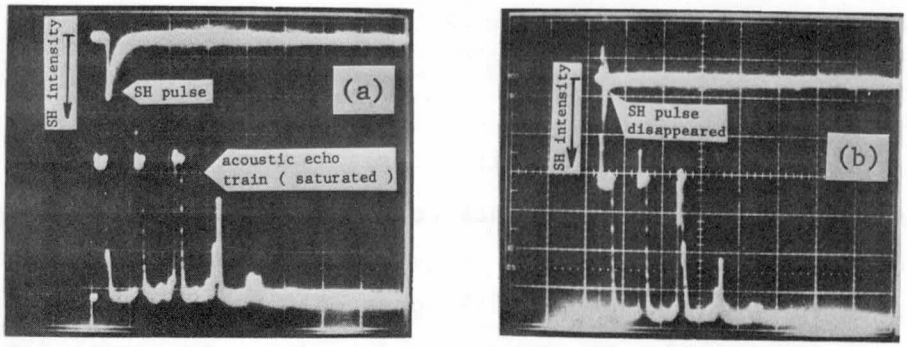

Fig.4.3-6 The wave forms of the observed SH signal and the acoustic echo train. The polarizer was set so as to pass only the ordinary wave (a), and was rotated by 90° so as to pass only the extraordinary wave (b). Horizontal sweep: 10 μsec/div.

dinal wave propagating in the x direction. The incident light from the pulsed CO_2 laser was focused with a KRS5 lens into the crystal which propagated in the y-z plane at an angle $\theta_A = 11.1°$ as an ordinary wave polarized along the x axis. The Bragg condition (4.2-15-a) was fulfilled at the acoustic frequency of 36.3 MHz and the intermediate extraordinary wave (ω_B) polarized in the y-z plane was generated in the direction of $\theta_B = 14.3°$ by the anisotropic Bragg scattering. Since the second phase-matching condition given by Eq.(4.2-15-b) was automatically satisfied at $\theta_B = 14.3°$, the output SH wave appeared as an ordinary wave in the same direction. Figure 4.3-6 (a) shows the wave form of the observed SH signal separated from the unconverted fundamental by the sapphire filter, where the polarizer was set so as to pass only the ordinary wave component. The SH signal disappeared when the polarizer was rotated by 90° so as to pass the extraordinary component as shown in Fig.4.3-6 (b). In this experiment, about 10 % of the fundamental power was acousto-optically scattered into the intermediate wave and the produced SH power was about 3×10^{-4} W with the fundamental input power of about 50 W. The conversion efficiency was, therefore, about 6×10^{-6}.

4.4 Discussion

For comparison with the results thus far described, the SHG experiments making use of conventional collinear index-matching were carried out with a *cw* CO_2 laser. The experimental setup was the same as used in the acousto-optically phase-matched SHG except for the Te crystal measured. The fundamental beam was transmitted as an extraordinary wave in the y-z plane at the index-matching angle θ_m from the optic axis. The SH wave was then generated as an ordinary wave polarized along the x axis. The crystal was obliquely polished at the desired angle for θ_m. Fig.4.4-1 shows the SH output as a function of the external incident angle when the crystal was rotated about the x axis. For the calculated θ_m of 14.3°, the measured θ_m was 15.3°. The deviation of about 1.0° is considered as mostly due to the misorientation of the crystal. For this interaction geometry, the induced nonlinear polarization P_{NL} and the conversion efficiency

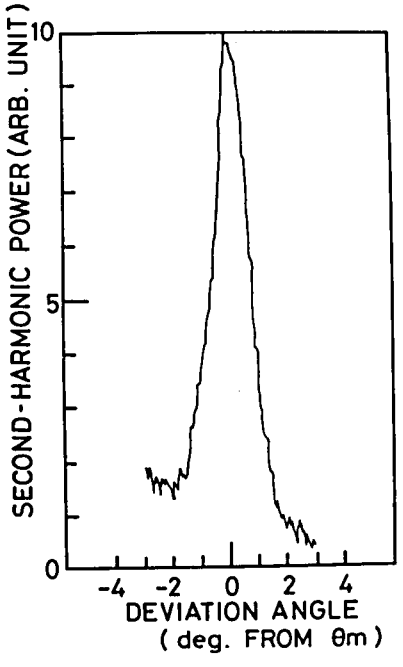

Fig.4.4-1 SH power generated by the conventional collinear index-matching as a function of external angle deviation from θ_m.

η are given by

$$P_{NL} = -\varepsilon_0 d_{11} \cos^2\theta_m E_e^2 \qquad (4.4\text{-}1)$$

and

$$\eta = P^{2\omega}/P^{\omega} \propto L^2 P^{\omega}, \qquad (4.4\text{-}2)$$

where E_e is the electric field amplitude of the incident expraordinary wave, $P^{2\omega}$ and P^{ω} are the SH and the fundamental power, and L is the effective interaction length. When the crystal with L = 13 mm was used, the conversion efficiency η of about 10^{-4} was obtained at the fundamental power of $P^{\omega} \simeq 0.5$ W. Now, suppose that the collinear index-matched SHG is carried out in the same experimental conditions as in the above-mentioned acousto-optically phase-matched SHG utilizing the four-wave interaction, i.e., L ≃ 6 mm and $P^{\omega} \simeq 50$ W. Then the calculation of Eq.(4.4-2) yields $P^{2\omega} \simeq 0.1$ W and $\eta \simeq 2 \times 10^{-3}$. Therefore, it is concluded that the efficiency obtained in the acousto-optically phase-matched SHG is about 1/100 times as small as that obtainable in the conventional collinear index-matched SHG.

In the above discussion, we have derived the expressions for the produced SH power for the cases in which the pump depletion can be ignored. However, the present experimental conditions are considered as situated about at the applicable limit of the above discussion since the results in Figs.4.3-4 and 4.3-6, for example, showed the depletion of about 18 and 10 % of the total fundamental power respectively and the most part of the depleted powers were converted into the acousto-optically scattered waves.

4.5 Concluding Remarks

In this chapter, the experiments using longitudinal acoustic

waves propagating in the x direction and shear waves propagating in the y direction were successfully demonstrated as examples for the novel phase-matching technique for SHG utilizing the acousto-optic interactions in Te. There are also several other acoustic waves propagating in other directions which satisfy Eqs.(4.2-2-a) and (4.2-2-b), and Eqs.(4.2-15-a) and (4.2-15-b), and hence the restriction for the crystal orientation is much relaxed as compared with the conventional collinear index-matching technique. One of the examples is a shear wave propagating in the z direction ($v = 2240$ m/sec) with the frequency of 27.6 MHz. The calculation shows that the fundamental ordinary wave incident 20.8° away from the z axis and the intermediate acousto-optically scattered extraordinary wave propagating in the direction of 20.2° can produce the output SH wave in the direction of 20.5° due to the four-wave interaction. Besides, it is possible to apply this technique to a parametric oscillator in which the oscillation frequencies can be varied by changing the acoustic frequency in a similar way to that discussed by Harris et al [5] for the collinear case.

References

[1] J. H. McFee, G. D. Boyd, and P. H. Schmidt, Appl. Phys. Letters 17 (1970) 57.

[2] R. W. Dixon, J. Appl. Phys. 38 (1967) 5149.

[3] S. Fukuda, T. Shiosaki, and A. Kawabata, Jpn. J. Appl. Phys. 15 (1976) 927; J. Appl. Phys. 50 (1979) 3899.

[4] S. Fukuda, S. Ikeda, T. Shiosaki, and A. Kawabata, Jpn. J. Appl. Phys. 18 (1979) suppl.18-1, p.413; 1978 IEEE Ultrasonics Symp. Proc. IEEE Cat. #78CH 1344-1SU (1978) 82.

[5] S. E. Harris, R. W. Wallace, and C. F. Quate, IEEE J. Quatum Electron. 4 (1968) 354.

[6] D. F. Nelson and M. Lax, Phys. Rev. B 3 (1971) 2795.

[7] D. F. Nelson, *Electronic, Optic, and Acoustic Interactions in Dielectrics* (Wiley, New York, 1979).

[8] D. F. Nelson and M. Lax, Phys. Rev. Letters 24 (1970) 379.

[9] G. D. Boyd, F. R. Nash, and D. F. Nelson, Phys. Rev. Letters 24 (1970) 1298.

[10] A. Yariv, *Quantum Electronics* (Wiley, New York, 1975).

[11] S. T. Kurtz, *Quantum Electronics*, edited by H. Rabin and C. L. Tang (Academic, New York, 1975) Vol.1, Pt.A, p.209.

[12] R. S. Caldwell and H. Y. Fan, Phys. Rev. 114 (1956) 664.

[13] N. van Tran, Onde Electr. 47 (1967) 965.

CHAPTER 5

ACOUSTO-OPTIC PROPERTIES OF AMORPHOUS Se

5.1 Introduction

Se is known as one of the peculiar materials which exist either in amorphous or in crystallin form at room temperature. Though Se crystal is a semiconductor with trigonal structure similar to Te, its electrical properties are more like those of insulators since the electrical conductivity of trigonal Se is as low as 10^{-5} to 10^{-6} $(\Omega \times cm)^{-1}$ at room temperature, and therefore the Joule heating arising from the application of high electric field is relatively small. For this reason, trigonal Se earlier drew wide attention as a promising electro-optic material for infrared wavelengths, in particular, for 10.6 μm [1-4]. However, the Se crystals obtained heretofore by various growth techniques developed to date have a very low transmission in the infrared, owing largely to the small-angle grain boundaries unavoidably existing in the crystals. This property also makes it difficult to apply an electric field uniformly over the entire crystals [5-8] and prevents Se from being an efficient electro-optic modulator material in the infrared in spite of its high electro-optic coefficient.

On the other hand, amorphous Se has a low absorption as shown in Fig.5.1-1 ($0.1\ cm^{-1}$ at 10.6 μm) in addition to relatively large refractive index (2.421 at 10.6 μm) [9], and these properties suggest that amorphous Se should be an effective acousto-optic material in the infrared region. Based on this expectation, amorphous Se is taken up in this chapter and its acousto-optic properties at 10.6 μm

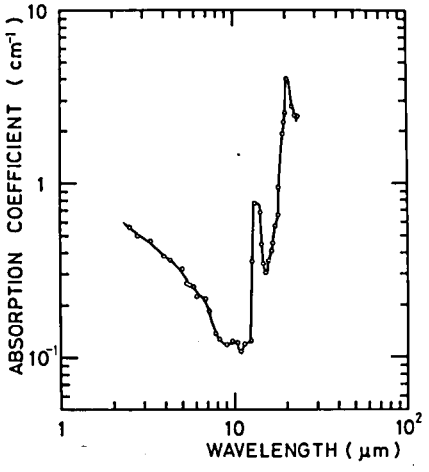

Fig.5.1-1 Wavelength dependence of the optical absorption coefficient of amorphous Se in the vicininty of 10.6 μm.

are examined in detail.

The amorphous samples measured in the experiments were prepared in vacuum-sealed quartz tubes using Se of 99.999-% purity. After these tubes were maintained in a furnace above 500°C for several days, they were quenched by quickly dropping them into ice water or by exposing them to room air. No evidence of crystallization was observed by x-ray inspections.

5.2 Experimental Results

5.2.A *Acoustic properties*

The acoustic properties of amorphous Se were measured prior to the acousto-optic measurements which are described in Sec.5.2.B below. Acoustic velocities and their variation with temperature T were determined by the pulse-echo method developed by McSkimin [10]. The samples were 2- to 3-mm thick and the two large parallel faces were ground and polished to be optically flat. Acoustic transducers of quartz and $LiNbO_3$ with various fundamental frequencies ranging from 10 to 20 MHz were bonded to the optically polished sample faces with phenyl salicylate or epoxy resin. Figures 5.2-1 (a) and (b)

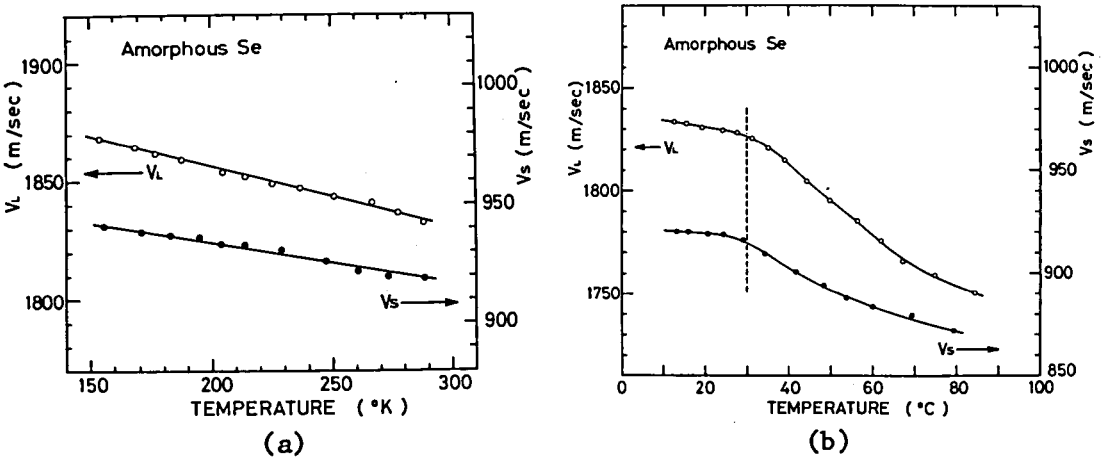

Fig.5.2-1 Variation of acoustic velocities in amorphous Se with temperature.

represent the variation of acoustic velocities in the temperature range from -120 to 90°C, where v_L and v_S denote the longitudinal and shear velocities. An abrupt change in the temperature dependence was observed at about T = 30°C, which is approximately corresponding to the glass transition temperature T_g of Se. T_g is defined as the range of temperature over which the transition between supercooled liquid and glass phase takes place [11]. For amorphous Se, it is known that 25°C < T_g < 35°C [11]. In the temperature range below T_g, both v_L and v_S show linear temperature dependences and decrease with increase in T. From these measurements v_L, v_S, and their temperature coefficients at room temperature were determined as 1.83×10^5

Table 5.1 Acoustic velocities in amorphous Se and their temperature coefficients at room temperature.

v_L	v_S	$\frac{1}{v_L}\frac{\partial v_L}{\partial T}$	$\frac{1}{v_S}\frac{\partial v_S}{\partial T}$
1.83×10^5 cm/sec	0.92×10^5 cm/sec	-140 ppm/°C	-180 ppm/°C

L and S respectively denote longitudinal and shear waves.

Table 5.2 Elastic constants of amorphous Se (in the unit of 10^{11} dyne/cm^2) at room temperature.

	this work	Graham et al. [a]	Vedam et al. [b]
c_{11}	1.43	1.443	1.436
c_{12}	0.707	0.690	0.698

$\rho = 4.27$ g/cm^3. [a] Ref.[12]. [b] Ref.[13].

cm/sec, 0.920×10^5 cm/sec, -140 ppm/°C, and -180 ppm/°C, respectively, as listed in Table 5.1. These relatively slow velocities suggest that amorphous Se may possess large figures of merit. Table 5.2 tabulates the values of the two independent elements of the elastic tensor, c_{11} and c_{12}, at room temperature along with those reported by Graham et al [12] and by Vedam et al [13]. These values were obtained from the relations

$$c_{11} = \rho\, v_L^2 \quad \text{and} \quad (c_{11} - c_{12})/2 = \rho\, v_S^2 , \tag{5.2-1}$$

where the density ρ was determined as 4.27 g/cm^3 by measuring the weight and sizes of a parallelepiped sample.

The temperature and frequency dependences of acoustic attenuation were also measured by the pulse-echo method. The intensity of a plane acoustic wave in a lossy medium is expressed by

$$A(x) = A(0) \exp(-\alpha x), \tag{5.2-2}$$

where x is the propagation distance and α is the acoustic attenuation constant. From Eq.(5.2-2), the intensity of the n-th echo A_n can be written

$$A_n = A_1 \exp[-2(n-1)\,\alpha L], \tag{5.2-3}$$

where A_1 is the intensity of the first echo, L is the thickness of the sample, and the acoustic reflectivity at each sample end has been assumed to be unity as a realistic approximation. Therefore,

the acoustic attenuation constant α can be determined by measuring the exponential decay of the acoustic echo train. Figure 5.2-2 is an example of the typical echo trains which show approximately exponential decay. The thus-obtained α in amorphous Se at room temperature is plotted in Fig.5.2-3 as a function of acoustic frequency for longitudinal (Fig.5.2-3 (a)) and shear (Fig.5.2-3 (b)) waves, from which it is found that α measured in dB/cm obeys

$$\alpha = 1.22\, f^{0.73} \qquad \text{(longitudinal waves)} \qquad (5.2\text{-}4)$$

and

$$\alpha = 2.12\, f^{0.81} \qquad \text{(shear waves)} \qquad (5.2\text{-}5)$$

where f is measured in MHz.

Figure 5.2-4 shows the temperature dependence of α for the longitudinal acoustic frequency of 12 MHz. As we have seen in the temperature dependence of the acoustic velocities, α also shows an abrupt change at about 300°K, corresponding to the glass transition, and rapidly increases with T above this temperature. Consequently, in order to use amorphous Se as an acousto-optic medium, it may be necessary to maintain the temperature below this glass transition temperature so as to assure stable operation and to avoid an increase in the acoustic loss, and this will be a serious drawback in its acousto-optic applications. Improvement of this difficulty by alloying with other elements will be discussed in Sec.5.2.C.

5.2.B *Figures of merit and photoelastic constants*

The determination of figures of merit was carried out by the Dixon-Cohen method [14-17] in the same way as has been described in Cap.2 for Te. A fused quartz buffer rod was used as a standard reference material (see Fig.2.2-2), on which a 36°-rotated y-cut

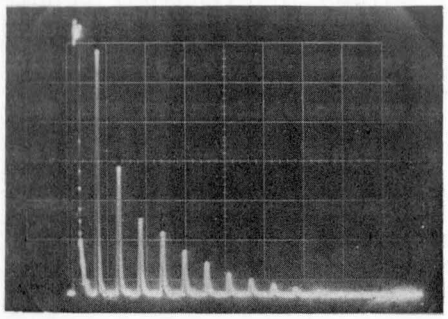

Fig.5.2-2 An acoustic echo train which shows approximately exponential decay.

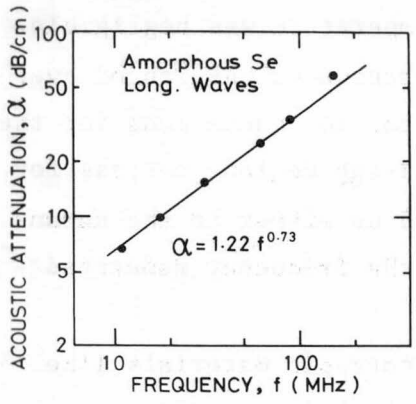

(a)

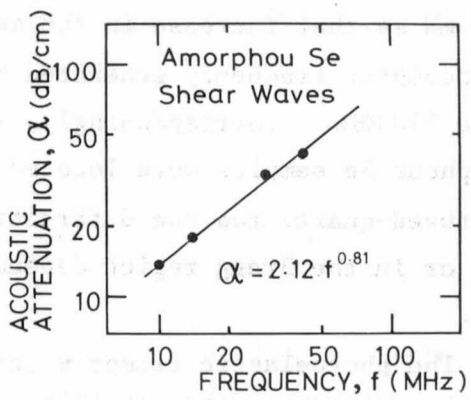

(b)

Fig.5.2-3 Acoustic loss in amorphous Se as a function of acoustic frequency at room temperature for longitudnal wave (a) and shear wave (b).

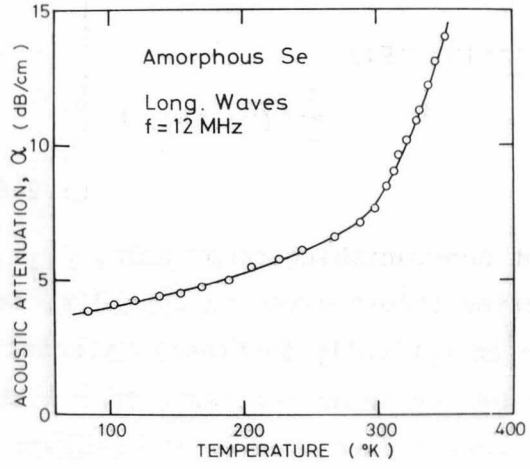

Fig.5.2-4 Acoustic loss in amorphous Se as a function of temperature for 12-MHz longitudinal wave.

$LiNbO_3$ transducer was bonded to generate pulsed longitudinal acoustic waves. The amorphous Se samples were bonded to the buffer rod on the face opposite to the transducer with phenyl salicylate or epoxy resin bond. The light sources were a 0.6328-μm He-Ne laser for the fused quartz and a 10.6-μm *cw* CO_2 laser for the sample, respectively. The incident linearly polarized CO_2 laser beam had a spot diameter of about 1 mm at the sample face. Care was taken to suppress the incident optical power to be much less than a few hundred mW so that increase in the sample temperature was negligible. The acoustic frequency generated by the transducer was ranged over 15 to 170 MHz. Correspondingly, the diffraction conditions for the smorphous Se samples were located in the Bragg region, whereas for the fused-quartz rod the diffraction could be either in the Raman-Nath or in the Bragg region depending on the frequency generated [18].

The photoelastic tensor matrix for isotropic materials like amorphous Se is written as [19]

$$\begin{vmatrix} p_{11} & p_{12} & p_{12} & 0 & 0 & 0 \\ p_{12} & p_{11} & p_{12} & 0 & 0 & 0 \\ p_{12} & p_{12} & p_{11} & 0 & 0 & 0 \\ 0 & 0 & 0 & \frac{1}{2}(p_{11}-p_{12}) & 0 & 0 \\ 0 & 0 & 0 & 0 & \frac{1}{2}(p_{11}-p_{12}) & 0 \\ 0 & 0 & 0 & 0 & 0 & \frac{1}{2}(p_{11}-p_{12}) \end{vmatrix}, \tag{5.2-6}$$

which contains only two independent non-vanishing components, p_{11} and p_{12}. According to the diffraction theory given in Appendix, for a longitudinal wave propagating in an optically isotropic material, M_{11} and hence p_{11} can be measured by using an incident light with polarization parallel to the displacement direction of the acoustic

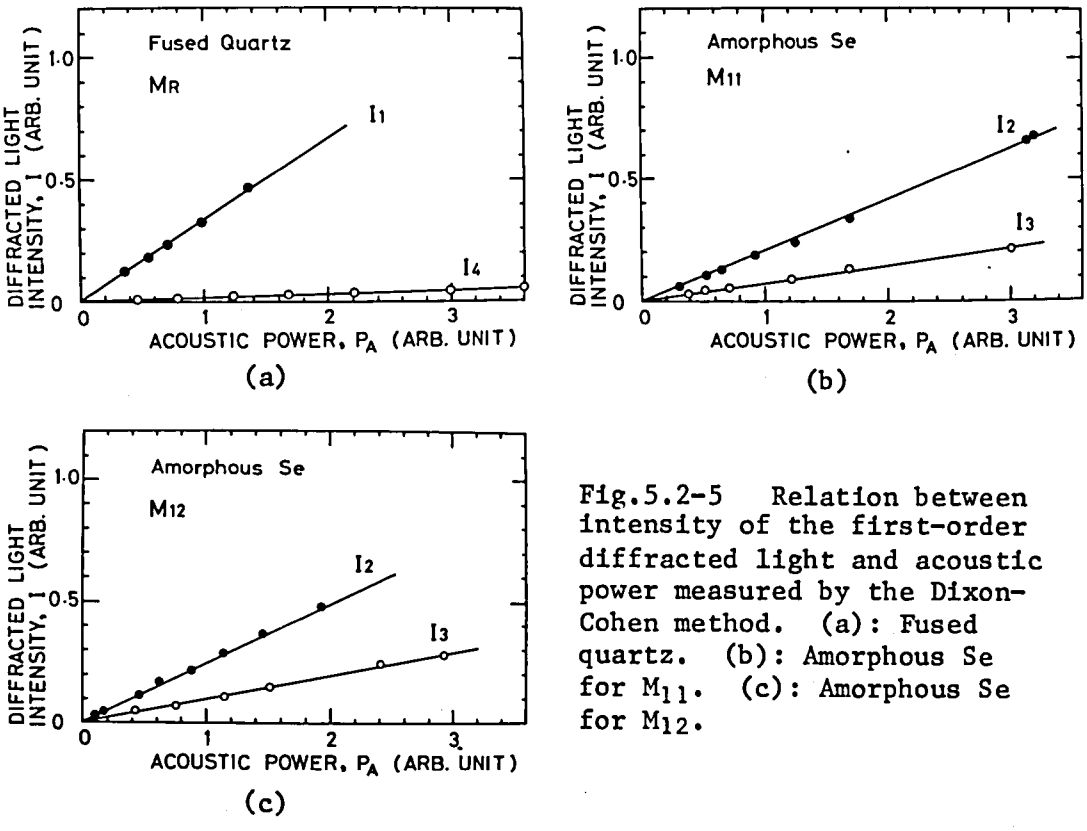

Fig.5.2-5 Relation between intensity of the first-order diffracted light and acoustic power measured by the Dixon-Cohen method. (a): Fused quartz. (b): Amorphous Se for M_{11}. (c): Amorphous Se for M_{12}.

wave. On the other hand, M_{12} and p_{12} can be determined from the measurements employing an incident light with polarization perpendicular to the elastic displacement. The plots of the results obtained in this way from the Dixon-Cohen measurements are shown in Fig.5.2-5 (a), (b), and (c), where I_2 and I_3 are the relative first-order diffracted light intensities for amorphous Se due to the acoustic pulse outgoing from the transducer and due to the pulse reflected from the free end of the amorphous Se, respectively, and I_1 and I_4 are the relative first-order diffracted intensities for the fused quartz due to the outgoing pulse and due to the reflected pulse, respectively. The figures of merit obtained from a similar procedure to that described in Sec.2.3 are tabulated in Table 5.3. The values determined by Schneider and Vedam for the wavelength of 1.15 μm, which have been the only measurements made to date as to the photoelastic properties

Table 5.3 Acousto-optic properties of amorphous Se.

Wave-length (μm)	Refractive index	Acoustic wave polarization and direction	Acoustic velocity (10^5 cm/sec)	Optical wave polarization and direction	Figures of merit M (10^{-18} sec^3/g)	M' (10^{-7} cm^2 sec/g)	M'' (10^{-12} cm sec^2/g)
1.15	2.4969	long.	1.83	//	1100	920	501
				⊥	1210	1010	552
10.6	2.421	long.	1.83	//	981	795	434
				⊥	1080	877	479

$\rho = 4.27$ g/cm^3, $M = n^6 p^2/\rho v^3$, $M' = n^7 p^2/\rho v$, and $M'' = n^7 p^2/\rho v^2$.

Table 5.4 Photoelastic constants of amorphous Se.

Wavelength (μm)	p_{11}	p_{12}
1.15	0.345	0.362
10.6	0.357	0.375

of amorphous Se, are also given in Table 5.3 [20]. Their results were obtained by the conventional static method in which the change of the refractive index was measured as a function of applied static pressure. It should be noted that amorphous Se has fairly large figures of merit at 10.6 μm as well as 1.15 μm and is a very attractive material for acousto-optic applications at wide infrared wavelength range since as we have seen in Fig.5.1-1 the transparent region of this material spans from about 1 to 20 μm. Table 5.4 lists the photoelastic constants deduced from the above-determined figures of merit employing Eq.(2.2-4) together with the values obtained by Schneider and Vedam at 1.15 μm [20]. The values for the refractive indices used in the calculations were those determined by Koehler et al [9].

Schneider and Vedam concluded in their literature that the photoelastic constants obtained at 1.15 μm were enhanced compared with the values obtained at longer wavelengths because this experimental wavelength was located near the absorption edge. Contrary to their conclusion, however, the present results reveal that the values at 10.6 μm are a little larger than those at 1.15 μm for both p_{11} and p_{12} and no enhancement can be observed at the shorter wavelength. This wavelength dependence is also supported by the pressure dependence of the optical reflectivity of amorphous Se measured by Kastner et al [21]. Figure 5.2-6 shows the fractional change of reflectivity

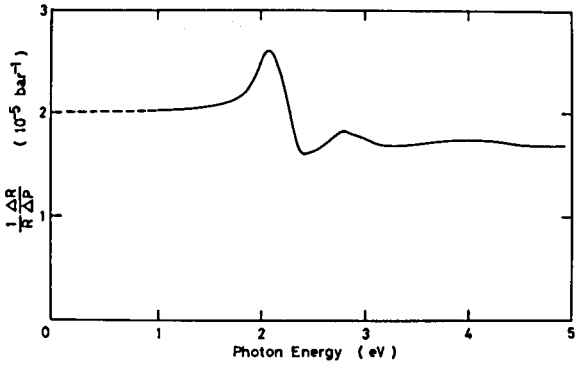

Fig.5.2-6 Fractional reflectivity change per unit hydrostatic pressure applied to amorphous Se as a function of photon energy (after Kastner et al [21]).

per unit hydrostatic pressure $\Delta R/R\,\Delta P$ measured by Kastner et al at room temperature as a function of photon energy. Extrapolating the plot in Fig.5.2-6, we obtain

$$\frac{1}{R}\frac{\Delta R}{\Delta P} = 2.0 \times 10^{-5}\ \text{bar}^{-1}$$

$$= 2.0 \times 10^{-11}\ \text{cm}^2/\text{dyne} \qquad (5.2\text{-}7)$$

for both 1.15 and 10.6 μm. Since the relation

$$R = (n-1)^2/(n+1)^2 \qquad (5.2\text{-}8)$$

holds between the reflectivity and refractive index of dielectric materials in a transparent region, we have

$$\Delta R = \frac{4(n-1)}{(n+1)^3}\Delta n\ . \qquad (5.2\text{-}9)$$

In isotropic solids under hydrostatic pressure, the relation between the increment of the hydrostatic pressure, ΔP, and the induced longitudinal strain S_1 is given by

$$\Delta P = -(c_{11}+2c_{12})\,S_1\ , \qquad (5.2\text{-}10)$$

where c_{11} and c_{12} are the elastic constants. Combining Eqs.(5.2-6) and (5.2-10), we obtain the change of refractive index as

$$\Delta n = -\frac{1}{2}n^3\,(p_{11}+2p_{12})\,S_1\ . \qquad (5.2\text{-}11)$$

Equations (5.2-9), (5.2-10), and (5.2-11) then yield

$$p_{11}+2p_{12} = \frac{(n+1)(n-1)}{2n^3}\,(c_{11}+2c_{12})\left(\frac{1}{R}\frac{\Delta R}{\Delta P}\right)\ . \qquad (5.2\text{-}12)$$

Substituting $\Delta R/R\,\Delta P = 2.0 \times 10^{-11}$ cm^2/dyne and the values for the refractive indices into Eq.(5.2-12), we obtain $p_{11} + 2p_{12} = 0.952$ at 1.15 μm and $p_{11} + 2p_{12} = 0.967$ at 10.6 μm. On the other hand, the experimentally determined values are $p_{11} + 2p_{12} = 1.07$ at 1.15 μm and $p_{11} + 2p_{12} = 1.11$ at 10.6 μm. Thus, these two kinds of values obtained in the different ways show good agreement with each other and support the experimental fact that the photoelastic constants at 10.6 μm are larger than those at 1.15 μm.

The phenomenological photoelastic theory developed by Wemple and DiDomenico [22-25] may be helpful to explain this wavelength dependence. Their theory starts from the well-known Sellmeier dispersion formula

$$n^2 - 1 = \sum_i F_i/(E_i^2 - E^2) \,, \qquad (5.2\text{-}13)$$

where E is the photon energy, n is the refractive index, and F_i and E_i are the strength and the position of the i-th oscillator, respectively. In the case of amorphous Se, the summation of the right-hand side of Eq.(5.2-13) can be approximated only by one term. This is shown in Fig.5.2-7. The parameters obtained by fitting Eq.(5.2-13) to the refractive index data given by Koehler et al [9] are $F_0 = 75.1\ (\text{eV})^2$ and $E_0 = 3.93$ eV, and it is found that the position of E_0 approximately corresponds to the transition from the lone-pair p band

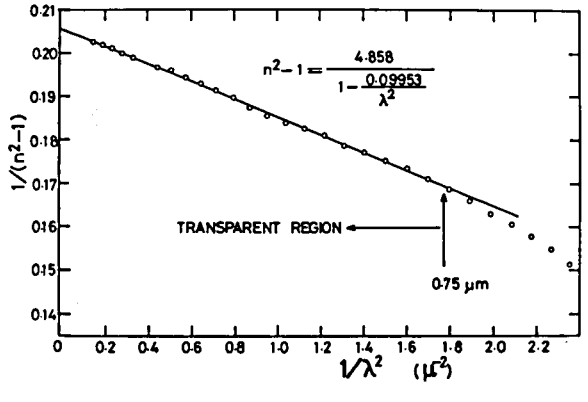

Fig.5.2-7 The Sellmeier dispersion relation observed in the refractive index of amorphous Se. The data for the refractive index were those reported by Koehler et al [9].

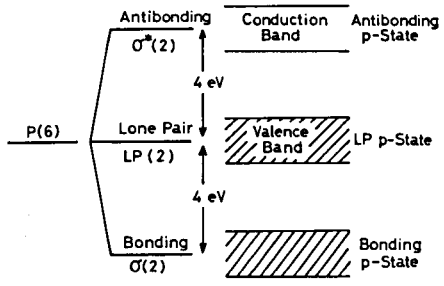

Fig.5.2-8 Schematic band-structure diagram for amorphous Se.

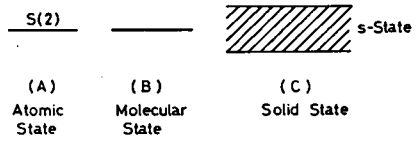

(the valence band of amorphous Se) to the antibonding p band (the conduction band) [26]. Figure 5.2-8 shows a schematic band-structure diagram for amorphous Se originally proposed by Kastner [26]. It is therefore understood that the refractive index in the longer wavelength region is mainly determined by this transition.

Differentiating Eq.(5.2-13) with respect to the strain, Wemple and DiDomenico derived the following equations to describe the photoelasticity of dielectrics [22-25]:

$$\frac{p_{ij}}{(1-1/n^2)^2} = \frac{2}{E_d} D_{ij}\left(1+K_{ij}\,(1-\frac{E^2}{{E_0}^2})\right), \qquad (5.2\text{-}14)$$

$$E_d = F_0/E_0 , \qquad (5.2\text{-}15)$$

and

$$K_{ij} = -\frac{1}{2}\left(\frac{\Delta F_0/F_0}{\Delta E_0/E_0}\right), \qquad (5.2\text{-}16)$$

where no summation over repeated subscripts is implied. p_{ij} is a

photoelastic constant, D_{ij} is a deformation potential, and K_{ij} describes interband-transition strength change induced by the strain. Substituting the experimental results given in Tables 5.3 and 5.4 into Eq.(5.2-14), we obtain D_{ij} and K_{ij} as follows: For p_{11},

$$D_{11} = 1.20 \text{ eV}, \quad K_{11} = 3.13, \tag{5.2-17}$$

and for p_{12},

$$D_{12} = 1.15 \text{ eV}, \quad K_{12} = 3.52. \tag{5.2-18}$$

Hence it can be concluded that the photoelasticity of amorphous Se and its wavelength dependence are mainly originated from the strain-induced change of the interband transition located approximately at 3.93 eV. The amount of the change is determined by the parameters given by Eqs.(5.2-17) and (5.2-18)

5.2.C *Improvement of acousto-optic properties of amorphous Se by alloying*

From an applicational point of view, amorphous Se possesses a few practical drawbacks as an acousto-optic medium as follows. (1) Low melting point : The melting point of this material is as low as about 220°C, so that the optical absorption, though small, may probably cause material damage under high incident power. Contrary to this anticipation, we however did not observe any evidence of damage even when the incident *cw* optical power at 10.6 μm was as high as several watts, and therefore we may conclude that this low melting point will not become a very serious problem as long as a moderate optical power is used. (2) Low glass transition temperature: As we have seen, T_g of amorphous Se is located in the range between about 25 and 35°C [11], so that the material is both optically and electrically unstable above this temperature. As one of the ways to over-

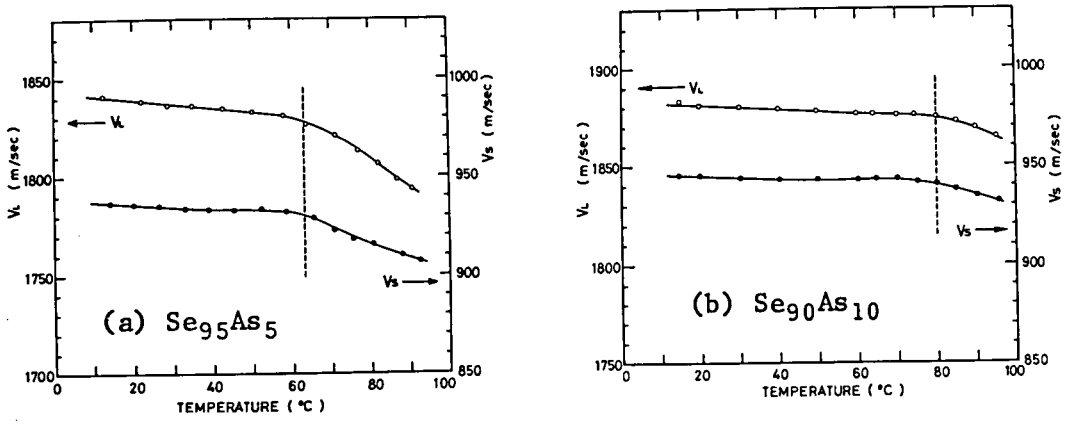

Fig.5.2-9 Variation of acoustic velocities of $Se_{95}As_5$ (a) and $Se_{90}As_{10}$ (b) with temperature.

come these problems, alloying with several percents of other elemental materials was attempted. The element taken up here is arsenic (As) because it has been discovered that the addition of small amount of As to some chalcogenide glasses results in strikingly different acoustic behavior [27]. The examined compositions are $Se_{95}As_5$ and $Se_{90}As_{10}$. These materials were prepared by direct fusion of Se and As in vacuum-sealed quartz tubes. The v *vs* T curves for these amorphous materials are shown in Figs.5.2-9 (a) and (b). The temperature which is considered as corresponding to T_g shows significant shift toward higher temperature region compared with the results obtained for pure amorphous Se (Fig.5.2-1). T_g for $Se_{95}As_5$ and $Se_{90}As_{10}$ is respectively 63 and 80°C and satisfactorily higher than room temperature. Table 5.5 shows the temperature coefficients

Table 5.5 Temperature coefficients of velocity at room temperature.

composition	$\frac{1}{v_L}\frac{\partial v_L}{\partial T}$	$\frac{1}{v_S}\frac{\partial v_S}{\partial T}$
$Se_{95}As_5$	-110 ppm/°C	-85 ppm/°C
$Se_{90}As_{10}$	-53	-75

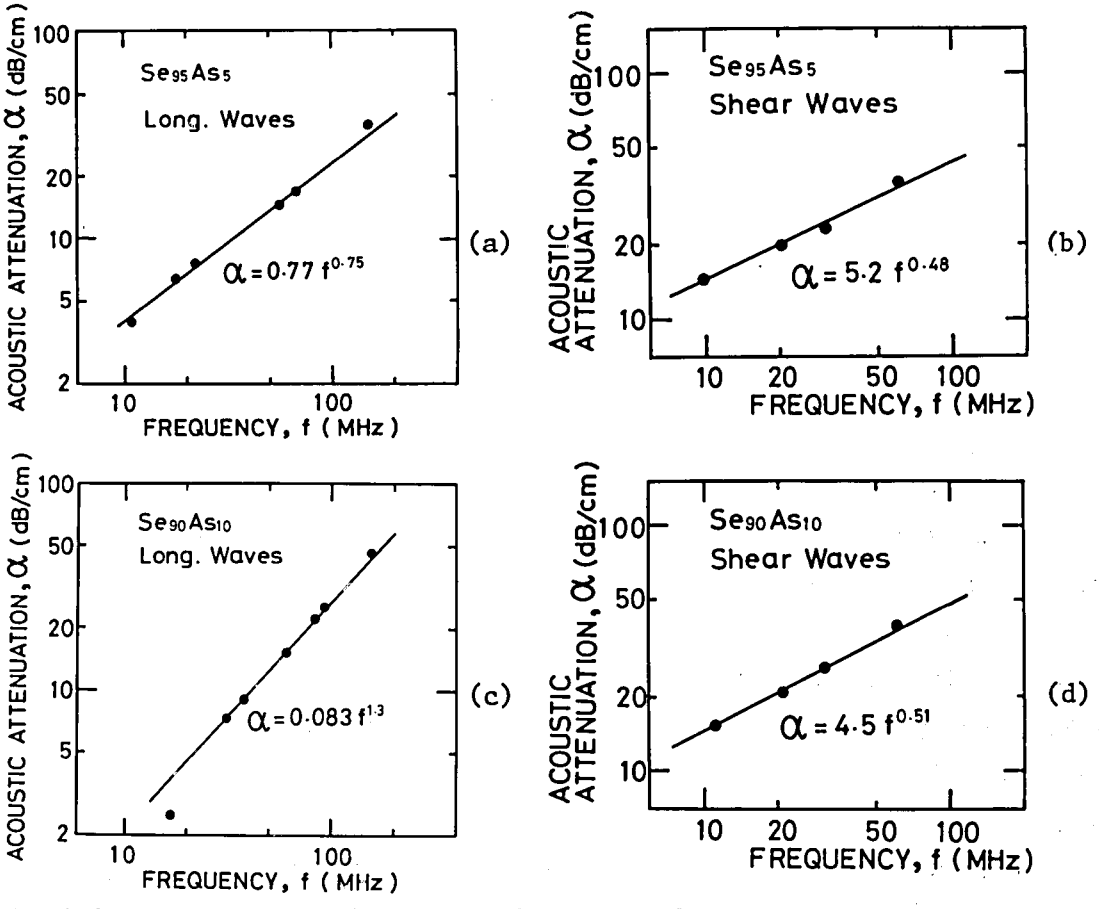

Fig.5.2-10 Acoustic loss as a function of acoustic frequency at room temperature. (a) and (b) are respectively for longitudinal and shear waves is $Se_{95}As_5$, and (c) and (d) are respectively for longitudinal and shear waves is $Se_{90}As_{10}$.

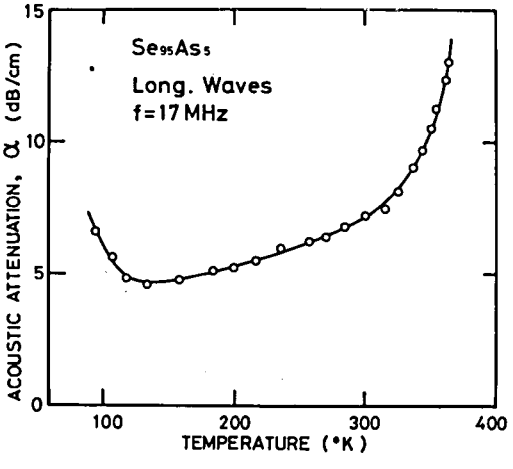

Fig.5.2-11 Variation of acoustic loss in amorphous $Se_{95}As_5$ with temperature.

Table 5.6 Figures of merit in amorphous $Se_{95}As_5$ and $Se_{90}As_{10}$.

composition	M_{11}	M_{12}
$Se_{95}As_5$	1100×10^{-18} sec^3/g	1160×10^{-18} sec^3/g
$Se_{90}As_{10}$	954	963

$M_{ij} = n^6 p_{ij}^2 / \rho v^3$.

of velocity at room temperature, which suggests that both of these materials possess smaller temperature coefficients than those of pure amorphous Se (Table 5.1) and therefore are more stable at room temperature.

Figures 5.2-10 (a), (b), (c), and (d) show the acoustic attenuation constant α versus frequency relations for these materials. α for longitudinal waves propagating in $Se_{95}As_5$ is shown in Fig.5.2-11 as a function of temperature. Table 5.6 lists the figures of merit determined by the Dixon-Cohen method [14,15] for $Se_{95}As_5$ and $Se_{90}As_{10}$. It is noted that these values are all comparable to or even larger than those of pure Se (see Table 5.3).

From the results described above, it is concluded that the addition of small amount of As to Se results in a more preferable acousto-optic behavior than pure amorphous Se.

5.3 Concluding Remarks

It is found that amorphous Se possesses large figures of merit at 10.6 μm which are almost comparable to those of Te (see Figs.2.6-2 and 2.6-3). The wavelength dependence of the photoelastic constans suggests that the photoelasticity in amorphous Se can be attributed to the interband transition from the lone-pair p band to the anti-bonding p band. In spite of the large figures of merit, amorphous Se is not very satisfactory as an acousto-optic medium since the glass

transition temperature of about 30°C makes the material very unstable at room temperature. It is however found that the addition of several percents of As significantly improves the acousto-optic properties.

References

[1] M. C. Teich and T. Kaplan, IEEE J. Quantum Electron. QE-2 (1966) 702.

[2] E. H. Turner, I. P. Kaminow, and E. D. Kolb, IEEE J. Quantum Electron. QE-4 (1968) 234.

[3] J. E. Adams and W. Haas, in *The Physics of Selenium and Tellurium*, edited by W. C. Cooper (Pergamon, London, 1969) p.293.

[4] S. Fukuda, T. Shiosaki, A. Kawabata, Jpn. J. Appl. Phys. 12 (1973) 1944.

[5] J. Stuke, in *Recent Advances in Selenium Physics*, edited by H. Gobrecht (Pergamon, London, 1965) p.35.

[6] T. Salo, T. Stubb, and E. Suosara, in *The Physics of Selenium and Tellueium*, edited by W. C. Cooper (Pergamon, London, 1969) p.335.

[7] S. Hemilä, Acta Polytech. Scand. Physics incl. Nucleonics 69 (Helsinki, 1969).

[8] T. Shiosaki, S. Fukuda, and A. Kawabata, Jpn. J. Appl. Phys. 10 (1971) 1487; ibid, 12 (1973) 252.

[9] W. F. Koehler, F. K. Odencrantz, and W. C. White, J. Opt. Soc. Am. 49 (1959) 109.

[10] H. J. McSkimin, J. Acoust. Soc. Am. 37 (1965) 864.

[11] A. E. Owen, in *Electronic and Structural Properties of Amorphous Semiconductors*, edited by P. G. Le Comber and J. Mort (Academic, New York, 1973) p.181.

[12] L. J. Graham and R. Chang, J. Appl. Phys. 36 (1965) 2983.

[13] K. Vedam, D. L. Miller, and R. Roy, J. Appl. Phys. 37 (1966) 3432.

[14] R. W. Dixon and M. G. Cohen, Appl. Phys. Letters 8 (1966) 205.

[15] R. W. Dixon and A. N. Chester, Appl. Phys. Letters 9 (1966) 190.

[16] S. Fukuda, T. Shiosaki, and A. Kawabata, Jpn. J. Appl. Phys. 15 (1976) 927; J. Appl. Phys. 50 (1979) 3899.

[17] S. Fukuda, T. Wada, T. Shiosaki, and A. Kawabata, Jpn. J. Appl. Phys. 16 (1977) 659.

[18] N. Uchida and N. Niizeki, Proc. IEEE 61 (1973) 1073.

[19] J. W. Tucker and V. W. Rampton, *Microwave Ultrasonics in Solid State Physics* (North-Holland, Amsterdam, 1972) p.364

[20] W. C. Schneider and K. Vedam, J. Opt. Soc. Am. 60 (1970) 800.

[21] M. Kastner and R. R. Forberg, Phys. Rev. Letters 36 (1976) 740.

[22] M. DiDomenico Jr. and S. H. Wemple, J. Appl. Phys. 40 (1969) 720.

[23] S. H. Wemple and M. DiDomenico Jr., Phys. Rev. Letters 23 (1969) 1156; Phys. Rev. B 1 (1970) 193.

[24] S. H. Wemple, Phys. Rev. B 7 (1973) 3767.

[25] S. H. Wemple and M. DiDomenico Jr., in *Applied Solid State Science*, edited by R. Wolf (Academic, New York, 1972) Vol.3, p.263.

[26] M. Kastner, Phys. Rev. Letters, 28 (1972) 355.

[27] J. T. Krause, C. R. Kurkjian, D. A. Pinnow, and E. A. Sigety, Appl. Phys. Letters 17 (1970) 367.

CHAPTER 6

Au-CLAD AMORPHOUS Se OPTICAL WAVEGUIDES AND PHOTOELASTIC MODULATOR

6.1 Introduction

Recent experimental and theoretical efforts to develop efficient optical waveguides and integrated optical elements have been made mostly in visible or near infrared region. In such circumstances, it is especially necessary to pay attention to inherent superior feasibilities of the 10.6-μm radiation of a CO_2 laser. Except GaAs, however, we have not yet obtained materials practically applicable to waveguides at 10.6 μm [1-4].

In this chapter, the first experimental observation of waveguiding phenomena in amorphous Se at 10.6 μm and its application to a photoelastic modulator are described. The optical absorption of this material is relatively low in the infrared region from about 1 to 20 μm as shown in Fig.5.1-1. The absoption at 10.6 μm is about $0.1\,cm^{-1}$ and the lowest in the measured wavelength range. This value is considered to be low enough for the application to optical waveguides. Besides, it has been revealed in Chap.5 that amorphous Se possesses large acousto-optic figures of merit at 10.6 μm and is attractive for the device application utilizing the interaction between surface acoustic waves and guided optical waves [5].

In general, dielectric optical waveguides are constructed making use of a guiding layer of high refractive index and a substrate of low refractive index. In the infrared region, however, it is not easy to find a proper combination of the materials of low absorption

since at present the materials available in the infrared region are not so many as in the visible. Hence, the structure of one-sided metal cladding is adopted for the present purpose since in this structure any choice of the substrate material does not affect the properties of the guide [6,7].

6.2 Experimental Results

6.2.A *Au-clad amorphous Se waveguides*

Figure 6.2-1 illustrates the structure of the sample. The material used as a cladding metal was an evaporated Au film. The Cr layer was sandwiched between the Au layer and the glass substrate to obtain strong adhesion. Then, the Se of 99.999 % purity was deposited at room temperature in the vacuum of several 10^{-6} Torr. It was confirmed by x-ray investigations that the above-prepared Se film was amorphous. The ends of the sample were mechanically polished to obtain flat parallel faces normal to the optical propagation direction The refractive indices of amorphous Se and Au at 10.6 μm are 2.421 and 17.23 - j·56.00, respectively [9].

Waveguiding experiments were performed with the setup shown in Fig.6.2-2. A linearly polarized *cw* CO_2 laser beam which was carefully adjusted to operate in the fundamental Gaussian TEM_{00} mode was used in the waveguiding experiments. Coupling between the incident beam and the guided modes was accomplished by focusing the incident

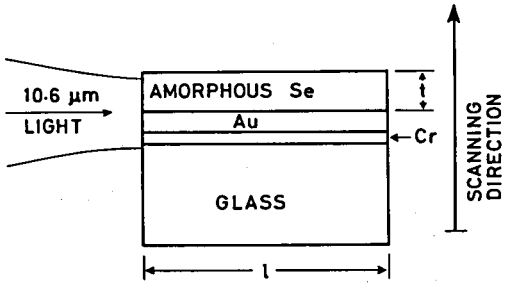

Fig.6.2-1 Structure of the waveguide.

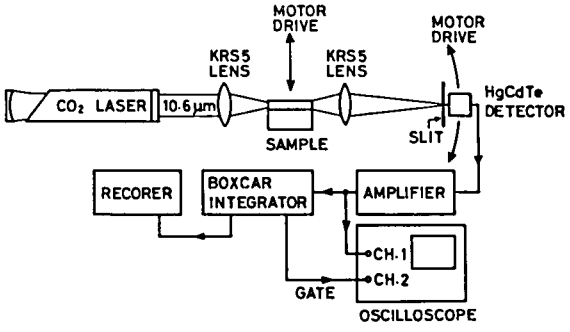

Fig.6.2-2 Experimental setup.

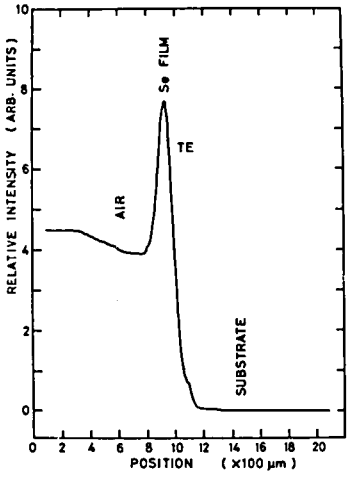

Fig.6.2-3 Variation of the transmitted optical intensity when the sample was translated across the focused laser beam. The direction of the sample translation is indicated by an arrow in Fig.6.2-1. The thickness and length of the Se layer were 11.0 μm and 4.22 mm, respectively.

beam onto the sample input face with a KRS5 lens. To identify the confined modes, the far-field intensity pattern of the transmitted light was measured by mechanically rotating the HgCdTe infrared detector about the sample. Figure 6.2-3 shows the transmitted intensity pattern which was obtained by mechanically translating the sample across the focused laser beam. The scanning direction is shown in Fig.6.2-1 by an arrow. The spatial resolution was limited by the about 90-μm half-power spot-diameter of the laser beam. The Se thickness of the sample in Fig.6.2-3 was 11.0 μm and the length in the propagation direction was 4.22 mm. The incident beam was polarized so as to excite TE modes. The strong sharp peak was observed when the incident beam illuminated the Se input face, suggesting the occurrence of optical confinement in the Se layer. When the beam illuminated the glass substrate, no transmission was observed because

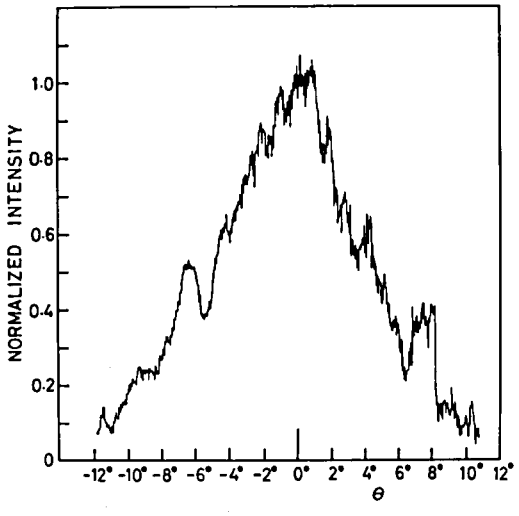

Fig.6.2-4 Angular distribution of the far-field intensity pattern. The thickness and the length of the Se film are 44 μm and 5.4 mm, respectively.

the glass was not transparent for the 10.6-μm radiation.

Figure 6.2-4 shows the angular distribution of the far-field intensity pattern obtained for a Se film of 44-μm thickness. The shape of the pattern is approximately symmetrical with respect to the position of 0°. The dominant structure is a single broad lobe centered at 0°, which suggests that the fundamental TE_0 mode is most dominantly confined. The pattern shows the width of about 10° at the half-power points. Now, it is possible to estimate the field distribution in the guide layer by assuming that the field distribution in the far-field is Gaussian to good approximation. The diffraction-spread angle of about 10° at the half-power points in the far-field then corresponds to a field distribution with the full-width of 45.5 μm at the $1/e^2$-power points at the output face of the Se layer [12], which is in good agreement with the film thickness of 44 μm. Hence, it can be concluded that the most dominant mode confined in the film is the TE_0 mode. This is the first experimental observation of the waveguiding phenomena in the film of amorphous Se at 10.6 μm. In the experiments to excite TE modes, the TE_0 mode was always found to be more or less dominant.

Confinement of TM modes was also attempted. However, no evi-

dence of the confinement was observed. It is concluded that this is mainly due to the large attenuation of TM modes inherent of metal-clad optical guides. The theoretical calculation of attenuation constants is shown in Fig.6.2-5 as a function of the thickness of the amorphous Se layer [8]. It is assumed in this calculation that the Au cladding is much thicker than the penetration depth (543 Å). The attenuation of the TE_0 mode is the smallest and it increases with mode order. The attenuation of the TM_0 mode is larger than that of the TE_0 by almost three orders of magnitude. The broken line in Fig. 6.2-5 denotes the limit corresponding to the inherently existing bulk absorption as shown in Fig.5.1-1.

6.2.B *Photoelastic modulator*

As we have seen in Chap.5, amorphous Se has large acousto-optic figures of merit at 10.6 μm as well as at 1.15 μm [3,10] and is an attractive material from an applicational point of view. One of the

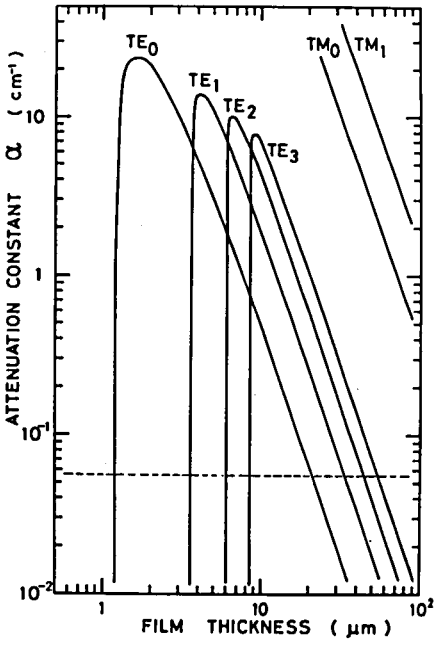

Fig.6.2-5 The attenuation constant of the Au-clad amorphous Se waveguide as a function of the Se thickness. The surface plasma mode has been neglected in this calculation. The broken line denotes the limit originated from the bulk absorption given in Fig.5.1-1.

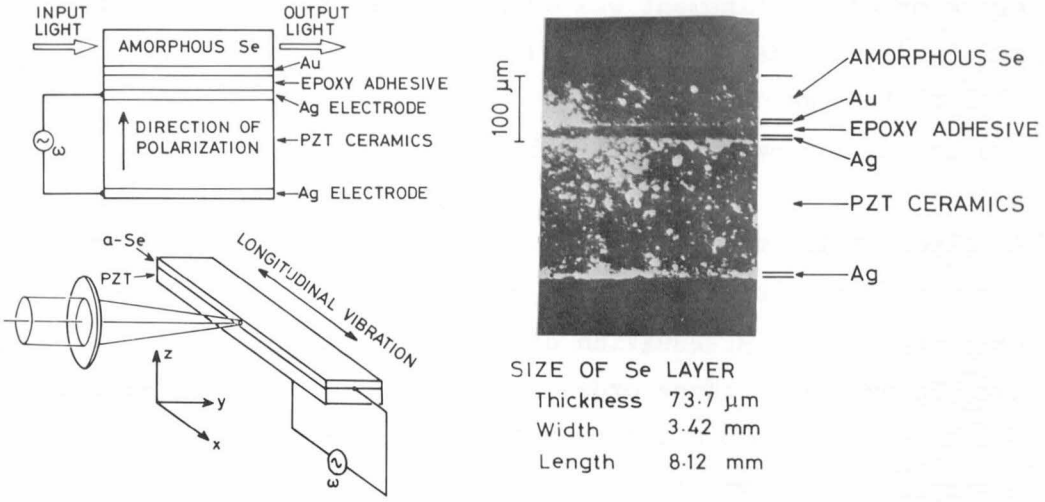

Fig.6.2-6 Schematic illustration of photoelastic modulator (a) and photograph of its cross section (b).

merits of the metal-clad Se waveguides is that this structure enables us to construct guided acousto-optic devices on piezoelectric substrates utilizing a large acousto-optic effect in amorphous Se. Since most of piezoelectric materials show considerable optical absorption at 10.6 μm, they cannot be used as the substrate of ordinary dielectric guide structures. This difficulty can be avoided by forming a metal-cladding layer between the piezoelectric substrate and the amorphous Se layer.

As preliminary experiments, a photoelastic modulator utilizing a piezoelectric resonance of the composite resonator as shown in Fig. 6.2-6 was constructed. PZT piezoelectric ceramics was used as a substrate to excite a mechanical vibration, onto which the amorphous Se layer with Au cladding was bonded with epoxy adhesive. The resonance excited in the experiments was a fundamental length-expanding mode or a longitudinal vibration along the length direction of the thin bar sample. Therefore, if we define the three coordinate axes x, y, z as shown in Fig.6.2-6, the excited mechanical strain is given

by S_{11} under the one dimensional approximation as

$$S_{11} = \frac{1}{2} S_{11}^{0} \sin\frac{\pi x}{L} \exp(j\omega t) + c.c., \qquad (6.2\text{-}1)$$

where ω and L are the frequency of the mechanical vibration and the length of the sample, respectively. The incident light was focused onto the side face so as to excite TE modes. Therefore, upon emerging from the guide output face, the transmitted light will acquire the relative phase shift ϕ as

$$\phi = \frac{2\pi}{\lambda_0} n w - \frac{2\pi}{\lambda_0} \Delta n w , \qquad (6.2\text{-}2)$$

$$\Delta n = \frac{1}{2} n^3 p_{11} S_{11} , \qquad (6.2\text{-}3)$$

where n is the effective refractive index without the strain and p_{11} is the photoelastic constant [5]. w is the width of the sample in which direction the incident beam was transmitted.

In order to detect the intensity light modulation due to the photoelastic effect, a Mach-Zehnder type interferometer was constructed as shown in Fig.6.2-7. The incident beam from a CO_2 laser is split into the two branches. As given by Eqs.(6.2-2) and (6.2-3), the light beam on one of the two branches undergoes the phase modulation caused by the photoelastic effect due to the mechanical

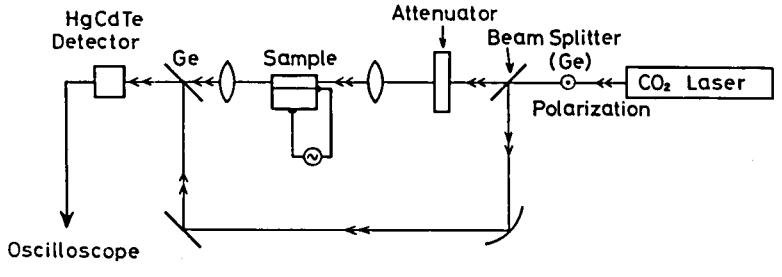

Fig.6.2-7 Schematic illustration of the setup used in the modulation experiments.

strain. The thickness of the Se layer was 74 μm. The length L and the width w were 8.1 mm and 3.4 mm, respectively. The resonance frequency of this sample was 211.2 kHz and was in good agreement with the calculated value of 209.5 kHz. The wave forms of the applied voltage at 211.2 kHz and modulated optical intensity are shown in the photograph in Fig.6.2-9. The solid curve in Fig.6.2-8 shows the electrical admittance of the sample as a function of frequency in the vicinity of the resonance. The amplitude change of the detected light intensity is shown by the broken curve. When either one of the two branches of the interferometer was blocked, the intensity modulation disappeared. This proves that the detected modulation is due to the phase modulation caused by the photoelastic effect. The amplitude of the driving voltage was 22.5 V. According to Fig.6.2-8, the band-width of this modulator is determined to be 5.4 kHz.

Figure 6.2-10 shows the detected light intensity as a function of applied voltage. The half-wave voltage V_π, derived from

$$\pi = \frac{\pi}{\lambda_0} n^3 p_{11} w S_{11} , \qquad (6.2\text{-}4)$$

is found to be 55 V. The extinction of the modulator is 91 %. This imperfect extinction is considered to be due to an unbalanced power splitting of the beam splitter and the additional interference of the air mode which has not been coupled into the guiding layer [13].

6.3 Concluding Remarks

Optical waveguiding phenomena at 10.6 μm have been observed in evaporated amorphous Se films with Au-cladding. The far-field analysis has shown that the fundamental TE_0 mode is most dominantly confined. The results show that amorphous Se can be used to form planar waveguides for the 10.6-μm radiation of a CO_2 laser. It has

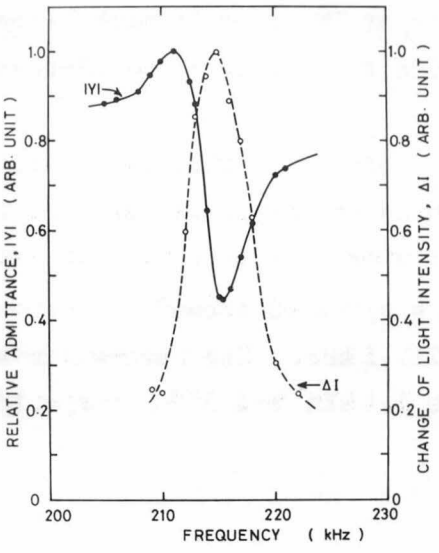

Fig.6.2-8 The electrical admittance of the modulator and the change in the amplitude of the detected light intensity as a function of driving frequency. The applied voltage is maintained constant at 22.5 V

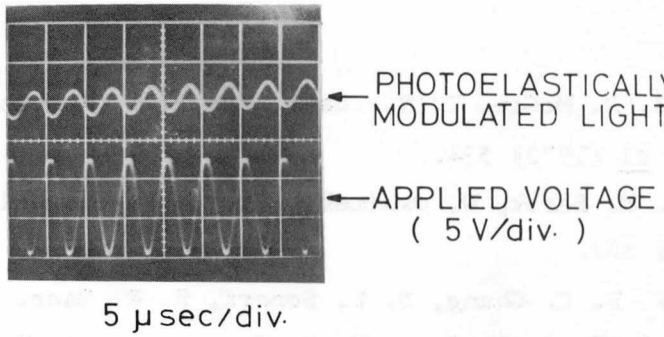

Fig.6.2-9 Wave forms of the applied voltage at 211.2 kHz and the modulated optical intensity.

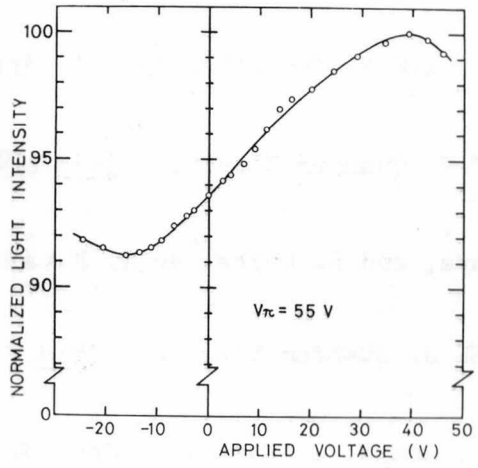

Fig.6.2-10 Detected light intensity as a function of the applied voltage. The frequency is maintained at the resonance of 211.2 kHz.

been also observed that the attenuation of TM modes is much larger than that of TE modes in accordance with the theory of metal-clad optical waveguides.

As an application, a photoelastic modulator utilizing a piezoelectric resonance of a Au-clad amorphous Se waveguide has been fabricated. PZT piezoelectric ceramics is used as a substrate to excite mechanical vibration. The modulator is operated around its fundamental length-expanding resonance of 211.2 kHz. The band-width and half-wave voltage are determined to be 5.4 kHz and 55 V, respectively [11].

References

[1] J. H. McFee, J. D. McGee, T. Y. Chang, and V. T. Nguyen, Appl. Phys. Letters 21 (1972) 534.

[2] P. K. Cheo, J. M. Berak, W. Oshinsky, and J. L. Swindal, Appl. Opt. 12 (1973) 500.

[3] M. S. Chang, W. S. C. Chang, B. L. Sopori, H. R. Vann, M. W. Muller, M. G. Graford, D. Finn, W. O. Groves, and A. H. Herzog, Appl. Opt. 14 (1975) 1572.

[4] P. K. Cheo and R. Wargner, IEEE J. Quantum Electron. QE-13 (1977) 159.

[5] S. Fukuda, T. Wada, T. Shiosaki, and A. Kawabata, Jpn. J. Appl. Phys. 16 (1977) 659.

[6] T. Takano and J. Hamasaki, IEEE J. Quantum Electron. QE-8 (1972) 206.

[7] Y. Suematsu, M. Hakuta, K. Furuya, and K. Chiba, Appl. Phys. Letters 21 (1972) 291.

[8] F. M. Garmire and H. Stoll, IEEE J. Quantum Electron. QE-8 (1972) 763.

[9] W. F. Koehler, F. K. Odencrantz, and W. C. White, J. Opt. Soc.

Am. 49 (1959) 109.

[10] W. C. Schneider and K. Vedam, J. Opt. Soc. Am. 60 (1970) 800.

[11] S. Fukuda, H. Kuroda, T. Shiosaki, and A. Kawabata, Trans. IECE Jpn. E-61 (1978) 160.

[12] A. Yariv, *Quantum Electronics* (Wiley, New York, 1975).

[13] Y. Ohmachi and J. Noda, Appl. Phys. Letters 27 (1975) 544.

CHAPTER 7

CONCLUSIONS

In this thesis, acousto-optic properties of single-crystal Te and amorphous Se at the 10.6-μm wavelength of a CO_2 laser are studied and discussed in detail from an applicational point of view. The results and conclusions obtained in this study are summarized as follows.

CHAPTER 2:

(1) Experimental results have been described for the acousto-optic properties of Te single crystal at 10.6 μm. It has been found that Te possesses exceptionally large acousto-optic frgures of merit M. The largest value, $M_{31} = 5850 \times 10^{-18}$ sec^3/g, has been obtained for longitudinal acoustic waves propagating along the crystallographic x axis and incident light polarized parallel to the z axis. The value of 4360×10^{-18} sec^3/g, obtained for M_{11}, is in fair agreement with the value determined by Dixon et al.

(2) Five of the eight non-vanishing independent Pockels photoelastic tensor components have been deduced from the above-measured figures of merit.

(3) The optical activity in Te has been precisely measured over the infrared wavelength range between 4.0 and 10.6 μm. Contrary to the previous results, the present measurements reveal that the magnitudes of levo- and dextrorotatory powers coincide with each other.

(4) The influences of optical activity on the acousto-optic properties of Te have been discussed.

(5) Based on the thus-obtained knowledges, the potential practical

applicabilities of Te crystal to an infrared acousto-optic deflector and modulator for the use especially at 10.6 μm have been evaluated in terms of figures of merit, optical properties, acoustic properties (especially acoustic loss), and resolution and access time. As a result, it has been found that Te single crystal is one of the most promising acousto-optic materials for 10.6-μm radiation.

(6) In order to avoid the harmful influence of an optical attenuation due to the absorption band centered at 11 μm, the use of an ordinarily polarized beam is preferred to the use of an extraordinarily polarized one as an incident light. Furthermore, for device applications in which only the driving power consideration is important, appropriate deflector configurations may be those utilizing longitudinal waves in the x direction and the corresponding large value of M_{12}. On the other hand, the deflector utilizing longitudinal waves in the z direction and M_{13} has an advantage for the applications which require operations with large resolution, large bandwidth, and short access time.

(7) A prototype of Te acousto-optic deflector has been fabricated based on these results and its operational characteristics have been examined at 10.6 μm.

CHAPTER 3:

(1) Contributions from the free-carrier screened indirect photoelastic effect and from the acousto-electrically induced free-carrier density waves to the photoelasticity in piezoelectric semiconductors have been considered by taking the existence of both electrons and holes into account. Explicit expressions for the effective photoelastic constants corresponding to these contributions have been derived on the basis of the small-signal acousto-electric theory. The results obtained are applicable either to extrinsic or to intrinsic semiconductors. It is derived that considerable cancellation takes place between photoelasticity due to the electron-density

wave and that due to the hole-density wave in intrinsic piezoelectric semiconductors. The numerical evaluation of these contributions to the photoelasticity has been carried out by taking Te as an example.

(2) In accordance with the theoretical prediction, an appreciable diffraction ascribable to the free-carrier density waves propagating in Te has been observed in the acousto-optic diffraction experiments using a 10.6-μm wavelength at room temperature. The observed diffraction intensity is in satisfactory agreement with the theoretically predicted one within a factor of 3. This is the first time that an acousto-optic diffraction due to free-carrier density fluctuations accompanying an acoustic wave has been observed in an intrinsic piezoelectric semiconductors.

(3) The experimental results have revealed that two of the nonvanishing independent Pockels photoelastic tensor components, p_{11}^{s} and p_{12}^{s}, have the same sign in Te.

CHAPTER 4:

This chapter describes an application of superior acousto-optic properties of Te to nonlinear optical effects and proposes a novel phase-matching technique utilizing acousto-optic interactions. Employing this phase-matching technique, relatively efficient optical second harmonic generation of a 10.6-μm light has been experimentally demonstrated. It has been revealed that by making use of this new phase-matching technique, restriction for the crystal orientation can be much relaxed as compared with the conventional collinear index-matching technique.

CHAPTER 5:

(1) It has been found that amorphous Se possesses large acousto-optic figures of merit almost comparable to those of Te. The obtained values are $M_{11} = 981 \times 10^{-18}\ \mathrm{sec}^3/\mathrm{g}$ and $M_{12} = 1080 \times 10^{-18}$

sec^3/g at 10.6 μm.

(2) The two non-vanishing independent Pockels photoelastic tensor components in amorphous Se have been determined as $p_{11} = 0.357$ and $p_{12} = 0.375$ at 10.6 μm. The wavelength dependence of these photoelastic constants suggests that the photoelasticity in amorphous Se can be attributed to the strain-induced change in the interband transition between the lone-pair p band and the antibonding p band.

(3) In spite of the large figures of merit, it has been found that pure amorphous Se is not very satisfactory as an acousto-optic medium since the glass transition temperature of about 30°C makes the material both mechanically and electrically very unstable at room temperature. It has however been found that the addition of several percents of arsenic (As) significantly shifts the glass transition temperature toward higher temperature region and consequently improves the acousto-optic properties as compared with pure Se.

CHAPTER 6:

(1) Optical waveguiding phenomena at 10.6 μm have been experimentally demonstrated for the first time in evaporated amorphous Se films with Au-cladding. The far-field analysis has shown that the fundamental TE_0 mode is most dominantly confined. The results have shown that amorphous Se can be used to form planar waveguides for the 10.6-μm radiation of a CO_2 laser. it has been also observed that the attenuation of TM modes is much larger than that of TE modes in accordance with the theory of metal-clad optical waveguides.

(2) As an application of remarkable photoelastic and acousto-optic properties of amorphous Se, a photoelastic modulator utilizing a piezoelectric resonance of a Au-clad amorphous Se waveguide has been fabricated. PZT piezoelectric ceramics is used as a substrate to excite mechanical vibration. The modulator is operated around its fundamental length-expanding resonance of 211.1 kHz. The band-width

and half-wave voltage have been determined as 5.4 kHz and 55 V, respectively.

APPENDIX

ACOUSTO-OPTIC DIFFRACTION THEORY

In this appendix, the theory of an acousto-optic interaction is briefly outlined [1,2].

The basic geometry of an acousto-optic interaction is defined in Fig.A-1. The x axis is chosen perpendicular to the boundary of the medium. An acoustic wave is propagating along the y axis. An optical beam is incident in the x-y plane with an angle θ_0 from the x axis. The beam width of the acoustic wave is L. The wave equation which describes the propagation of the optical wave in the medium can be written

$$\nabla^2 E = \frac{[n(y, t)]^2}{c^2} \frac{\partial^2 E}{\partial t^2} , \qquad \text{(A-1)}$$

where $n(y, t)$ is the refractive index in the region of the acoustic field ($0 < x < L$) and can be written

$$n(y, t) = n + \Delta n \sin(\Omega t - K y) \qquad \text{(A-2)}$$

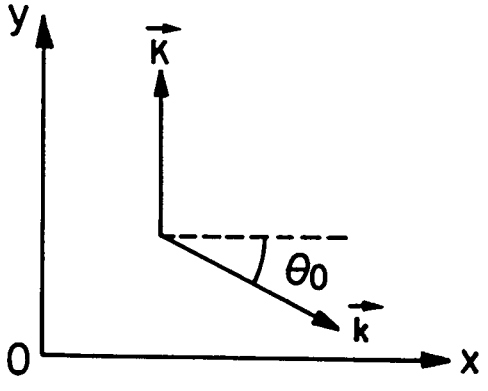

Fig.A-1 Interaction geometry.

for a sinusoidal acoustic field, where Ω and $\vec{K}$ are the angular frequency and wave vector of the acoustic wave, n is the refractive index of the medium in the absence of the acoustic field, and Δn is the amplitude of the index change. As the perturbed electrical field E is periodic in time and space with the acoustic field, it can be expanded in a Fourier series, yielding

$$E = \sum_{m=-\infty}^{\infty} E_m(x) \exp[\, j\{(\omega + m\Omega)t - \vec{k}_m \cdot \vec{r}\}] \,, \tag{A-3}$$

where

$$\vec{k}_m \cdot \vec{r} = n k (x \cos\theta_0 - y \sin\theta_0) + m K y \tag{A-4}$$

and ω and $\vec{k}$ are the angular frequency and wave vector of the incident optical wave in vacuum. $E_m(x)$ represents the amplitude of the m-th diffracted light with frequency of $\omega + m\Omega$. By substituting Eqs.(A-2) through (A-4) into Eq.(A-1) and neglecting second-order terms, we obtain a set of coupled, difference-differetial equations

$$\frac{dE_m}{dx} - \frac{\xi}{2L}(E_{m+1} - E_{m-1}) = j \frac{mQ}{2L\cos\theta_0} \left(m - \frac{\sin\theta_0}{\sin\theta_B} \right) E_m \,, \tag{A-5}$$

where

$$\xi = k \Delta n L / \cos\theta_0 \,, \tag{A-6}$$

$$Q = K^2 L / n k \,, \tag{A-7}$$

and

$$\sin\theta_B = K / 2 n k, \tag{A-8}$$

where θ_B is the Bragg angle measured in the medium. Q is the parameter introduced by Klein and Cook [1] as a useful criterion to determine in which regime the diffraction takes place: Raman-Nath ($Q \ll 1$), transition ($Q \sim 1$), or Bragg ($Q \gg 1$) diffraction. However, the practical limits of Raman-Nath and Bragg diffractions are customarily defined as $Q \lesssim 0.3$ for Raman-Nath region and $Q \gtrsim 4\pi$ for Bragg region.

Case (1): $Q \ll 1$ (Raman-Nath diffraction)

For an acoustic beam of low frequency and narrow width so as to satisfy the relation $Q \ll 1$, the diffraction takes the form of what is known as Raman-Nath diffraction, for which Eq.(A-5) reduces to

$$\frac{dE_m}{dx} - \frac{\xi}{2L}\left(E_{m+1} - E_{m-1} \right) = -j\, m K \tan\theta_0\, E_m . \qquad \text{(A-9)}$$

Using the identity equation for ordinary Bessel functions,

$$J_m(x) = \frac{x}{2m}\left[J_{m-1}(x) + J_{m+1}(x) \right], \qquad \text{(A-10)}$$

we obtain the solution

$$E_m(x) = \exp\left(-\frac{1}{2} j\, m K x \tan\theta_0 \right) J_m\left[-\xi \frac{\sin(K x \tan\theta_0/2)}{K L \tan\theta_0/2} \right]. \qquad \text{(A-11)}$$

The normalized intensity of the m-th diffracted light at L is then

$$I_m = |E_m(L)|^2 = J_m^2\left[-\xi \frac{\sin(K L \tan\theta_0/2)}{K L \tan\theta_0/2} \right]. \qquad \text{(A-12)}$$

Equation (A-12) reveals that many diffraction orders can be observed

in Raman-Nath diffraction. The diffraction pattern is symmetric at all angles of incidence since $I_m = I_{-m}$. The angle of diffraction of the m-th order is determined by

$$\sin\theta_m = \sin\theta_0 + m\frac{K}{nk} \quad . \tag{A-13}$$

Case (2): $Q \sim 1$ (transition region)

When $Q \sim 1$, it is no longer possible to obtain analytical solutions for Eq.(A-5). For a small value of Q, however, diffraction taking place in this region has a feature analogous to Raman-Nath diffraction. For a large value of Q, on the other hand, it resembles Bragg diffraction. The technique to obtain numerical solutions was proposed by Klein and Cook [1].

Case (3): $Q \gg 1$ (Bragg diffraction)

When the acoustic frequency is so high as to satisfy the relation $Q \gg 1$ and $\theta_0 \simeq \pm\theta_B$, only zeroth and first order beams are predominant. For θ_0 close to $+\theta_B$, Eq.(A-5) can be approximated as

$$\frac{dE_0}{dx} - \frac{\xi}{2L}E_1 = 0 \, , \tag{A-14}$$

$$\frac{dE_1}{dx} + \frac{\xi}{2L}E_0 = j\frac{2\zeta}{L}E_1 \tag{A-15}$$

with

$$\zeta = LK(\sin\theta_B - \sin\theta_0)/2\cos\theta_0 \, . \tag{A-16}$$

Phariseau obtained the solutions of these coupled wave equations as [3]

$$E_0(x) = E_0(0)\exp(j\zeta x/L)\left[\cos\left\{\frac{x}{L}\{\zeta^2 + (\xi/2)^2\}^{1/2}\right\}\right.$$

$$- j \frac{\zeta}{\{\zeta^2 + (\xi/2)^2\}^{1/2}} \sin\left[\frac{x}{L}\{\zeta^2 + (\xi/2)^2\}^{1/2}\right] . \qquad \text{(A-17)}$$

$$E_1(x) = - E_0(0) \frac{\xi/2}{\{\zeta^2 + (\xi/2)^2\}^{1/2}} \exp(j\,\zeta\, x/L)$$

$$\times \sin\left[\frac{x}{L}\{\zeta^2 + (\xi/2)^2\}^{1/2}\right], \qquad \text{(A-18)}$$

where the boundary condition, $E_1(0) = 0$, has been employed. The intensities of these waves at $x = L$ are obtained from the relations

$$\frac{I_0(L)}{I_0(0)} = \frac{|E_0(L)|^2}{|E_0(0)|^2} , \qquad \frac{I_1(L)}{I_0(0)} = \frac{|E_1(L)|^2}{|E_0(0)|^2} \qquad \text{(A-19)}$$

as

$$I_0(L) = I_0(0)[\,1 - (\xi/2\,\sigma)^2 \sin^2\sigma\,] , \qquad \text{(A-20)}$$

$$I_1(L) = I_0(0)(\xi/2\sigma)^2 \sin^2\sigma , \qquad \text{(A-21)}$$

where

$$\sigma^2 = \zeta^2 + (\xi/2)^2 \qquad \text{(A-22)}$$

and $I_0(0)$ is the intensity of the incident beam at $x = 0$. When the angle of incidence θ_0 satisfies the Bragg condition $\sin\theta_0 = \sin\theta_B$, we have $\zeta = 0$ and Eqs.(A-20) and (A-21) reduce to

$$I_0(L) = I_0(0) \cos^2(\xi/2) , \qquad \text{(A-23)}$$

$$I_1(L) = I_0(0) \sin^2(\xi/2) . \qquad \text{(A-24)}$$

Now, we shall derive a more explicit expression for ξ by making use of the inverse dielectric constant which is defined by

$$(1/\kappa)_{ij} = \varepsilon_0 \frac{\partial E_i}{\partial D_j} . \tag{A-25}$$

The changes in $(1/\kappa)$ due to strain are given by the photoelastic constant p_{ijkl} of the medium in the form

$$\Delta(1/\kappa)_{ij} = p_{ijkl} S_{kl} , \tag{A-26}$$

or in the contracted matrix notation,

$$\Delta(1/\kappa)_m = p_{mn} S_n . \tag{A-27}$$

The change in the dielectric constant is then obtained by making use of the identity equation

$$\Delta\kappa_{ij} = - \kappa_{ik} \Delta(1/\kappa)_{kl} \kappa_{lj} \tag{A-28}$$

as

$$\Delta\kappa_{ij} = - \kappa_{ik} p_{klmn} S_{mn} \kappa_{lj} . \tag{A-29}$$

Using the relation $n^2 = \kappa$, we have

$$\Delta n = - \frac{1}{2} n^3 p S , \tag{A-30}$$

where for simplicity the tensor notation is omitted.

It was shown by Nelson and Lax [4-6] that the formulation (A-26) is not sufficiently general to describe all acousto-optic phenomena. In particular, the photoelasticity arising from shear acoustic waves in anisotropic media is not fully covered by the conventional de-

scription (or equivalently, Pockels photoelasticity), which is expressed by Eq.(A-26). This is so because a shear wave not only causes a shear strain but also a rotation of the infinitesimal volume element [4]. In this appendix, however, we shall neglect this rotational contribution since it is discussed in detail in Chap.3.

The strain S is related to the acoustic power P_A as

$$P_A = \frac{1}{2} \rho v^3 \, S S^* \, L H \tag{A-31}$$

where ρ is the density, v is the acoustic velocity, and H is the height of the acoustic beam. The parameter ξ defined by Eq.(A-6) is then written

$$\xi = \frac{2\pi}{\lambda_0 \cos\theta_0} \left(\frac{n^6 p^2}{\rho v^3} \right)^{1/2} \left(\frac{P_A L}{2H} \right)^{1/2} . \tag{A-32}$$

Substituting Eq.(A-32) into Eqs.(A-23) and (A-24), we obtain

$$I_0(L) = I_0(0) \cos^2 \left[\frac{\pi}{\lambda_0 \cos\theta_0} \left(\frac{M P_A L}{2 H} \right)^{1/2} \right] , \tag{A-33}$$

$$I_1(L) = I_0(0) \sin^2 \left[\frac{\pi}{\lambda_0 \cos\theta_0} \left(\frac{M P_A L}{2 H} \right)^{1/2} \right] , \tag{A-34}$$

and the diffraction efficiency is given by

$$\eta = I_1(L)/I_0(0) , \tag{A-35}$$

where M is the figure of merit defined by

$$M = n^6 p^2 / \rho v^3 . \tag{A-36}$$

The diffraction treated above is what is known as isotropic (or normal) Bragg diffraction, which can be observed only when the op-

tical propagation constant $k = 2\pi n/\lambda_0$ concerning to the diffraction is of constant magnitude for all propagation directions. Since the Bragg condition stated by Eq.(A-8) is a consequence of the pseudo-momentum and energy conservation conditions

$$\vec{k}_0 = \vec{k}_1 + \vec{K} \tag{A-37}$$

and

$$\omega_0 = \omega_1 \pm \Omega$$

$$\simeq \omega_1 \qquad (\omega_1 \gg \Omega) \ , \tag{A-38}$$

the angle of diffraction in isotropic diffraction equals the angle of incidence, where $\vec{k}_0$ and $\vec{k}_1$ are the wave vectors of the zeroth and first order diffracted lights within the medium. The wave vector diagram describing isotropic diffraction is therefore an isosceles triangle as shown in Fig.A-2 (a).

On the other hand, anisotropic (or abnormal) Bragg diffraction takes place when the polarization plane of the diffracted light beam rotates at a right angle to that of the incident light (i.e., $i \neq j$ in Eq.(A-26)) and also refractive indices for both lights differ from each other [1,7,8]. In this case, the angle of incidence need

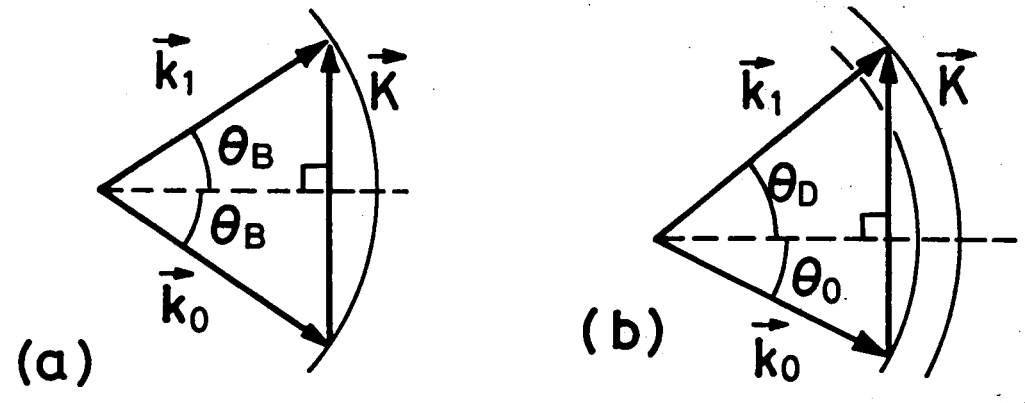

Fig.A-2 Wave vector diagrams for isotropic Bragg diffraction (a) and anisotropic Bragg diffraction (b).

not equal the angle of diffraction and a drastic asymmetry is observed in the wave vector diagram as shown in Fig.A-2 (b). The Bragg condition for anisotropic diffraction is given in Sec.3.2.B as Eqs. (3.2-42) and (3.2-43) [7]. The rigorous expression for the intensity of the first-order diffracted light is derived as Eq.(3.2-40) in Sec.3.2.B by properly taking all of the material anisotropy into account.

References

[1] W. R. Klein and B. D. Cook, IEEE Trans. Sonics Ultrason. SU-14 (1967) 123.

[2] N. Uchida and N. Niizeki, Proc. IEEE 61 (1973) 1073.

[3] P Phariseau, Proc. Indian Acad. Sci. 44A (1956) 165.

[4] D. F. Nelson and M. Lax, Phys. Rev. Letters 24 (1970) 379.

[5] D. F. Nelson and M. Lax, Phys. Rev. B 3 (1971) 2778.

[6] D. F. Nelson, *Electronic, Optic, and Acoustic Interactions in Dielectrics* (Wiley, New York, 1979).

[7] R. W. Dixon, J. Quantum Electron. QE-3 (1967) 85.

[8] O. Keller, Phys. Rev. B 13 (1976) 4612.

LIST OF PUBLICATIONS

A. Full Papers

(1) " Current Saturation Related to Internal Potential Barrier in Se Crystal", T. Shiosaki, S. Fukuda, and A. Kawabata, Jpn. J. Appl. Phys. 12 (1973) pp. 252-259.

(2) "Au-Clad Amorphous Se Optical Waveguides and a Photoelastic Modulator for the 10.6 μm Radiation", S. Fukuda, H. Kuroda, T. Shiosaki, and A. Kawabata, Trans. IECE Japan (Special Issue on Integrated Optics and Optical Fiber Communications), E61 (1978) pp. 160-163.

(3) "Acoustically Phase-Matched Noncollinear Optital Second Harmonic Generation in Tellurium", S. Fukuda, S. Ikeda, T. Shiosaki, and A. Kawabata, Jpn. J. Appl. Phys. 18 (1979) suppl. 18-1, pp. 121-126.

(4) "Acousto-Optic Properties of Tellurium at 10.6 μm", S. Fukuda, T. Shiosaki, and A. Kawabata, J. Appl.Phys. 50 (1979) pp. 3899 -3905.

(5) "Photoelasticity and Acousto-Optic Diffraction in Piezoelectric Semiconductors", S. Fukuda, T. Karasaki, and T. Shiosaki, and A. Kawabata, Phys. Rev. B 20 (1979) pp. 4109-4119.

B. Short Notes

(1) "Current Saturation Effect in Trigonal Selenium", T. Shiosaki, S. Fukuda, and A. Kawabata, Jpn. J. Appl. Phys. 10 (1971) pp. 1487-1488.

(2) "Electrooptic Effect in Thallium-Doped Selenium Crystal at 10.6 μm", S. Fukuda, T. Shiosaki, and A. Kawabata, Jpn. J. Appl. Phys. 12 91973) pp.1944-1945.

(3) "Infrared Optical Activity in Tellurium", S. Fukuda,

T. Shiosaki, and A. Kawabata, Phys. Status Solidi (b) 68 (1975) pp. K107-K110.

(4) "Acoustooptic Properties of Tellurium Single Crystal at 10.6 μm", S. Fukuda, T. Shiosaki, and A. Kawabata, Jpn. J. Appl. Phys. 15 (1976) pp. 927-928.

(5) "Acoustooptic Properties of Amorphous Selenium", S. Fukuda, T. Wada, T. Shiosaki, and A. Kawabata, Jpn. J. Appl. Phys. 16 (1977) pp.659-660.

C. Conferences and Symposium

(1) "Optical Waveguiding at 10.6 μm in Metal-Clad Amorphous Selenium Films", S. Fukuda, H. Kuroda, T. Shiosaki, and A. Kawabata, Digest of Tech. Papers, 1977 International Conference on Integrated Optics and Optical Fiber Communication, Tokyo 1977, pp. 125-128.

(2) "Acoustically Phase-Matched Noncollinear Optical Second Harmonic Generation in Tellurium", S. Fukuda, S. Ikeda, T. Shiosaki, and A. Kawabata, Digest of Tech. Papers, 10th Conference on Solid State Devices, Tokyo 1978, pp. 109-110.

(3) "Acousto-Optically Phase-Matched Noncollinear Optical Second Harmonic Generation in Tellurium", S. Fukuda, S. Ikeda, T. Shiosaki, and A. Kawabata, 1978 IEEE Ultrasonics Symposium Proceedings, Cherry Hill 1978, pp. 82-86.

(4) "Acoustooptic Interactions in Piezoelectric Semiconductor: Tellurium", To be published in 1979 IEEE Ultrasonics Symposium Proceedings, New Orleans 1979, (Invited Paper).

D. Other Papers

Besides the above-mentioned papers, 17 papers were orally presented at the meetings of Japan. Soc. Appl. Phys. and IECE Japan relating to the subjects described in this thesis.